ADVANCED OPTICAL SYSTEMS FOR IMAGING AND FABRICATION

Simonluca Piazza

PhD supervisors: Dr. Marti Duocastella

Prof. Alberto Diaspro

A thesis submitted for the degree of

Doctor of Philosophy

Ph.D. course in Bioengineering and Robotics

XXX Cycle

Department of Nanophysics, Istituto Italiano di Tecnologia, Genova, Italy

Dibris, Università degli studi di Genova, Genova, Italy

To my family

Contents

Introduction

The development of next-generation micro and nanotechnologies demands for tools capable of characterizing and modifying matter at ever decreasing scales. Among the vast arsenal of methods that offer local inspection and control of matter, optical systems are particularly appealing due to their inherent non-contact nature and possibility to selectively deliver energy at targeted positions. However, two main challenges still limit the use of optical techniques: their spatial resolution, which is intrinsically limited by the laws of diffraction, and their temporal resolution, which often compromise their capability to capture fast processes.

The use of light to characterize materials offers the unique possibility to collect information in a non-invasive and specific manner. This has prompted optical microscopy techniques to become the tool of choice to investigate samples in fields as important as materials science and biology. In the last decades, scanning microscopy techniques, such as confocal and multiphoton microscopy, have shown remarkable capabilities for the three-dimensional study of biological processes at the cellular and subcellular level. However, while scanning microscopes typically enable the investigation of samples with sufficiently high spatial resolution, they suffer from a limited imaging speed given by their intrinsic scanning nature. Therefore, the development of new microscopes enabling for faster acquisition of the fast dynamics of relevant biological phenomena represents one of the main challenges in modern optical microscopy.

The use of light to modify materials provides the possibility to accurately deliver a large amount of energy in any desired place, to achieve surface or bulk modification, and to interact with the desired material in a non-contact manner. To this end, laser-based systems have been successfully used to produce material modification according to a user-selectable design, leading

to applications such as welding, cutting, marking, or drilling, and becoming an indispensable tool for material processing in scientific and industrial applications. Despite the many advantages offered by laser-based techniques over standard methods, however, the use of light to modify a material still poses a strong constraint on the spatial resolution of optical systems. In fact, while diffraction limits the focusing capabilities of an optical system, light-matter interaction ultimately defines the achievable minimum feature size.

The goal of this thesis is to overcome inherent limitations of current optical systems in terms of their applicability for imaging as well as for microfabrication. In more detail, the overall structure of this work aims at two different technological objectives:

- Improve the temporal resolution of current optical microscopes while preserving the spatial resolution. In particular, by investigating how an optofluidic lens can be used to enhance the capabilities of standard laser scanning microscopes regarding three-dimensional (3D) imaging speed and penetration depth capabilities.
- Enhance the spatial resolution of current laser-based manufacturing techniques while maintaining their high processing speed. More in detail, by developing novel laser-based fabrication techniques to generate 2D and 3D features with a minimum size below the limits of diffraction.

This thesis is divided into three chapters. A brief description of each chapter is described next:

Chapter 1 begins with an overview of the fundamental principles of light-matter interaction and the basic concepts of optical systems. Particular attention is given to the introduction of the scalar theory of light which will be used throughout the thesis to describe the behavior of the implemented optical systems.

Chapter 2 contains a detailed description of a new optical microscope designed for high-speed three-dimensional imaging. A complete experimental and theoretical demonstration of the microscope working principle is provided, together with two case-study applications: enhanced 3D imaging in two-photon microscopy, and high-speed cross-sectional imaging for imaging flow cytometry.

Chapter 3 presents a novel strategy to overcome the intrinsic limits of laser fabrication techniques. The use of engineered materials whose shape can change according to an applied external stimulus in introduced to decouple the interaction of laser with materials into two steps: first, laser irradiation and initial material response, and second reconfiguration of the material according to the stimulus to achieve size reduction of the final structure.

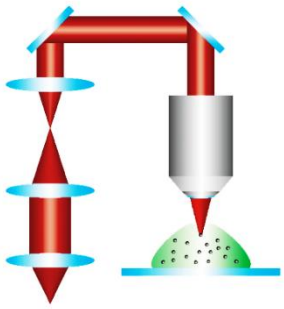

Chapter 1

Advanced optical systems for imaging and fabrication

Before diving into the design and development of optical systems capable of manipulating light to achieve particular goals or requirements, it is essential to gain familiarity with the fundamental processes underlying the propagation of light and its interaction with materials. Throughout this chapter, an introduction to the behavior of light and the theory of optics is presented. Special attention is given to the scalar theory of light (ray optics and wave optics), which will be used in the next chapters to describe the propagation of light in the developed optical systems. The fundamental principles governing light propagation and absorption in materials, as well as the resulting material responses, are then presented. Finally, a series of key concepts related to optical systems, such as image formation, resolution and depth of field are described.

1.1 Light propagation

Matter is what we are made of. Yet, it would be impossible for us to see and probe it unless we use light. It is indeed because of light that we can actually see and interact with the physical world surrounding us. The primary tool that allows us to use light to interact with the environment is represented by the human eye: the fundamental optical system in our everyday life. Despite being an invaluable tool, however, the naked human eye only offers limited temporal and spatial resolution of about 25 Hz and 100 μm respectively [1]. As a consequence, in order to extend our knowledge in a variety of fields, from the study of cells and stars to the study of light itself, the development of optical systems capable of enhancing our ability to collect, manipulate and shape light is of utmost relevance. It is thus important to understand how light propagates and interacts with materials. In the next sections, we introduce the basic concepts of light propagation and light-matter interaction. Our attention is focused on the scalar theory of light, which we can use in order to fully describe an optical system, and on the basic principles of optics and optical elements, useful to design new optical systems.

1.1.1 Ray optics, reflection and refraction

To a first approximation, the propagation of light can be modeled by considering it as a bunch of rays. As these rays travel through different media, they will be deviated from their original trajectory according to the laws of light-matter interaction. Light emitted from a lamp for instance, can be modeled as a collection of rays - in the form of simple straight lines - emanating from a source. Following Fermat's principle, light ray propagating from a point A to a point B in space will follow the path of stationary phase. However, a practical implication would be that light rays will usually travel

along the path that can be traversed in the least time [2]. Light traveling within an optically homogeneous medium will, therefore, propagate without deviations, while light passing through different media will be reflected and or refracted according to the optical properties of the encountered materials. As a result, we can model the behavior of light, to a first approximation, as a conjunction of ray optics and the mathematical rules of geometry. This simple yet powerful description of light falls under the definition of geometrical optics [3] and, notably, it is capable of predicting the behavior of light in many different scenarios. For example, rays emanating from a point can be traced as they travel through a lens and followed on the other side.

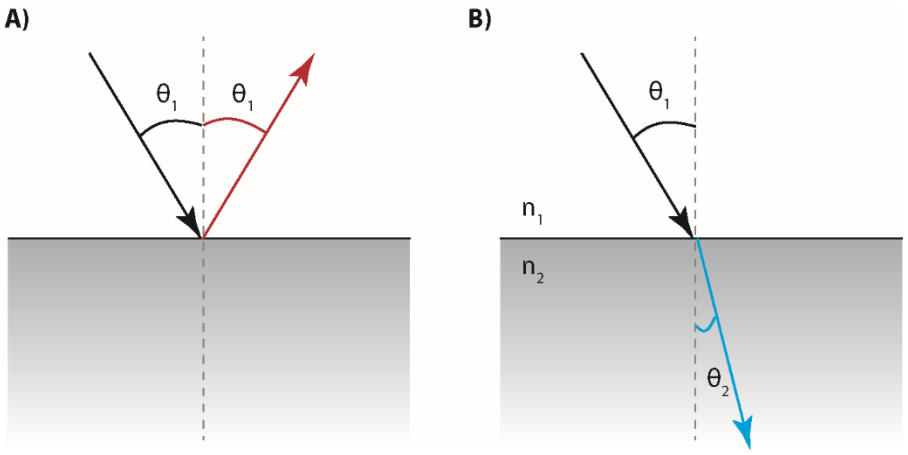

Figure 1.1 (A) Reflection and (B) refraction of light at the interface between two media of different refractive indices.

While ray tracing cannot explain fundamental phenomena such as diffraction and interference, it offers simplified modeling of light behavior mainly relying on the laws of reflection and refraction which are reported below.

Law of reflection: This law describes the behavior of a ray of light reflected by a surface, e.g. by a plane mirror. In such a case, the angle of reflection is

equal to the angle of incidence, both angles measured with respect to the normal to the surface and laying on the same plane (Figure 1.1).

Law of refraction: Known as Snell's law, the law of refraction governs the behavior of a light ray propagating across two media with different refractive index. Due to the different optical properties, the incident light ray is deviated from its original direction according to:

$$n_1 \sin\theta_1 = n_2 \sin\theta_2 \tag{1.1}$$

where θ_1 is the angle of incidence and θ_2 is the angle of refraction, both measured with respect to the normal to the interface, while n_1 and n_2 are the refractive index of the two media respectively (Figure 1.1).

Ray tracing can give reasonable explanations for different optical phenomena such as approximating image formation and image magnification of an optical system. However, since geometrical optics does not take into consideration the wave nature of light, it fails to explain relevant phenomena such as diffraction and interference. Notably, the study of diffraction and the limitations it imposes are essential to describe the behavior of optical systems [4].

1.1.2 Diffraction and wave optics

Diffraction refers to the behavior of light in the presence of an obstacle or a slit. More in detail, when the size of the encountered object (e.g. an obstacle or an aperture) becomes closer to the wavelength of light, the path followed by light cannot be explained anymore in terms of geometrical optics. As defined by Sommerfeld in 1954 [5], diffraction can be described as 'any deviation of light rays from rectilinear paths which cannot be interpreted as reflection or refraction'. A more intuitive definition of diffraction can be derived according to Huygens' Principle, which states that light traveling in

space can be represented as the superposition of spherical waves. More in detail, each point on the wavefront of propagating light can be considered to be a source of secondary spherical waves with the same frequency as the primary one. As an example, Figure 1.2 shows a schematic representation of Huygens' Principle applied to the case of a propagating plane wave – a wave whose wavefronts are infinite parallel planes. Notably, the wavefront and amplitude at a later instant can always be found as the summation of these secondary wavelets.

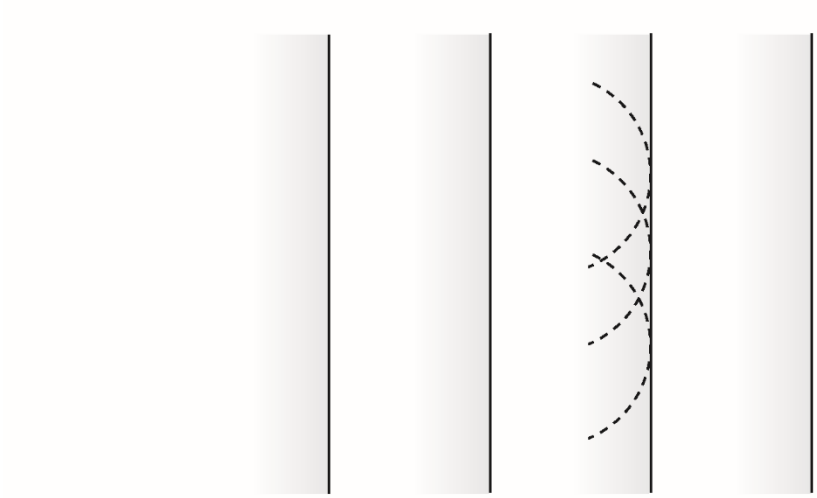

Figure 1.2 Huygens' principle for the propagation of a plane wave.

Following Huygens' idea, it was Young to further contribute to the theory of wave optics by describing the phenomenon of interference, that is: how different light waves can superimpose with each other in order to generate a wave with greater, lower, or equal amplitude [4]. Finally, Hyugens and Young descriptions of light were brought together by Fresnel, which was capable of calculating the distribution of light in diffraction patterns with excellent accuracy. According to Fresnel diffraction, light propagation in

space can be mathematically described as the convolution of the incoming wavefront with the paraxial approximation of a spherical wave [5]:

$$g_{out}(x', y', z) = \frac{e^{ikz}}{i\lambda z} \iint g_{in}(x, y)\, e^{\frac{ik}{2z}(x'-x)^2+(y'-x)^2}\, dxdy \tag{1.2}$$

where g_{in} and g_{out} are the input and output wavefronts, λ is the wavelength of light and $k = 2\pi/\lambda$.

Notably, while the wave nature of light found his origin in the experiments of Huygens and Young, the fundamental description of light as electromagnetic wave was not demonstrated until the introduction of Maxwell's electromagnetic theory. Firstly introduced at the end of the 19th century, Maxwell's equations describe how the electric and magnetic field originate by charges, currents, and changes of each other, and how these fluctuating fields propagate at the speed of light in the form of electromagnetic radiation [4]. Starting from Maxwell's equations, both the wave equation and the Rayleigh-Sommerfeld diffraction formula can be derived under the scalar approximation, which simplifies the mathematical treatment of electromagnetic fields by neglecting their vectorial nature [5]. While the wave equation formalizes the wave-behavior of light, Rayleigh-Sommerfeld formulation consolidates the theory of diffraction by providing a firmer mathematical foundation to the Huygens-Fresnel's principle.

1.2 Light absorption, scattering, and fluorescence

Although wave optics provides the fundamental tools to describe an optical system, it fails in describing the processes underlying the interaction of light with materials. To this end, the quantum nature of light and materials should be considered. Accordingly, each ray of light can be described not only as a propagating wave, but also as a collection of particles, named photons, each one bringing a fixed amount of energy. As a consequence

when light encounters a surface or passes through a medium, interactions occur between the light photons and the material atoms [6]. Following classical electromagnetism, these interactions can be represented to a first approximation with a simplified model [6]. When photons hit the atoms composing a material, they can exert a force on the electrons in a way that is inversely proportional to the wavelength of light. Once the free electrons are accelerated due to the energy absorption, they can in turn originate electromagnetic radiation in the form of emitted photons, or dissipate through non-radiative processes. This primitive representation of light-matter interaction can be used in order to describe the phenomena of absorption, re-emission, and scattering, which are at the basis of most common light-matter interaction processes [7]. Absorption occurs when photons successfully transfer energy to the electrons, causing them to jump to a higher energy state. The acquired energy is typically converted into other forms: it can, for instance, be dissipated into lattice vibrations (quasiparticles named phonons), or into other processes that result in heat dissipation (non-radiative process). Notably, given the resonant nature of absorption, a photon can be absorbed only if it has a particular energy. The absorbed energy can not only be dissipated through lattice vibrations or heat, but it can also be reemitted in the form of another photon. In such case, the emitted photon possesses lower energy with respect to the incident one (radiative process) and this phenomenon is denoted as fluorescence or phosphorescence. Finally, when light is not absorbed by electrons, the incident energy of a photon can be scattered across multiple directions while maintaining the same frequency. Since the frequency (energy) is preserved, this process is denoted as elastic scattering. Photons from scattered light possess a different phase (polarization) with respect to the incident one.

1.2.1 Light absorption and penetration depth

Material processing or characterization by means of light ultimately relies on the interaction of the used light source (e.g. a laser) with the desired sample (e.g. a biological tissue or a metallic substrate from a device). As an example, when performing imaging of thick biological tissues, light should ideally be able to penetrate the sample while being minimally absorbed. On the other side, when performing material processing such as laser-induced melting or ablation, the capability of light to penetrate into the sample represents a critical factor in order to determine whether surface or bulk processing can be obtained.

As previously introduced, when light encounters a material, part of it is reflected at the surface by cause of the discontinuity in refractive index, while the remaining part is transmitted inside the material. At the surface, reflectivity depends on different parameters including the polarization and angle of incidence of light, and the refractive index of the traversed media. The amount of light that is not reflected at the surface travels instead inside the material. More in detail, as light penetrates in the medium, its intensity decades with depth due to absorption. To a first approximation, the intensity of light I decades exponentially with depth according to the Beer-Lambert law [8]:

$$I(z) = I_0 e^{-\propto z} \tag{1.5}$$

where I_0 is the intensity of light at the surface, z is the penetration depth, and $\propto$ is the absorption coefficient of the material, which in turn is a function of wavelength and temperature. Notably, the reciprocal of the absorption coefficient, $1/\propto$ is defined as the absorption depth, and indicates the depth at which the intensity of the transmitted light drops to $1/e$ of its initial value.

It is worth mentioning that the description of light propagation in different media, as well as the specific absorption mechanisms, strongly depends on

the light and material properties [9]. As an example, when continuous wave (CW) or nanosecond pulsed lasers are used as light sources, most of the absorption can be attributed to single photon interactions. Instead, when picosecond or femtosecond lasers are used, the high instantaneous intensity carried by each laser pulse can give rise to nonlinear processes such as multiphoton absorption and optical breakdown. These latter phenomena not only are capable of decreasing the absorption depth, but are also responsible for changing the fundamental interactions of light with materials.

1.2.2 Light-enabled modification of materials

Light-matter interaction can be employed not only to properly shape and manipulate light as it travels through optical systems, but also to induce changes in the traversed materials which cannot be easily obtained with other methods. The absorption mechanisms through which light interacts with materials in order to induce permanent modifications can be broadly classified into three classes [8]: photothermal, photochemical, and photophysical processes.

As previously mentioned, when light from a laser impinges on a material, photons can couple to the available electronic or vibrational states depending on their energy. The time required by the excited electrons to transfer or dissipate the acquired energy strongly depends on the material properties. By comparing the light-induced excitation rate with the thermalization rate – time to reach thermal equilibrium – the three groups aforementioned can be distinguished. If the thermalization rate is higher than the light-induced excitation, the absorption process results mainly in heat generation. The material response is therefore determined by thermal effects and the process is defined as photothermal. Instead, when light-induced excitation prevails over thermalization, the absorbed energy can

directly lead to the breaking of the material bonds. During a photochemical process, the temperature of the medium usually remains constant. Finally, when both thermal and non-thermal mechanisms occur, the material response is defined as photophysical.

As in many cases photothermal processes play a key role in material modifications, it can be useful to understand the material response to thermal effects by modeling heat dissipation. To this end, the spatial and temporal propagation of heat inside a material can be represented using the heat equation [8]:

$$\rho(\bar{x},T)c_p(\bar{x},T)\frac{\partial T(\bar{x},t)}{\partial t} - \nabla[\kappa(\bar{x},T)\nabla T(\bar{x},t)] + \rho(\bar{x},T)c_p(\bar{x},T)\bar{v_s}\nabla T(\bar{x},t) = Q(\bar{x},t) \tag{1.6}$$

where ρ is the density, c_p is the specific heat capacity, κ is the thermal conductivity, v_s is the velocity of the substrate relative to the heat source, and Q is the volumetric heating rate, which also accounts for the contribution given by heat sources.

While the possibility to find an analytical solution to the heat equations is typically difficult, simplifying assumptions and approximations can often help explaining the material response as a function of heating, cooling rate, maximum temperature reached and temperature gradients. A relevant parameter which can be derived from the heat equation in order to understand the thermal response of a material is the thermal diffusion length:

$$l_T = \xi\sqrt{D\tau} \tag{1.7}$$

where ξ is a constant related to the geometry of the system and $D = {}^{\kappa}/_{\rho c_p}$ is the thermal diffusivity. Notably, thermal diffusion length is useful to determine the distance over which the temperature gradient inside the material propagates within a characteristic time τ (e.g. the time of laser irradiation).

Photothermal, photochemical and photophysical processes happening at the atomic and molecular level can lead to permanent material modification also at the macroscopic scale, causing permanent modification of the chemistry, composition, crystalline structure, or morphology of the material [10]. As an example, chemical reactions or phase transitions can be initiated when irradiating a material with fluences (energy per unit area) below the melting threshold. Material melting and deformation can instead occur due to high atomic mobility when the melting threshold is overcome. Finally, by properly selecting the laser source parameters, such as the wavelength, fluence, and pulse length, removal of material by direct absorption of laser energy, denoted as ablation, can be achieved. As for the previous cases, laser ablation can be obtained by overcoming the threshold fluence of the used material.

Laser ablation of materials can lead to evaporation and sublimation of the substrate (photothermal mechanisms), or to direct ionization and plasma formation which in turn cause phase transformations or direct bond-breaking (photochemical processes). While the first can be generally obtained with pulsed laser sources or, in certain cases, even with intense CW radiation, the latter are usually achieved by means of ultrafast pulses (e.g. femtosecond). A comprehensive description of these phenomena can be found elsewhere [8].

1.2.3 Scattering

Another optical phenomenon which must be taken into account when considering penetration of light into a sample is represented by scattering. As previously mentioned, scattering occurs when light, instead of being absorbed by electrons, is deviated (scattered) across multiple directions [11–13]. To this end, when light is focused into a material by means of an objective lens, scattering contributions can degrade the focusing capabilities

of the objective. When imaging is of interest, a turbid or thick sample can cause significant scattering of light, eventually resulting in a severe loss of signal-to-background. On the opposite side, when performing material modification, scattering should not represent an issue, as the dielectric materials used for laser processing typically present higher optical transparency compared to biological samples (e.g. glass, PDMS).

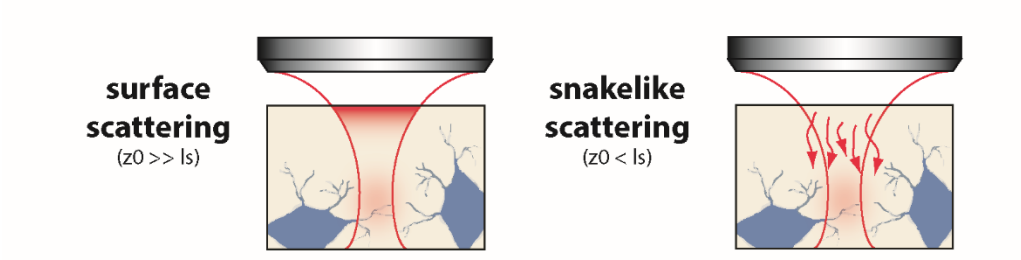

Figure 1.3 Schematic representation of surface scattering and snakelike scattering contributions.

To better understand how scattering can degrade the imaging quality of optical systems, we now briefly describe the two main types of scattering. The origin of such scattering can be broadly classified into two different regimes depending on the focus position z_0 within the sample and the scattering mean free path l_s – the distance between consecutive scattering events [14]. When $z_0 \gg l_s$, which usually occurs when the focus is deep inside the sample, high excitations powers are required to provide enough ballistic (non-scattered) photons to reach the focus – the number of ballistic photons decreases exponentially with depth (Figure 1.3). As a consequence, the intensity in the sample surface can be high enough to generate 2PE signal, especially when imaging specimens with a wide fluorescence labeling distribution. In this case, the out-of-focus background is originated by diffusive photons with randomized directions from the sample surface [15]. When $z_0 < l_s$, which typically occurs at short penetration depths or for weekly scattering samples, the out-of-focus signal is caused by snake-like

scattering – photons retain some memory of their initial trajectories [16] (Figure 1.3). Consequently, scattering effects originating from either diffuse or snake-like photons are somewhat present in all instances and can significantly degrade image quality and resolution by loss of signal-to-background (S/B).

1.2.4 Fluorescence

A good example of a photochemical process is represented by fluorescence, which happens when the absorbed light is reemitted in the form of another photon. In such case, the emitted photon possesses lower energy with respect to the incident one (radiative process) and this phenomenon is denoted as fluorescence or phosphorescence. As already mentioned in the previous sections, when light interacts with matter it can be absorbed by atoms or molecules which can be excited to higher electronic states. Such states are normally not stable, and after a certain time interval, known as lifetime, relaxation of the system to its ground state occurs. Radiative processes that originate from this relaxation are known as photoluminescence and include fluorescence and phosphorescence. The Jablonski diagram can help explaining absorption and photoluminescence processes. As reported in Figure 1.4, the diagram illustrates the electronic states of a molecule and electronic transitions as a function of the inter-nuclear distance.

The energy of the incoming light is absorbed by the molecule, which can be excited from a lower electronic state to a higher one. Usually, at ambient temperature (≈25°C corresponding to an energy of 25 meV) excitation mainly occurs from the electronic ground state S_0 that possesses the lowest vibrational energy, because higher vibrational states are not significantly populated at these temperatures. Typical energies required for this transition are on the order of few eV (1-3 eV) corresponding to wavelengths

in the UV-Vis-NIR range (wavelength = 250 – 1250 nm). Because light absorption is a fast process occurring on timescales of 10^{-15} seconds, no significant displacement of the heavy nuclei occur (Born-Oppenheimer approximation). Therefore, in the Jablonski diagram, photon absorption can be simply described by a vertical transition between states with the same nuclear coordinates (Franck-Condon principle). Thus, fluorescent molecules are excited to a higher electronic state and to the vibrational and rotational states corresponding to the nuclear coordinates.

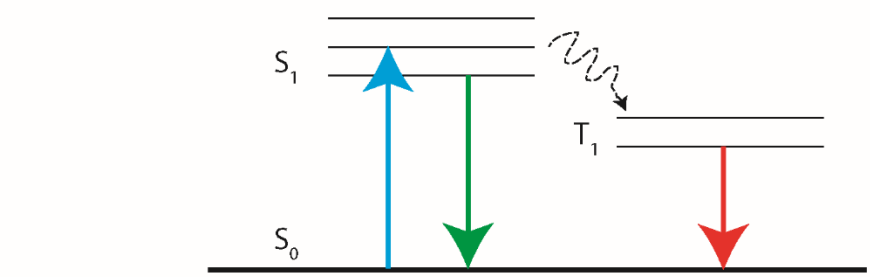

Figure 1.4 Jablonski diagram. After absorption of a photon, the molecule is excited to a higher electronic state. From there it typically reaches the ground state by vibrational relaxation. From S_1, the molecule can go to the ground state of S_0 via non-radiative decay channels or by the emission of a photon, called fluorescence. In addition, there can be intersystem crossing to a triplet state, which is energetically below the singlet state. The emission from T_1 to S_0 is denoted as phosphorescence.

Photon absorption is usually followed by vibrational relaxation, from one of the vibrational levels of the singlet excited state S_1 to the lowest level of S_1, a process known as internal conversion. Vibrational relaxation takes about 10^{-12} s. The molecule finally relaxes to S_0 after about 10^{-8} s, which is the typical fluorescence lifetime of commonly used fluorophores. Importantly, fluorescence is typically emitted from the vibrational ground state of S_1 to higher vibrational levels of S_0. As a result, the energy of the emitted photon is lower than that corresponding to the absorbed one. The shift to lower energy from the absorption to emission spectrum is called Stokes shift. The

Stokes shift of fluorescent molecules allows spectral separation of excitation and emission light and makes fluorescent-based methods an efficient tool for investigation of various photophysical processes. Fluorescence is of utmost relevance for bioimaging applications; however, there is a second phenomenon that can occur after photon absorption and electron excitation to the vibrational states of S_1. A spin-conversion-based decay channel can allow the relaxation of the excited molecule from S_1 to the triplet state T_1. This process is called intersystem crossing and can occur, with low probability, on time scales of 10^{-6} s or longer. In this case, the most likely transition occurs between states with overlapping nuclear coordinates which is usually an electronic state of higher vibrational energy. Importantly, photon emission as a result of the transition from T_1 to S_0 is known as phosphorescence.

1.2.5 Multiphoton absorption

In order to obtain fluorescence, the required energy of the exciting photons must be higher than the one of the emitted photons. In other words, the incident wavelength has to be shorter than the emitted one. Thus, in order to collect fluorescence in the visible spectrum, excitation has to be typically performed in the UV or visible range. There exists, though, the possibility of violating this condition. Indeed, if several photons are absorbed by a molecule within a very short time interval, a non-linear absorbing process can occur, named multiphoton absorption. In this case, the multiple photons that arrive simultaneously can add to each other, corresponding to a single photon whose energy is equal to the sum of the multiple photons.

By considering again the case of a fluorescent molecule, two-photon excitation can, in this case, be performed in the infrared spectral range. An example of a two-photon excitation process is schematically illustrated using the Jablonski diagram in Figure 1.5. The sum of the energies of two

infrared photons interacting with the molecule has to be greater than the energy gap between the molecule's ground and excited states. Since this process depends on the simultaneous absorption of the two photons, the probability of two-photon absorption by a fluorescent molecule is a quadratic function of the excitation radiance. From a practical point of view, in order to grant that the multiple photons arrive within a short time scale, ultrafast laser pulses are required. Additionally, to decrease imaging time, high repetition rates laser sources are desired, such as titanium sapphire oscillators. The higher peak power and the lower duty cycle of these lasers minimize average power deposition in the specimen while maximizing two-photon excitation efficiency.

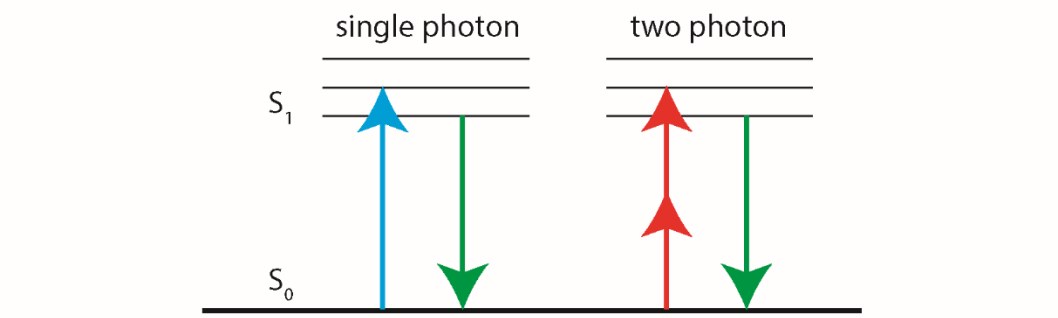

Figure 1.5 Jablonski diagram for one photon and two-photon excitation. Notably, fluorescent emission is the same for both modalities of excitation.

In general, multiphoton excitation scales with the n-power of the intensity, where n is the number of photons required for the non-linear excitation. The n-power function of the incident radiance allows to spatially localize the excitation process. Moreover, since scattering is inversely proportional to the incident wavelength, the use of red-shifted wavelengths required for two-photon excitation allows for the reduction of scattering-induced effects. This can render multiphoton absorption highly desirable for both imaging and material processing applications. As an example, thanks to the possibility to spatially localize the excitation and to the reduced scattering effect, two-

photon excitation microscopy offers a remarkable advantage in structural and functional imaging of high scattering biological samples [17,18]. On the other side, the spatial localization offered by multiphoton absorption represents an optimal solution when laser-induced ablation of transparent materials is of interest [19,20].

1.3 Basic concepts of optical systems

Optical systems can be considered as the enabling tools to either capture, manipulate or shape light. Their utilization ranges from microscopy to laser processing, with relevant applications in life sciences, imaging, industry, and defense [21]. While a standard definition of an optical system would be restrictive with respect to the many different possible implementations and applications, several key concepts can be used to determine and characterize its performance. Having introduced the basics of light theory and light-matter interaction; this section describes a series of relevant aspects of optical systems, such as the working principle of lenses, the concept of resolution and depth of field.

1.3.1 Focusing light through a lens

Among the different elements which can typically be found on an optical table, such as mirrors, prisms, filters and gratings, lenses represent the fundamental unit of optical systems. Starting from the small lens contained in our eyes, which serves to focus light onto the retina, lenses are indeed at the heart of optical devices like cameras, microscopes, telescopes, and eyeglasses.

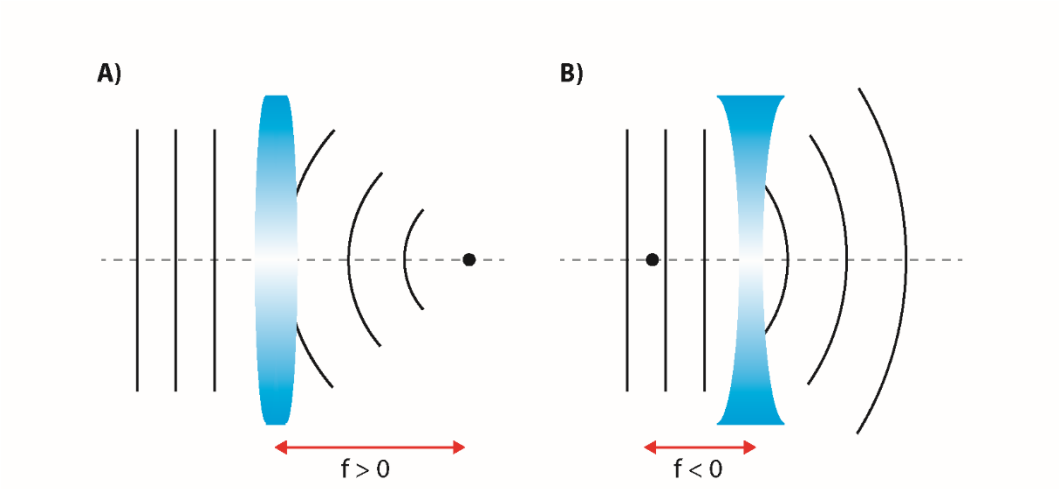

Figure 1.6 Effects of a (A) converging lens and a (B) diverging lens on a normally incident plane wave.

A simple lens typically consists of a transparent refracting material (e.g. glass), with spherically-shaped surfaces on the front and/or back, and is capable of focusing or dispersing light depending on its shape. When the thickness of the lens is negligible compared to the radii of curvature of the surfaces, the lens can be considered as a thin lens [5]. Following wave optics and paraxial approximation, the output wavefront of a thin lens can be obtained by multiplying the incident wavefront with the lens transfer function $t_l(\mathrm{x},\mathrm{y})$ according to [5]:

$$t_l(\mathrm{x},\mathrm{y}) = \exp\left[-\frac{jk}{2f}(x^2+y^2)\right] \tag{1.8}$$

where f represents the focal length of the lens, and is in turn related to the refractive index n of the material and to the radii of curvature R_1 and R_2 of the lens surfaces:

$$\frac{1}{f} = (n-1)\left(\frac{1}{R_1}-\frac{1}{R_2}\right) \tag{1.9}$$

Notably, the transfer function of the lens resembles the paraxial approximation of a spherical wave. As a consequence, a plane wave traveling through the lens, as shown in Figure 1.6, would be transformed by the lens into a converging ($f > 0$) or diverging ($f < 0$) spherical wave. While paraxial approximation helps to describe the behavior of light travelling through a lens, it is worth mentioning that under nonparaxial conditions, the emerging wavefront will contain aberrations in the form of deviations from a perfect spherical wavefront [4].

Up to this point, we characterized the focusing capabilities of a lens and introduced a description of the phase induced by a lens and of its focal length as a function of the lens shape. To better represent the behavior of light traveling through a lens, we can now investigate how light propagates after encountering the lens. To this end, we can combine the lens phase term from Equation 1.8 with the Fresnel kernel from Equation 1.2, expressed this time in case of a generalized pupil function $P(u,v,t)$ [5]:

$$U(x,y,z,t) = \frac{e^{ikz}}{i\lambda z}\iint_{-\infty}^{\infty} P(u,v,t)e^{\frac{ik}{2z}[(x-u)^2-(y-v)^2]}dudv \tag{1.10}$$

Where the pupil function $P(u,v,t)$ includes in this case the contribution of the input field U_0 incident on the lens with circular aperture $p(u,v)$ of radius R, and the phase term of the lens with focal length f:

$$\begin{aligned} P(u,v,t) &= p(u,v)U_0 e^{-ik\frac{u^2+v^2}{2f_0}} \\ p(u,v) &= \left\{ \begin{array}{ll} 1 & u^2+v^2 \le R^2 \\ 0 & u^2+v^2 > R^2 \end{array} \right\} \end{aligned} \tag{1.11}$$

As a result, the field propagation after the lens can be obtained by solving the Fresnel integral in the Fourier domain so to obtain the value of $U(x,y,z,t)$ at any given time. Notably, the generalized pupil function can be useful in order to approximate light propagation into an optical system [5]. In fact, by considering different optical elements (e.g. objective lenses) as thin lenses, all the phase terms introduced by these elements can be

included in the expression of the pupil function, thus being able to consider within a single expression all the main phase and amplitude contributions of an optical system.

1.3.2 Resolution

In the previous section, we described how a converging lens can be used to focus a plane wave to a point at a distance f along the lens optical axis. Notably, the smallest spot of light that can be focused by an ideal lens with circular aperture in such conditions is denoted as Airy disk, and its size is only limited by the laws of diffraction [2]. As depicted in Figure 1.3, the Airy disk is composed of a central bright spot surrounded by a series of rings. While the cross-sectional intensity variation of the Airy disk is independent from the used optics and wavelength of light, its width varies. As in the case of a single lens, the Airy disk can be obtained when imaging a single, point-like source in a dark background with an ideal optical system [22]. In this case, the resolution of the system is typically expressed as the full width at half maximum (FWHM) of the image of the point-like object, which is in turn defined as the point spread function (PSF) of the system.

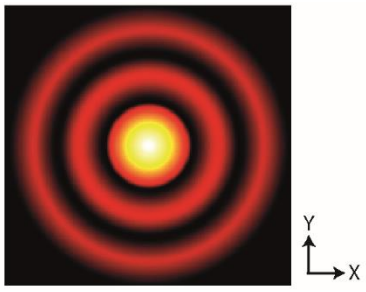

Figure 1.7 Image of the Airy disk obtained by simulating the propagation of laser light through a lens. The image depicts an image of the field collected at the focal plane of the lens.

The resolution of an optical system is classically described in terms of two-point resolution representing the distance at which the image of two points can still be distinguished from that of a single point. According to the Rayleigh criterion, two points are resolved if the distance between the maxima of their diffraction-limited images is at least as large as the distance from the peak to the first dark ring of the Airy disk, which yields to [23]:

$$r_0 = \frac{0.61\lambda}{NA} \tag{1.12}$$

where λ is the wavelength of light and NA is the numerical aperture. Notably, while this description accounts for the lateral resolution of an optical system, the very same approach can be used to determine the axial resolution. Accordingly, the resolution over the optical axis can be expressed as:

$$r_z = \frac{2\lambda n}{NA^2} \tag{1.13}$$

where n is the refractive index. Interestingly, the PSF of an optical system is usually measured by imaging sub-diffraction-size objects (e.g. fluorescent beads). As the size of these objects is smaller than the used wavelength, they can be effectively considered as point source emitters.

1.3.3 Depth of field

Depth of field can be considered as the distance between the nearest and farthest objects in space that appears acceptably sharp in an image. As it happens for instance in photography, images usually contain both in focus and out-of-focus information. While the first describes objects which appear sharp and well defined in the image, the latter refers to objects appearing blurred and poorly-defined. Discrimination of in-focus versus out-of-focus objects can be explained in terms of the focal plane of the objective, that is:

only the objects placed at the focal plane of the lens will appear in focus in the collected image. In case of a lens focusing light to a point, depth of field can be easily determined as the diffraction-limited axial resolution of the lens. While a variety of different criteria for determining when the image falls below an acceptable level of sharpness have been proposed, the Rayleigh criterion can often be used to compute the depth of field (DOF) of an optical system [22]:

$$DOF = \frac{2\lambda n}{NA^2} \tag{1.14}$$

where λ is the wavelength, n the refractive index and NA the numerical aperture. Notably, the DOF is mainly defined by the numerical aperture of the imaging lens and by the magnification of the system. Depending on the application (e.g. imaging or material processing) the DOF extension should ideally be either very narrow or very long. As an example, although a shallow DOF may improve the axial resolution, it can sometimes limit the capability of conventional microscopes to image three-dimensional samples [24]. On the contrary, the use of an extended-DOF (EDOF) scheme in an optical system can potentially enable to collect information from larger volumes at higher temporal resolution, therefore allowing for high-speed volumetric imaging [25]. The very same discrimination also happens in the case of material processing. While a short DOF can be a key parameter to induce material modifications with high axial resolution, an extended DOF could facilitate the fabrication of structures with a high aspect-ratio [26].

1.2.4 Optical sectioning

The capability to image biological specimens in three dimensions represents one of the major achievements of modern optical microscopy, and it relies on the possibility to eliminate out-of-focus light from the collected images [27]. When considering a laser scanning microscope [28], three-dimensional data

is usually collected by recording and then computationally rendering a stack of XY images taken at different focal planes throughout the specimen. Fundamental for this process is the concept of optical sectioning, namely the ability of the imaging system to remove unwanted light coming from above and below the imaged plane. Out-of-focus signal can completely obscure the in-focus information and greatly reduce the image contrast. Elimination of unwanted light provides greater contrast and allows correct three-dimensional (3D) reconstructions. Contrary to what happens in optical systems which are based on widefield illumination, confocal scanning microscopy, multiphoton scanning microscopy, and light sheet microscopy are the most widely used optical sectioning techniques for optical imaging applications [17,29,30].

1.3.5 Focusing light via non-traditional lenses

When considering the different types of lenses which can be found in an optical system, most of them will usually have a fixed focal length and a relatively narrow depth of field. As previously mentioned, these simple lenses are usually made of glass or plastic materials with a uniform index of refraction, and are shaped with a curved surface approximating a sphere or parabola which allows focusing or diverging light (Figure 1.8A). While these simple lenses constitute the fundamental unit of optical systems, they can impose constraints on the light-shaping capabilities of an optical system. As an example, given their relatively narrow depth of field, standard lenses cannot be used in order to collect information or, equivalently, to modify a material over extended depth of fields. At the same time, their fixed focal length limits their capabilities when a rapid shift of the focal position is required, as in the case of fast 3D imaging applications. In order to overcome these limitations, lenses enabling for non-traditional beam shaping capabilities can be adopted.

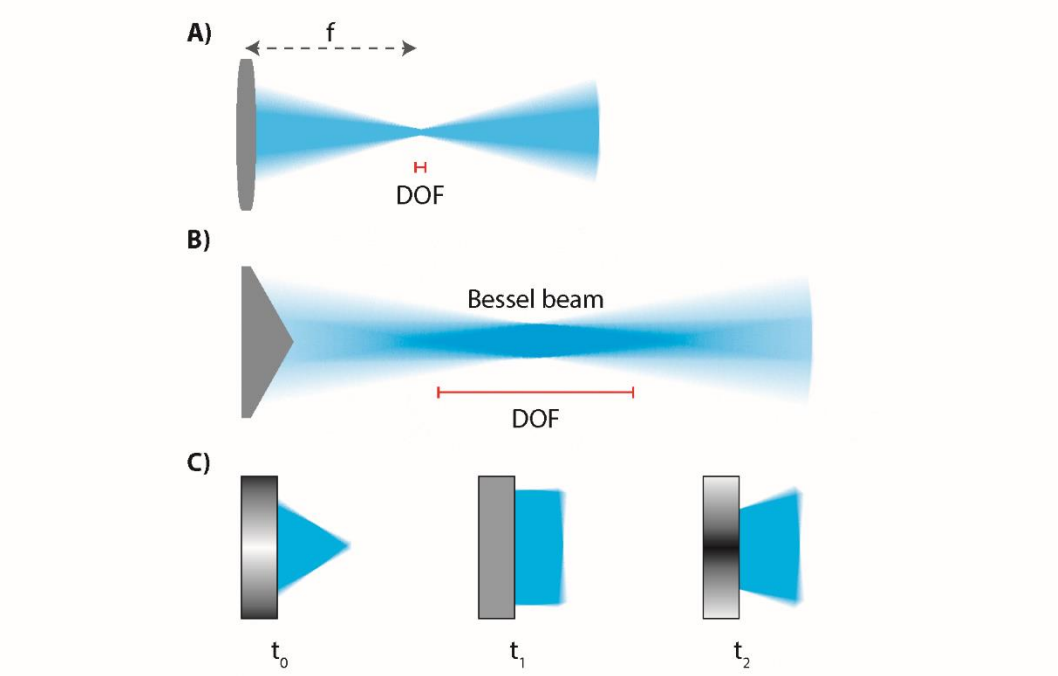

Figure 1.8 (A) A standard lens typically has a fixed focal length (f) and a relatively shallow depth of field (DOF). (B) An Axicon lens generates a non-diffracting Bessel beam which shows an extended depth of field compared to the standard lens in (A). (C) A tunable lens can vary its focusing capabilities over time. The image depicts three different time instants in which the lens focuses light (t_0), acts like a flat dielectric (t_1), and diverges light (t_2), respectively.

To achieve imaging, or materials processing over extended depth of fields, an optimal solution is represented by the use of Bessel beams, namely, 'non-diffracting' beams which shows a minimal spreading in the central lobe during wave propagation [31,32]. Interestingly, applications of Bessel beams include imaging, micromanipulation, nonlinear optics, and optical transfection [33]. While a detailed description of the properties of Bessel beams can be found in [34], one of the most convenient way to generate them is by using a conical lens element, or axicon lens [31], as depicted in Figure 1.8B. Nonetheless, even if the use of Bessel beams can help extending the depth of field of an optical system, axicon lenses are still fixed

optical elements. To this end, a useful alternative to standard lenses is represented by the use of tunable lenses that can be rapidly tuned over various focal distances just by using an external signal [35–37] (Figure 1.8C). The working principle of these lenses is usually based on a rapid change of either the lens surface curvature [38] or refractive index [36]. As these lenses typically require no moving parts, they provide the unique capabilities of focusing, defocusing, beam shaping, and extending depths of field by means of a single device and at high rates [39].

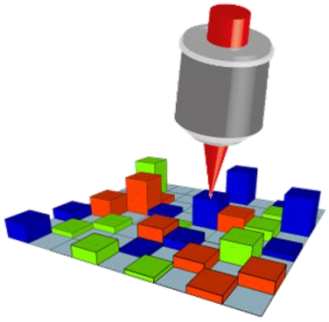

Chapter 2

Pixel-based Z-focus control in scanning microscopy

The invention of confocal laser-scanning microscopy (LSM) in 1957 by Marvin Minsky provided scientists with the capability of collecting clear images of biological samples in three-dimensions. Ever since, LSMs have become the tool of choice for unveiling the dynamics and structural organization of complex biological systems in a specific and non-invasive manner. However, as conventional LSMs are only optimized for collecting data from individual planes, the possibility to perform three-dimensional (3D) imaging of rapidly evolving biological systems is still constrained by a limited acquisition speed. In this chapter, the design and development of a novel optical system for rapid 3D imaging is presented. More in detail, a new optical microscope is introduced which relies on the integration of an acoustic optofluidic lens in order to achieve high-speed 3D imaging in both confocal and two-photon laser scanning microscopy. Our approach overcomes the traditional paradigm used for 3D imaging based on sequential acquisition of 2D planes by introducing a new degree of freedom in LSM: z-focus control on a pixel-by-pixel basis.

2.1 Introduction

Optical microscopes, arguably the most commonly used tools to characterize the building blocks of nature, are only optimized for acquiring two-dimensional information. In particular, they are designed to capture images from the plane perpendicular to the optical axis, namely the XY plane. This represents a strong limitation because the inherent 3D properties of samples require truly volumetric characterization tools. Indeed, the particular phenomena of interest may occur along the axial direction, but remain hidden by the difficulty in retrieving signal from outside the imaged XY plane.

When considering a standard laser scanning microscope (LSM) [29], a three-dimensional image is usually collected through the acquisition of a stack of 2D sections by sequential scanning in XY followed by axial focus translation. Fundamental for this process is the concept of optical sectioning, namely the ability of the imaging system to reject out-of-focus background [28]. Importantly, out-of-focus signal can completely degrade the in-focus information, and significantly reduce contrast of the acquired image. On the contrary, elimination of unwanted light provides greater contrast and allows correct three-dimensional (3D) reconstructions. While optical sectioning enables for 3D imaging at high-contrast, the need to acquire signal from a single axial plane at a time reduces the acquisition speed capabilities of LSMs.

Throughout this chapter, we propose a novel architecture for laser scanning microscopy (LSM) which provides an additional degree of freedom to these microscopes, enabling for fast acquisition of information along the Z-axis. The presented method relies on coupling an acoustic varifocal liquid lens into a LSM setup, in order to axially scan the focus at kHz rates [36]. Because the time to complete an axial scan can be in the microsecond time scale, multiple z-focus scans can be performed on a pixel by pixel basis. This opens up new possibilities for high-speed 3D imaging in LSM, allowing

for the collection of information from large volumes with an unprecedented spatiotemporal resolution.

2.2 3D imaging speed in state-of-the-art LSM

The three-dimensional imaging speed of a laser scanning microscope is related to its capability of rapidly collecting information from a desired volume. While most biological applications require subsecond time resolution, standard laser scanning microscopes usually provide slower imaging rates [40]. The main constraint in acquisition speed of a LSM is related to its point scanning nature. In order to obtain a three-dimensional image, sequential scanning in XY followed by axial focus translation is indeed usually performed. As a result, the inspected volume is imaged by acquiring a stack of 2D sections. Notably, techniques such as resonant scanners, temporal focusing, or 2PE light sheet microscopy [43,44,30] have proven successful in reducing the acquisition time for a 2D section (Table 2.1). However, the overall imaging speed is mainly constrained by the time required to mechanically move either the sample or focus along the Z direction. As an example, conventional piezoelectric actuators, which can be used for objective or stage motion, are usually limited by inertia to speeds below 100 Hz [45].

In order to improve the 3D imaging speed of LSMs, several approaches have been developed in addition to objective or stage motion [40]. These techniques mainly fall into two different groups: multiplexing or divergence control. Multiplexing approaches rely on the use multiple foci instead of a single one in order to parallelize the imaging process and reduce acquisition time. Multiplexing itself can be performed either temporally, spatially or as a combination of both and provides an enhancement in imaging speed directly proportional to the number of used foci [42]. As previously mentioned, successful implementations of these techniques include spatiotemporal

multiplexing and random access scanning microscopy [42,46–48]. Both these techniques operate by actuating a temporal split of the excitation signal into different regions of interest within the sample. Even though these approaches have shown great imaging capabilities in terms of volumetric speed (Table 1), their actual implementation often results in complex setups with limited degrees of freedom. Moreover, the need to determine a priori the focal spots, or planes of interest, might not be suitable in cases where the sample moves or changes over time. Sample motion can indeed shift the regions one desires to study with respect to the predefined illuminated positions, eventually resulting in image artifacts.

	3D technique	2D imaging time	Minimum pixel/ voxel time	3D imaging time
slow	Focal modulation	$\sim t_{pixel} \cdot n_{pixels}$	~ 0.2 ms	$\left(t_{2D} + t_{axial\ shift}\right) \cdot n_{planes}$
3D imaging speed	Standard	$\left(t_{pixel} + t_{scan}\right) \cdot n_{pixels}$	~ 10 µs	$\left(t_{2D} + t_{axial\ shift}\right) \cdot n_{planes}$
	Temporal focusing	$t_{exposure}$	~ 10 µs	$\left(t_{2D} + t_{axial\ shift}\right) \cdot n_{planes}$
	Random access scanning	$\sim t_{pixel} \cdot n_{pixels}$	~ 20 µs	$\sim t_{voxel} \cdot n_{points}$
	Ultrafast beam shaping	$\left(t_{pixel} + t_{scan}\right) \cdot n_{pixels}$	~ 20 µs	t_{2D}
fast	Temporal multiplexing	$\left(t_{pixel} + t_{scan}\right) \cdot n_{pixels}$	~ 10 µs	t_{2D}

Table 2.1 3D imaging microscopy techniques. Different microscopy techniques are listed and ordered with respect to their overall 3D imaging speed (left red bar), 2D imaging speed (t_{2D}), and minimum pixel/voxel dwell time. Imaging time is computed accordingly for each technique by considering the pixel/voxel dwell time (t_{pixel}, t_{voxel}), the time required to scan the beam between two consecutive points (t_{scan}), the exposure time in case of wide-fields systems ($t_{exposure}$), and the number of acquired pixels (n_{pixels}), points (n_{points}), voxels (n_{voxels}), and planes (n_{planes}).

Alternative techniques capable of high-speed volumetric imaging are based on the control of the divergence of the excitation beam prior to the entrance to the focusing objective lens. In this case, high-speed focus shifting can be achieved by changing the degree of beam divergence [35].

Because neither the sample nor the objectives are moved during imaging, problems related to mechanical vibrations can be avoided, offering an inherently fast 3D method. Divergence modulation of the beam is typically achieved by using devices such as deformable mirrors, spatial light modulators, or variable-focus lenses - most of which are tunable optofluidic lenses [49] [50]. Among the latter, axial focal shifting is usually achieved by a mechanical change of the lens shape. However, the need to physically change the lens curvature still imposes a fundamental limitation in terms of the speed such z-scanning systems can reach.

2.3 Pixel-based Z-focus control using an optofluidic lens

Recently, the use of an acoustic lens in confocal [51] and 2PE microscopy [25] has enabled continuous volumetric imaging at unprecedented speeds. This lens behaves as a resonant axial scanner [26], enabling phase modulation of the incident beam at microsecond timescales and leading to ultrafast beam shaping on a pixel-by-pixel basis. As such, an additional degree of freedom can be added to LSMs, enabling for fast acquisition of information along the Z-axis. Our implementation of a laser scanning microscope capable of performing high-speed 3D imaging relies on the use of an acoustic liquid lens for tunable phase modulation at microsecond timescales. Such a lens, called a tunable acoustic gradient index lens [36] or TAG lens, uses sound to induce periodic changes in the refractive index of a fluid. More in detail, the acoustic lens consists of a cylindrical piezoelectric tube filled with a transparent fluid (Figure 2.1). When a sinusoidal wave oscillating in the radiofrequency range is used to drive the piezo transducer, a pressure wave is generated inside the cavity which periodically alters the refractive index of the liquid according to [36]:

$$n(r,t) = n_0 + n_a J_0\left(\frac{\omega}{c_s} r\right) \sin(\omega t) \tag{2.1}$$

where n_0 is the static refractive index, n_a is the induced change in refractive index, J_0 is the Bessel function of the first kind, ω is the lens driving frequency, and c_s is the speed of sound. Note that typical resonant driving frequencies for the acoustic lens are in the order of hundreds of kHz, which implies phase modulation of the incident light at these rates. In addition, by changing the amplitude of the driving voltage, the value of n_a can be modified, and consequently the overall phase modulation induced by the lens.

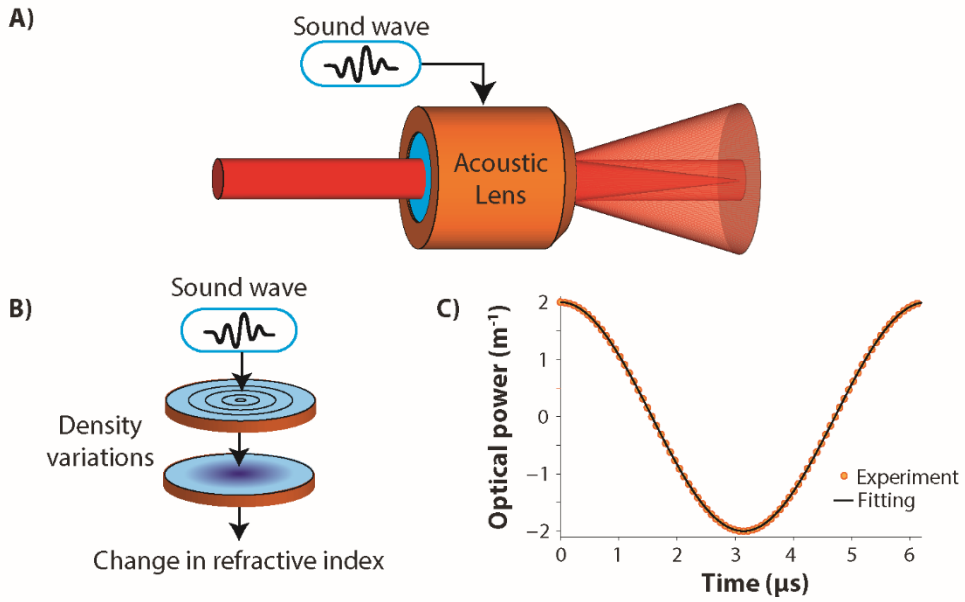

Figure 2.1 (A) Schematic representation of the acoustic lens. (B) The applied sound waves cause a density variation of the fluid contained within the lens, which in turn results in a change of the refractive index of the medium. (C) Temporal variation of the optical power ($1/f$) of the lens driven at 145 kHz.

The phase induced by the TAG lens can be used in two different beam shaping modalities. The fundamental difference between them lies solely on the relative size of the incident beam compared to the induced phase, as shown in Figure 2.2. More in detail, when $R < 2.4cs/\omega$ (2.4 is the zero of the Bessel function), the radius of the incident beam R only fills the central part

of the lens, and the phase profile from Equation 2.1 can be approximated to a parabola without introducing significant error. In this case, the lens optical power $\delta(t)$ can be written as:

$$\delta(t) = \frac{1}{f(t)} = \frac{Ln_a\omega^2}{2{c_s}^2}\sin(\omega t) \tag{2.2}$$

where $f(t)$ corresponds to the focal length of the lens and L is the length of the TAG lens. As a result, the acoustic lens acts as a high-quality varifocal parabolic lens whose focal length continuously oscillates between positive and negative values.

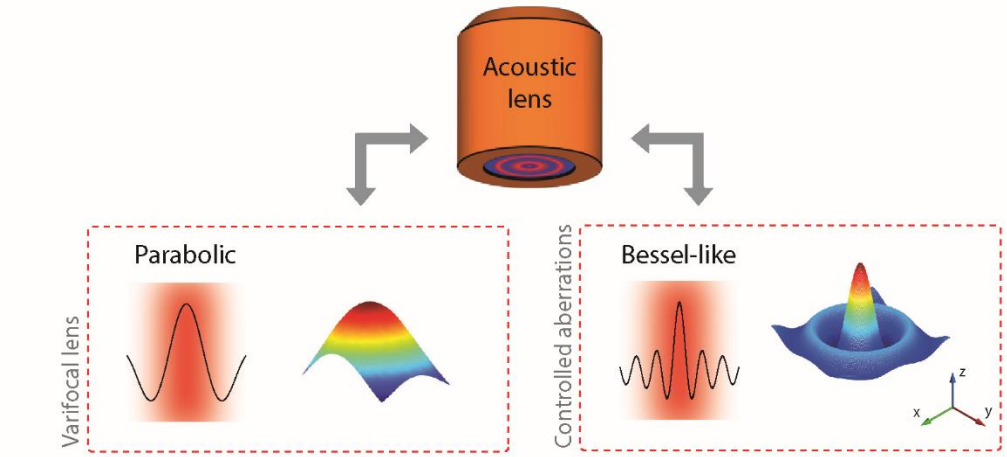

Figure 2.2 Beam shaping modalities. (Left) When a parabolic phase profile is used, the lens acts as a varifocal lens. (Right) When instead a Bessel-like phase profile is adopted, controlled aberrations can be induced in the excitation pathway. The different phase profiles depend on the lens driving frequency relative to the diameter of the incident beam.

At these conditions, by placing the acoustic lens in a conjugate plane with respect to the objective lens, and providing a sufficient pixel dwell time, ideally a multiple of the lens oscillating period [39], the lens induces a change in beam divergence at the objective pupil that results in one or

several axial scans at each pixel. Thus, within the pixel dwell time, information from different axial positions can be collected. Note that such 3D information can be captured at rates similar to a traditional 2D acquisition [38] (Table 2.1). By merging the information collected within each pixel, an extended depth of field (EDOF) image can be obtained. In addition, by sorting photons with respect to their arrival time, and given the a priori knowledge of the axial focus position, multiple planes can also be reconstructed. The axial separation between each plane can be arbitrarily selected, Nyquist criterion and signal-to-noise only to be considered [38].

The other beam shaping modality occurs when $R > 2.4cs/\omega$. In this case, the incident beam interacts with the Bessel-like phase profile described in Equation 2.1, resulting in the introduction of significant aberrations – mainly coma and spherical aberrations, with a small component of defocus. Thus, after passing through the objective the, phase of the beam will be continuously modulated at each pixel. Interestingly, for each modulation period there are two instances in which the collected signal is unaberrated. Indeed, when the sinusoidal component of Equation 2.1 equals zero, the lens acts as a flat dielectric and, consequently, no aberrations are observed. In this way, by applying proper demodulation, one can separate the aberration-free signal from the remaining aberrated information.

Notably, this can be then used to enhance the S/B of the collected images. In fact, by simply subtracting the aberrated information from the unaberrated signal [41], the out-of-focus background originated from scattering can be reduced producing an enhancement in the optical sectioning capabilities of the microscope (Figure 2.3). Finally, an important benefit of using the acoustic lens as a beam shaper is the possibility to move from axial focus shifting to induced control of aberrations by either changing the beam size or electronically modifying the driving frequency. In practice, the latter is easier to implement, with the only downside of the response time of the lens required to produce a stable modulation, in the order of ms [42].

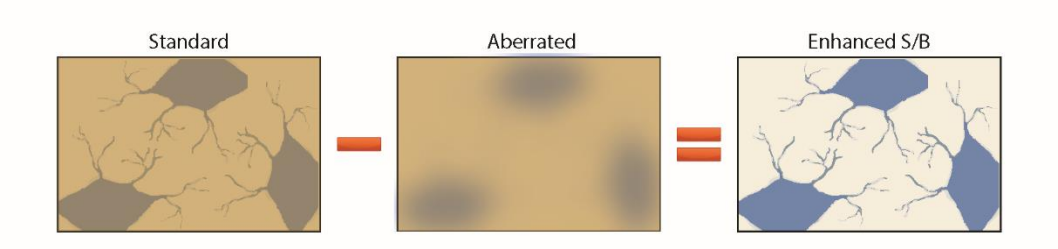

Figure 2.3 S/B enhancement algorithm. Out-of-focus background originated from scattering can be reduced producing an enhancement in the optical sectioning capabilities of the microscope by subtracting the aberrated information from the standard image.

A more rigorous formalism can help clarify the basic principles of the beam shaping described. To this end, we now simulate the effects induced by the acoustic lens when placed in the excitation path of a LSM. We investigate both high-speed axial scanning and controlled aberrations imaging modality, however, as the next sections of this chapter focus on the application of controlled aberration imaging for two-photon microscopy (2PE), we report simulations related to a 2PE system. More in detail, we simulate the wavefront propagation of the ballistic component in a 2PE system using the Fresnel diffraction integral [5,43]. As introduced in Chapter 1 section 1.2.2, the field amplitude at a certain Z position can be computed as the convolution between a generalized pupil function P(u,v,t) and a quadratic phase term (the Fresnel kernel) as given by:

$$U(x,y,z,t) = \frac{e^{ikz}}{i\lambda z}\iint_{-\infty}^{\infty} P(u,v,t)e^{\frac{ik}{2z}[(x-u)^2-(y-v)^2]}dudv \qquad (2.3)$$

where λ is the wavelength of light and $k = 2\pi/\lambda$. For simplicity, we consider the objective lens to be a thin optical lens with focal length f_0 and the acoustic lens to be placed at the back focal plane of the focusing objective (or in a conjugate plane with unit magnification). In this case, we can write $P(u,v,t)$ as the product of an input field U_0 limited by a circular aperture

$p(u,v)$ of radius R, and two phase contributes corresponding to the objective lens and the acoustic lens, which yields to:

$$P(u,v,t) = p(u,v)U_0 e^{-ik\frac{u^2+v^2}{2f_0}} e^{ik\theta(u,v,t)}$$
$$p(u,v) = \left\{ \begin{array}{ll} 1 & u^2+v^2 \leq R^2 \\ 0 & u^2+v^2 > R^2 \end{array} \right\} \quad (2.4)$$

where the radial and temporal dependency of θ is given by Equation 2.1. Once we solve the Fresnel integral in the Fourier domain and obtain the value of $U(x,y,z,t)$ for a given time, we can express the system point spread function (PSF) as $PSF = U^2$. Note that, due to scattering, the intensity of the ballistic photons (I_{2PE}) will decay with depth according to the Beer-Lambert's law. Therefore, we can write:

$$I_{2PE}(x,y,z,t) \propto (PSF(x,y,z,t)e^{-\mu_s z})^2 \quad (2.5)$$

where μ_s is the scattering coefficient and we have considered the non-linear excitation of 2PE. Finally, the overall intensity of the beam at different axial positions can be computed as [22]:

$$I_{2PE}(z,t) = \iint_{-\infty}^{-\infty} I_{2PE}(x,y,z,t)dxdy \quad (2.6)$$

Results of the simulations are presented in Figure 2.5. In all cases, we consider a wavelength of 800 nm, a Gaussian beam profile with a full width half maximum (FWHM) value of 4.2 mm, a speed of sound of 1000 m/s and a scattering coefficient of 7.5 mm^{-1} in agreement with that found in the literature for mouse brain [44]. The capability of the acoustic lens for volumetric imaging is shown in Fig. 2.5A. In this case, we simulate a lens driven at a frequency of 330 kHz, a pupil with a diameter of 2 mm, and so the incident beam is smaller than $2.4c_s/\omega$ ~ 1.2 mm, which corresponds to the conditions in which the acoustic lens acts as a varifocal lens. Note that these are the standard conditions of operation of the acoustic lens, as

demonstrated for confocal [38] and 2PE microscopy [20,45]. As expected, the beam is shifted axially for different time instances while preserving the peak intensity value and the FWHM, which is in agreement with the absence of aberrations – note that objective lenses are designed to operate at a specific focal plane, and thus there exists a practical limit of how much one can axially shift the beam focus without inducing aberrations [46].

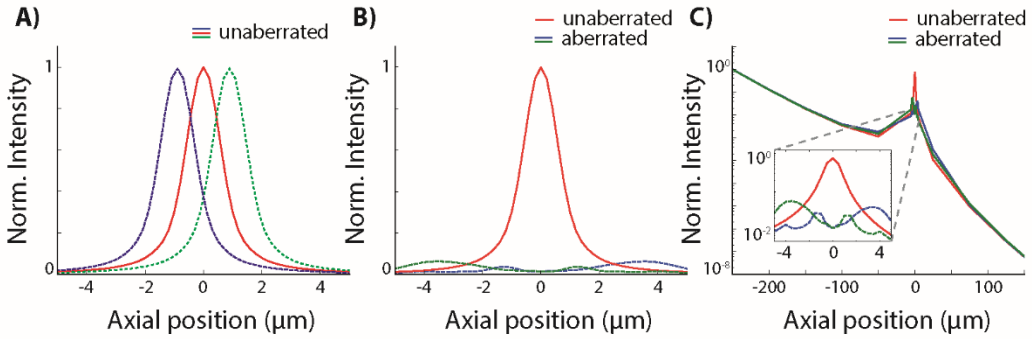

Figure 2.5 Acoustic lens beam shaping theoretical analysis. The plots represent the simulated axial PSF of a 2PE system when using (A) a parabolic phase profile and (B) a Bessel-like phase profile for three different time instances: red t=0 μs, blue t=0.75 μs, green t=2.25 μs. The natural focal plane of the system corresponds to the 0 μm position. (C) Axial PSF for the Bessel-like phase profile analyzed over a 450 μm range. The beam focus is set at 250 μm inside the sample.

A different situation arises when driving the lens at higher frequencies while preserving the rest of parameters constant (Fig. 2.5B). In particular, we simulate a frequency of 450 kHz, a pupil with a diameter of 15.6 mm (no pinhole is used), and hence 2.4cs /ω ~ 0.8 mm. Consequently, the incident beam interacts with a much larger fraction of the Bessel-like phase profile. In this case, the peak intensity of the beam quickly decreases while its FWHM increases as the beam is modulated (unaberrated beam at $t = 0$ μs). This corresponds to a decrease in the Stehrl ratio of our system from 1 to 0.1, which can be explained by the introduction of aberrations caused by the acoustic lens. Notably, the beam remains unaberrated (maximum

intensity, Stehrl ratio of 1) at 0 μm, as in this case the temporal phase profile of the lens corresponds to that of a flat dielectric. Additionally, the 2PE signal is quenched by the introduction of aberrations only in the vicinity of the focus, as shown in Fig. 2.5C. Thus, a simple subtraction between the unaberrated and aberrated signals is expected to reduce any contribute that results from out-of-focus signal, such as diffusive photons that originate in the sample surface, without significantly decreasing the signal from the unaberrated plane of interest. This provides the theoretical foundation for the subtraction approach used in the next sections for reducing out-of-focus background.

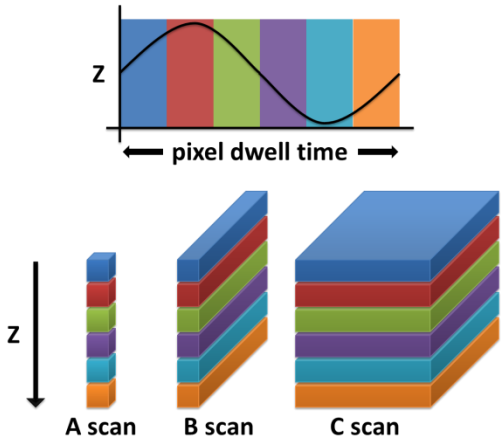

Figure 2.4 Pixel-based Z focus control and simultaneous capture of multiple focal planes in A, B, and C scans.

To conclude, our system operates in an analogous way to traditional resonant scanners, but instead of achieving high-speed X line scanning, it allows to obtain fast Z-line scanning. Moreover, by performing appropriate spatiotemporal demultiplexing of the collected photons, e.g. by using a fast acquisition card [38], reconstruction of each pixel along the z-scanned line can be obtained. As shown in Figure 2.4, this approach leads to a suitable architecture in order to perform A-scans, B-scans or C-scans, in analogy to

optical coherence tomography [47]; which in turn can be of interest for fluorescence correlation spectroscopy, imaging flow cytometry or fast volumetric imaging, respectively. In the following sections, we investigate and demonstrate pixel based z focus control can be used to enhance the three-dimensional imaging speed of confocal and two-photon microscopy. At first, we present the implementation of a two-photon microscope capable of performing high-speed 3D imaging (C-scan) of thick biological samples, together with enhanced penetration depth. Second, we show how the focus-scanning capabilities offered by the lens can be used to perform imaging flow cytometry (B-scan) in a commercial confocal microscope.

2.4 C-scan for enhanced volumetric imaging in two-photon microscopy

When considering the study of fundamental processes in life sciences, such as neuronal signaling or molecular diffusion at the cellular level, the development of optical techniques capable of performing non-invasive 3D imaging with high spatiotemporal resolution is of utmost relevance. To this end, two-photon excitation (2PE) microscopy [17,29,60] has been adopted as the de facto standard for imaging thick or scattering biological samples with sub-micrometer resolution, and at depths up to several hundreds of microns [61,18,62]. The multiphoton absorption process underlying two-photon excitation allows for intrinsic confinement of the focal volume to a diffraction limited spot. As a consequence, out-of-focus background is reduced, and optical sectioning is obtained with no need of pinholes or the use of structured light. Moreover, the longer wavelength photons – in the near-infrared spectral window – which are used to promote multiphoton absorption, typically present a lower scattering cross-section if compared to the ones used in single photon microscopy, therefore resulting in better penetration of light into tissues [29].

However, as the study of complex biological phenomena in fields as important as neuroscience demands for higher temporal resolutions over ever-increasing penetration depths [40], 2PE still faces two important challenges. First, the inertia of optical systems seriously limits three-dimensional (3D) imaging speed. Although resonant scanners can be used to reduce acquisition time for a single XY section, volumetric imaging rates are typically below 1 Hz due to the need to mechanically move sample or focus in the Z direction. Second, in thick tissues or turbid media, out-of-focus background generated by 2PE scattered photons can degrade image quality and resolution by loss of signal to background (S/B).

Here, we describe how the acoustic lens aforementioned can be coupled into a standard 2PE system in order to achieve high-speed volumetric imaging as well as enhanced S/B over high penetration depths. The lens is used to perform ultrafast beam shaping on a pixel-by-pixel basis, hence achieving phase modulation of the excitation light at microsecond timescales. By using high-speed readout, the detected photons can be sorted according to the corresponding phase induced by the lens. When a parabolic phase profile is adopted, high-speed axial focus shifting occurs, and continuous volumetric imaging is achieved. For other phase profiles, controlled aberrations can be induced just on the neighboring focal planes, and out-of-focus fluorescence can be removed with a subtractive algorithm. In this case, since all relevant information to background rejection is acquired in a single XY scan, potential problems related to motion artifacts are also suppressed. We provide a theoretical framework of our technique and demonstrate experimentally its capabilities by imaging 2 different scattering phantom samples and individual neurons from a mouse brain slice.

2.4.2 Optical system

The 2PE system consisted of a femtosecond laser source (Coherent Chameleon, 150 fs, 800 nm wavelength), an upright scanning microscope (Nikon FN1 C2+ confocal microscope) and an acoustic optofluidic lens (TAG Optics Inc. TAG lens 2.0). All experiments were performed using a 40x water immersion objective (Nikon CFI Apo Lambda S WI, NA 1.15).

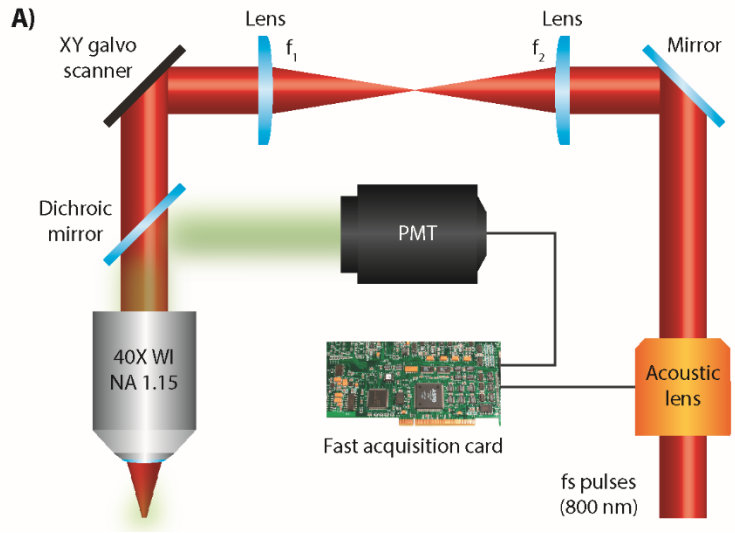

Figure 2.6 Scheme of the 2PE microscope used for ultrafast beam shaping on a pixel-by-pixel basis. The acoustic lens was placed in a conjugate plane of the XY galvo-mirrors. Demodulation was performed using a fast acquisition card.

We placed the acoustic lens in a conjugate plane of the XY galvo-mirrors located at the entrance of the microscope scan head, which were in turn conjugated to the back focal plane of the objective lens (Figure 2.6). For a telecentric system such as a 2PE microscope, this position for the acoustic lens minimizes potential magnification effects that the changes in the lens focal length could introduce [63]. The laser beam size at the entrance of the acoustic lens was 3 mm FWHM, and it was magnified by a factor of 2. Thus the beam filled the back aperture of the objective lens. We drove the acoustic

lens near the 330 and 450 kHz resonances for volumetric imaging and controlled aberration imaging, respectively. Because the effective aperture of the acoustic lens at 330 kHz is about 2 mm, we placed a pinhole of about this size in front of the lens. In contrast, no pinhole was used for the 450 kHz regime. To directly monitor the focal length of the acoustic lens at a given time, we measured the intensity of a continuous-wave (CW) laser source (657 nm) that passed through the lens slightly off its axis by means of a photodiode (Thorlabs PDA36A Si Switchable Gain Detector, 350-1100 nm). Because the CW laser is deflected with an angle that linearly depends on the focal length of the acoustic lens, the photodiode collects an intensity signal that results modulated accordingly. On the detection side, we used a photomultiplier tube (PMT) (Becker and Hickl HPM 100 40 hybrid detector) connected to a fast acquisition card (Becker and Hickl DPC-230, ~180ps time resolution) synchronized with the XY scanner of the microscope (pixel, line and frame feedback signals) and with the photodiode (Fig. 1A). We implemented custom-made software, written in Python language that allows the image processing of the acquired data, the temporal photon sorting and the execution of the subtraction algorithm.

Sample preparation: We characterized the optical response of our system by imaging a 3D sample consisting of fluorescent beads (Invitrogen FluoSpheres 170 nm yellow-green fluorescent beads) dispersed in 1% agarose (Invitrogen Ultrapure Low Melting Point Agarose). The quantification of the S/B enhancement of our approach was carried out by imaging two phantom samples that mimic scattering in tissues. The first sample consisted of 1.03 μm polystyrene beads (Polysciences, NIST microbeads) with a concentration of 0.0054 spheres/μm-3 dispersed into 1% agar solution together with 170 nm fluorescent beads with a concentration of 4 ppm v/v. In this case, the scattering coefficient obtained was 7.5 mm^{-1} according to Mie theory – close to the value typically found in brain tissue [64]. The second sample consisted of 4 μm fluorescent beads (Invitrogen Tetraspeck microspheres) under a 0.17 mm coverslip imaged

through an artificial turbid medium. In more details, the objective immersion medium was replaced by a solution with 10% v/v fluorescein dye and polystyrene beads in water with the same concentration as reported above, achieving a scattering coefficient of 7.5 mm-1. Because the scattering component of this sample is represented only by the immersion medium, a control experiment – with 'zero-level' scattering – could be easily performed by simply replacing the turbid medium with water. The performance of both volumetric imaging and S/B rejection were demonstrated by imaging neurons labeled with DAPI in a 500 μm thick mouse brain slice. In all cases, the excitation wavelength was set at 800 nm while fluorescence emission was collected in the 510-590 nm range.

Image analysis: Processing of the acquired data, including the temporal photon sorting and the execution of the subtraction algorithm, was performed using a custom-made software written in Python language. We evaluated the ability of our S/B enhancement algorithm to reject out-of-focus scattering by comparing the contrast of images acquired with and without the S/B enhancement. More in detail, we first quantified the S/B level of each image by collecting a line profile and by computing the ratio between the peak value from 'signal' pixels versus the mean value from 'background' pixels [66]. After obtaining the S/B ratio of the two images (with and without S/B enhancement), we quantified the relative enhancement introduced by our technique by computing the ratio between the two S/B values. We used a second metric to quantify our S/B enhancement by computing the contrast function C of each image according to [67]:

$$C = \frac{I_{max} - I_{min}}{I_{max} + I_{min}} \tag{2.7}$$

where I_{max} is the peak intensity of the image and I_{min} is the average background signal. Finally, we performed volume reconstruction of the acquired data in a two-step process. First, we reconstructed a stack of axial

planes from an extended depth of field image by dividing the collected photons into different time slots, each one corresponding to a different focal plane. Second, we used the stack to obtain a volume render using the volume viewer plugin from Fiji software [65].

2.4.3 Microscope characterization

Volumetric imaging: Initially, we assessed the capability of our microscope to simultaneously retrieve information from multiple z positions on a pixel by pixel basis. To this end, we characterized the lateral and axial system PSF using 170 nm fluorescent beads dispersed in agarose, as shown in Figure 2.7. We acquired two 3D stacks by translating the sample with a piezoelectric stage over an axial range of 50 μm with the acoustic lens off and on, respectively. For this particular experiment, the acoustic lens was driven at 330 kHz (an axial scan was completed in 1.51 μs) while the voltage was set at 23 Vpp and the pixel dwell time corresponded to 21 μs. At these conditions, the resulting phase profile can be considered parabolic ($R < 2.4cs/\omega \sim 1.2$ mm). As expected, when the acoustic lens was turned on (Figure 2.7A), the excitation beam was scanned multiple times over the z-axis at each pixel, and consequently, the integration of the pixel information resulted in an extension in the axial PSF from 1.5 μm to about 30 μm (FWHM values). Note that the achieved axial scanning range was in agreement with the theoretical value of 35 μm [35,68]. Importantly, the lateral PSF throughout the whole scanning range (average FWHM = 0.60μm) was comparable to the in-focus PSF with lens off (FWHM ≃ 0.55μm) (Figure 2.7C, D). This elongated PSF can be used to obtain an EDOF image [24].

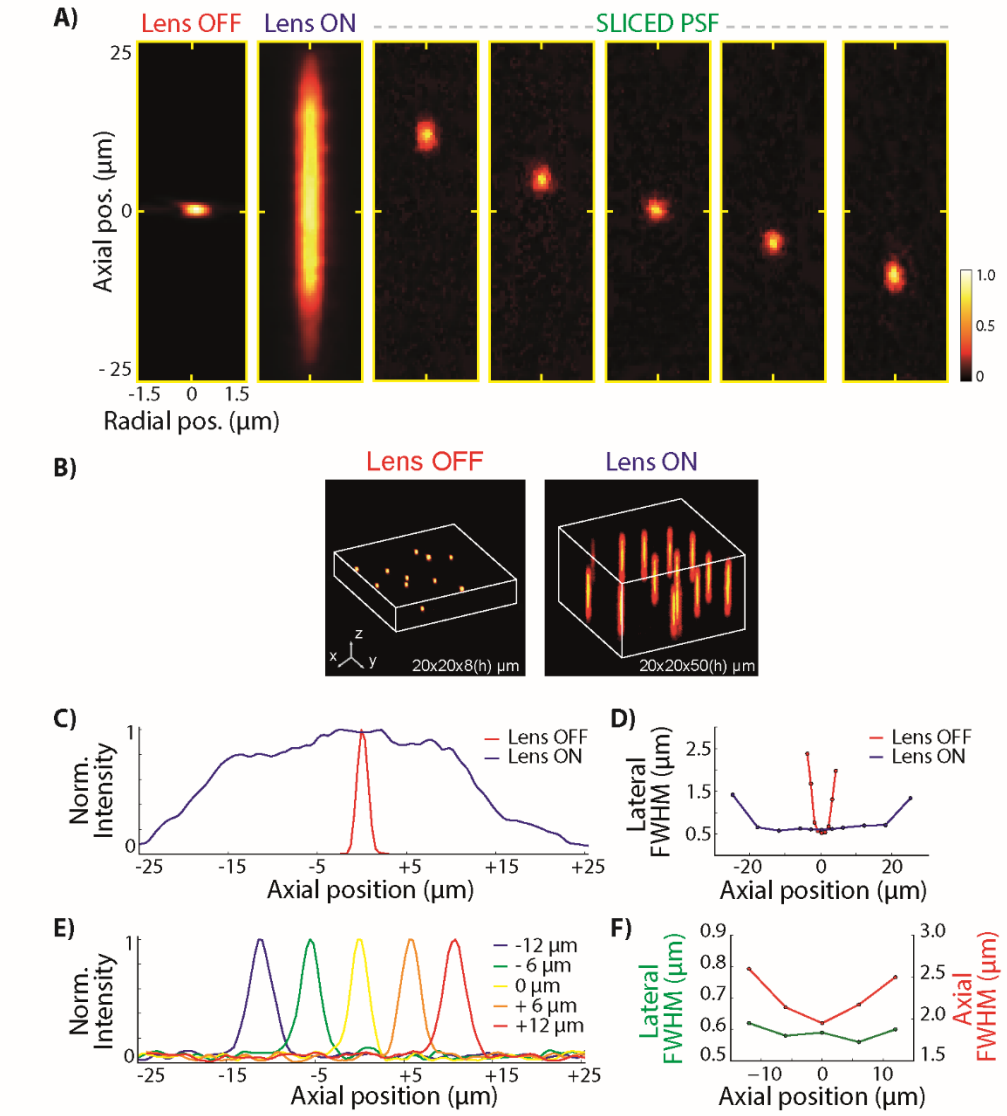

Figure 2.7 Experimental PSF characterization for 3D imaging. (A) Standard PSF of the 2PE system with the acoustic lens off and extended PSF obtained when driving the acoustic lens with a parabolic phase profile. Representative PSFs corresponding to 5 different reconstructed focal planes obtained starting from the EDOF PSF. (B) 3D reconstruction of the imaged bead with the lens off and on. (C) Intensity profile of the axial PSF with the acoustic lens off (red line) and on (blue line) and (C) corresponding plots of the FWHM of the lateral PSF vs axial position. (E) Axial PSF characterization of the 5 representative planes shown in (A). (E) Corresponding plots of the lateral and axial FWHM of the PSF vs axial position.

Figure 2.7B shows a 3D reconstruction of both datasets collected with the acoustic lens off and on respectively. Moreover, by properly demodulating the signal collected at each pixel, it is possible to convert the elongated PSF in multiple PSFs each corresponding to a different focal plane. To do so, we used the information captured with the fast acquisition card corresponding to the arrival time of each photon relative to the focal shift induced by the acoustic lens. Thus, we sorted the collected photons into different time intervals, with each time interval corresponding to a different focal plane. An image of the PSF reconstructed for five representative planes is presented in Fig. 2.7A. Note that, due to the continuous axial scanning of the acoustic lens, the number of planes can be arbitrarily chosen, with an upper limit imposed only by the signal-to-noise ratio. Importantly, the FWHM of the lateral PSF for each of these planes is 0.60±0.02 μm, less than 5% larger than the native resolution of the system with the lens off (Fig. 2.7F). The FWHM for the axial PSF is 1.9 μm for the plane located at z=0 μm (native focal plane of the system) and progressively increases up to 2.6 μm for planes located at z=±12 μm due to spherical aberration. Despite this slight decrease in axial resolution when using the acoustic lens, it is worth pointing out the speed at which the information from multiple axial planes can be acquired. At conditions reported herein (pixel dwell time of 21 μs, 256 pixels per line and an idle time between pixels of 0.5 μs), the time to obtain an XZ image (100 x 30 μm2) was only 5.5 ms, which implies up to 180 sections/second, a value that cannot be reached with traditional z-scanners.

Enhanced S/B imaging: The aberrations induced by our beam shaper when the incident beam interacts with the totality of the Bessel-like phase profile can be used to reduce out-of-focus scattering. As theoretically described above, a simple subtraction algorithm between unaberrated and aberrated signals should suffice. Importantly, a key aspect of our beam shaper is the capability to collect all the necessary information to generate the S/B enhancement at each pixel. In other words, the unaberrated signal

can be acquired together with the aberrated information. This requires appropriate demodulation of the phase induced by the acoustic lens, and hence the use of a fast acquisition card and initial calibration. To this end, we initially characterized the PSF of the system using fluorescent beads. In particular, we drove the acoustic lens at 450 kHz, while using an excitation beam size (3 mm) larger than 2.4cs /ω ~ 0.8 mm, thus satisfying the conditions for controlled aberrated imaging. Figure 2.8A shows the lateral FWHM and peak intensity of the PSFs reconstructed. Notably, there is a time instance in which the PSF intensity presents a maximum and its FWHM a minimum. This corresponds to the condition in which the acoustic lens behaves as a flat dielectric, and hence the PSF presents minimal aberrations.

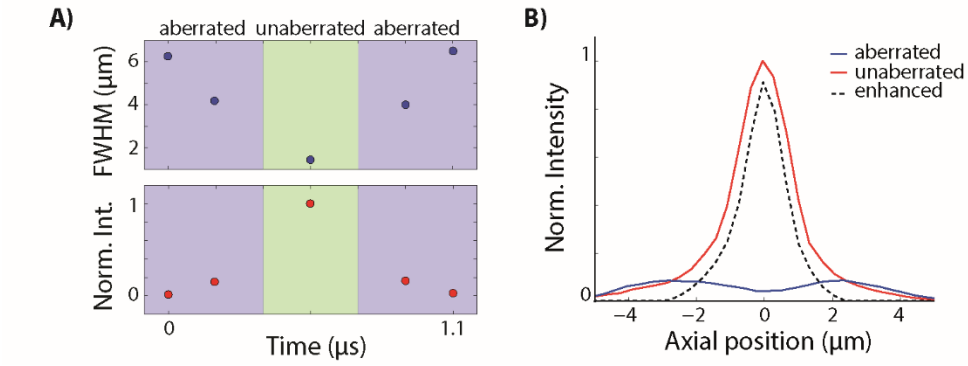

Figure 2.8 Experimental PSF characterization for aberrated imaging. (A) Temporal evolution of the lateral FWHM and normalized peak intensity of the PSF during half a period of oscillation of the acoustic lens. There is a time instance in which the FWHM presents a minimum and the intensity a maximum, corresponding to the moment in which the lens acts as a flat dielectric, and hence the signal is unaberrated (green region). In contrast, during the rest of the oscillation, the signal is aberrated (blue region). (B) The background rejection algorithm is based on a time-weighted subtraction of the time-weighted aberrated signal (blue line) from the unaberrated information (red line). The negative values are discarded after performing the subtraction (black dashed line).

Throughout the remaining text, we will refer to the information acquired during this time instance as the unaberrated signal. In this case, the value obtained for the FWHM is 1.9 μm, in agreement with the one obtained with acoustic lens off. In contrast, during the rest of the lens oscillation, the FWHM of the PSF is significantly wider, and the peak intensity decreases by almost a 90% with respect to its maximum. This behavior is consistent with a decrease in the Stehrl ratio of our microscope and the presence of aberrations, in good agreement with theoretical results when using the Bessel-like profile (Fig. 2.7B). Interestingly, because the acoustic lens spends more time collecting aberrated signal than unaberrated information, a time-weighted subtraction is required to properly adjust the contributions of these signals and remove the out-of-focus background. In particular, we calculated the enhanced signal s_{enh} as:

$$s_{enh} = \frac{s_{unab}}{\frac{t_0}{T}} - \frac{s_{ab}}{\frac{T - t_0}{T}} \tag{2.8}$$

where s_{unab} and s_{ab} are the unaberrated and aberrated fluorescence signal, respectively, t_0 is the time spent by the acoustic lens at the unaberrated position, and T is the oscillation period of the acoustic lens (for the experiments presented herein t_0 ~ 30% T). Finally, any negative value is discarded after subtraction. The experimental signals from Equation 2.8 are plotted in Fig. 2.7B.

2.4.4 Fast 3D imaging of neurons

We validated the volumetric imaging capabilities of our microscope by imaging neuronal cells from a 500 μm thick mouse brain slice. Figure 2.9A presents a standard XY image obtained with the acoustic lens off. Only a limited number of cells are visible. In contrast, when turning on the acoustic lens an EDOF is acquired, as shown in Fig. 2.9B. As expected, the number of visible cells is significantly increased, but the loss of optical sectioning

also results in a deterioration of image quality. Moreover, information regarding the axial location of the cells is lost.

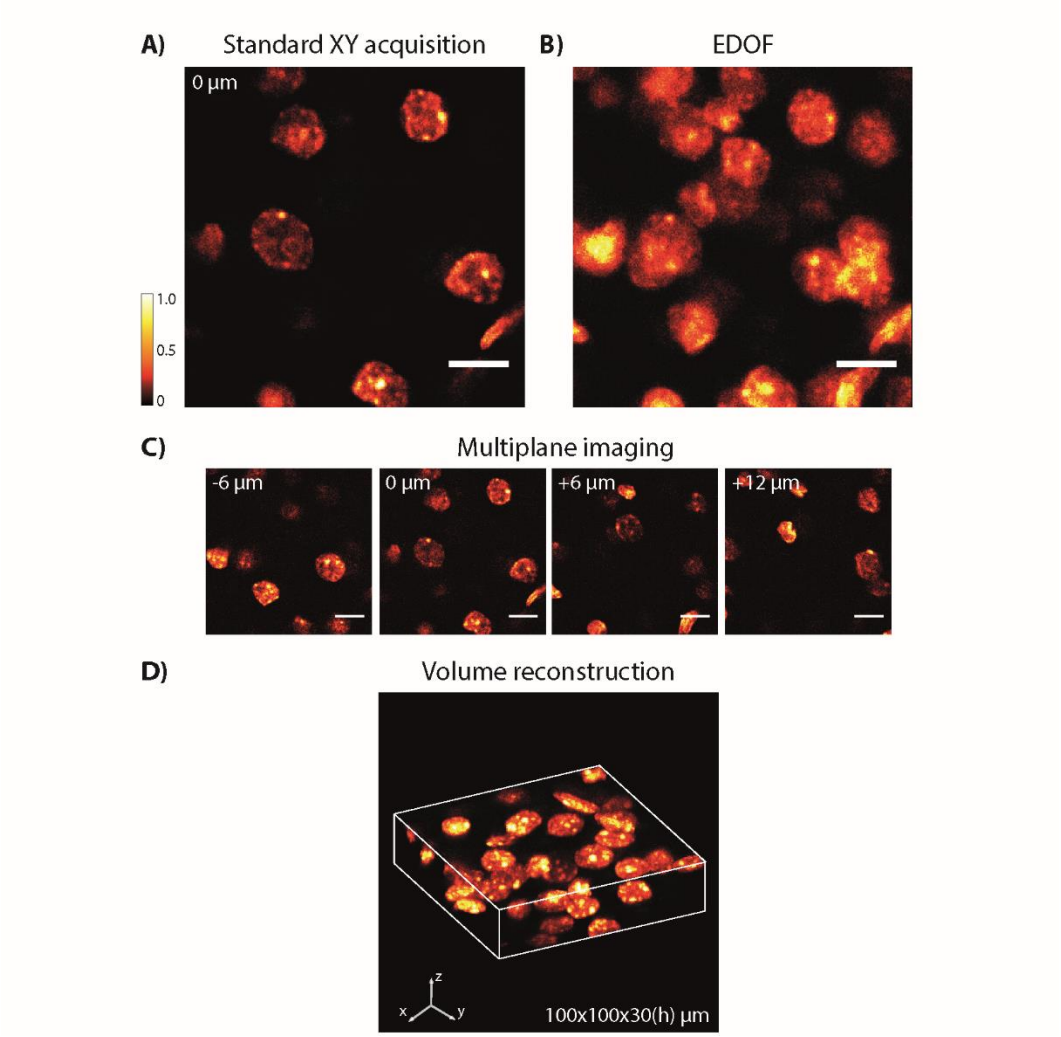

Figure 2.9 Volumetric imaging of neuronal cells from a 500 µm thick mouse brain slice. A) A standard XY 2PE acquisition. B) EDOF image obtained when driven the acoustic lens with a parabolic phase profile. C) Multiplane imaging with the acoustic lens. The 4 representative planes were captured in a single XY scan. D) Rendering of a 3D image from the reconstructed volume. Scale bars are 10 µm.

These problems can be solved by applying the multiplane imaging approach described above. Thus, by using the temporal information of the collected photons, images of multiple axial sections can be restored, as displayed in Fig. 2.9C. In addition, the reconstructed axial planes can be combined together to render a 3D image (Fig 2.9D). Importantly, all images in Fig. 2.9 were acquired at identical conditions (same acquisition time) except for the use of higher excitation power (about a factor of 5) in the case of the acoustic lens on. The need of high excitation powers is caused by the inherent axial multiplexing induced by z-scanning. Ideally, in order to capture the same amount of signal per plane as in traditional 2PE, one would need to increase the excitation power or exposure time by a factor equal to the ratio between z-scanned depth and nominal depth of focus. Still, because of the zero idle time during z-scanning with the acoustic lens, the amount of 3D information collected for a given time can be larger than in 2PE with mechanical stages. Additionally, the discontinuous illumination caused by the lens high-speed scanning can potentially help preventing photobleaching [69], even if higher laser powers are used. Indeed, the resonant scanning behavior of the acoustic lens favors the principle of triplet relaxation (T-Rex) microscopy [70], according to which photobleaching can be reduced by using pulsed excitation with an interpulse time separation long enough to enable the relaxation of the fluorescence molecule from the triplet state.

2.4.5 Signal-to-background enhancement in scattering phantom samples

To experimentally quantify the S/B enhancement of our approach, we used two different scattering phantom samples. First, we imaged fluorescent beads embedded in a 3D gel with a mean scattering length of 135 μm, as shown in Fig. 2.10. In more detail, we collected two 3D stacks of 30 μm each centered around two different depths of 50 μm and 250 μm, respectively.

Figure 2.10B shows the XZ maximum intensity projections for the standard (acoustic lens off) and enhanced S/B images, which were collected using the same acquisition parameters. When the imaging depth was relatively close to the surface (50 µm), the improvement in S/B is ~1.5, as shown in the intensity profiles. The image contrast C varies from 0.87 for the standard image to 0.90 for the enhanced S/B one.

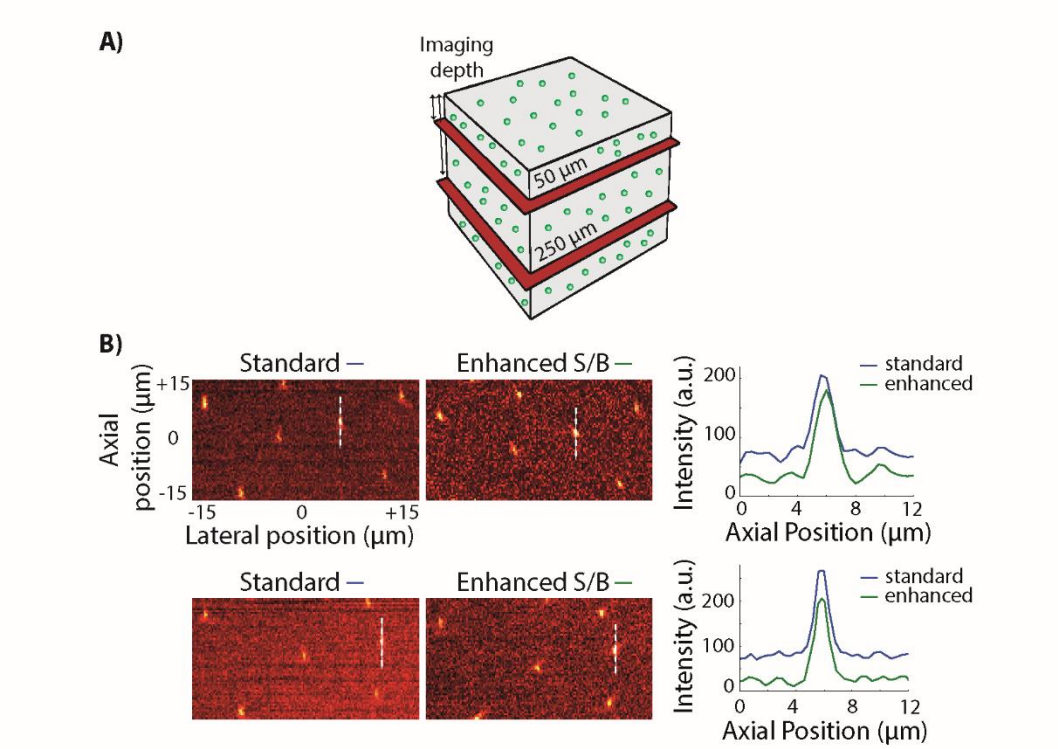

Figure 2.10 Quantification of the signal-to-background enhancement using the Bessel-like phase profile. (A) Schematic representation of the first phantom sample used as a model for tissue scattering, consisting of a mixture of 170 nm fluorescent and 1 µm non-fluorescent beads in agarose. (B) XZ sections obtained from 30 µm z-stacks using the standard (acoustic lens off) and S/B enhancement approach at an imaging depth of 50 µm (top) and 250 µm (bottom). The corresponding intensity profiles of the highlighted areas are shown on the right.

Instead, when imaging at a depth of 250 µm where the amount of scattering starts becoming significant, the enhancement in S/B significantly increases, up to a factor of ~3 while the image contrast is improved from 0.68 to 0.86.

The second phantom scattering sample we used to quantify the gain in S/B consisted of an immersion medium that was artificially rendered fluorescent and scattering, as shown in Fig. 2.11A. Because the scattering medium can be easily replaced by water, this system enables to evaluate the performance of our S/B approach against a control experiment in which no scattering is present. As shown in Figure 2.11B, 4 µm fluorescent beads observed through the scattering medium at a depth of 600 µm present a significant increase in background compared to the control experiment.

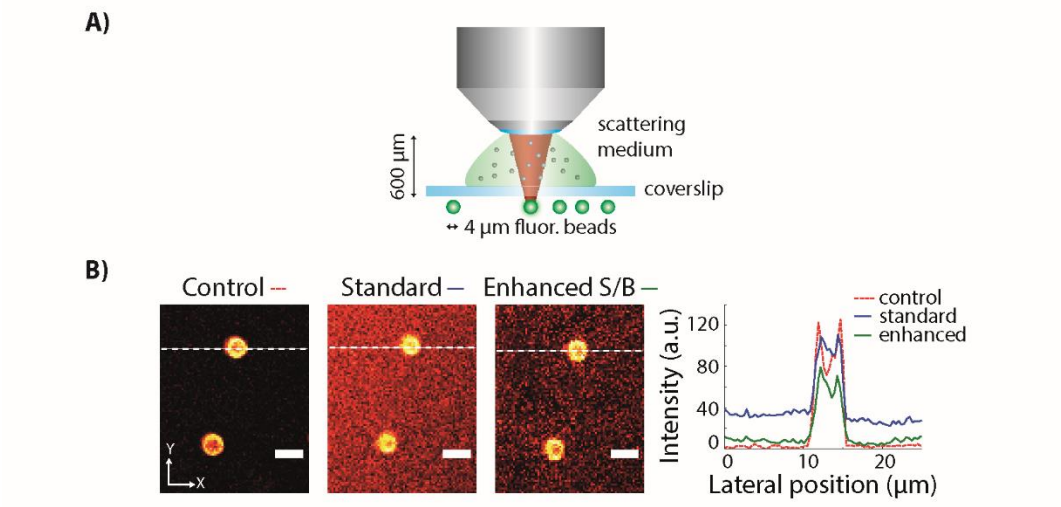

Figure 2.11 Quantification of the signal-to-background enhancement using the Bessel-like phase profile. (A) Scheme of the second phantom sample, in which 4 µm fluorescent beads were imaged through a scattering immersion medium. (B) XY images of the 4 µm beads using water as immersion medium (left), and the scattering medium in a standard acquisition (center) and after applying the S/B enhancement approach (right). The intensity profiles of the dashed lines are shown on the right. Scale bars are 5 µm.

Interestingly, by applying our S/B approach, the background is successfully reduced, and an image with improved contrast and sharpness can be restored. Because light traveled a long path through the scattering medium, in this case the enhancement in S/B is a factor of ~10 and the contrast C is enhanced from 0.69 to 0.93. Note that the S/B value is close to that obtained in the control experiment.

2.4.5 Signal-to-background enhancement in thick mouse brain slice

To better represent the S/B enhancement capabilities of our technique, we imaged a biological sample consisting of neuronal cells from a 500 μm mouse brain slice. In particular, we acquired a 20 μm thick z-stack at a depth of 250 μm inside the sample. Figure 2.12A depicts the maximum intensity projection for both XY and XZ planes for standard as well as for S/B enhanced images. Notably, both XY and XZ enhanced sections presents sharper details than the standard counterparts. Even if the subtractive approach results in a slight signal loss, the signal-to-background ratio of the enhanced images is improved – as it can be clearly observed in the intensity profile from Fig. 2.12B. In fact, a quantification of the S/B ratio reveals an improvement by a factor of ~3 for the XY images and by a factor of ~5 for the XZ images. Image contrast is enhanced from 0.87 to 0.92 for the XY images and from 0.63 to 0.78 for the XZ ones.

The results presented herein provide a novel technique to reject out-of-focus fluorescence in 2PE microscopy. A clear advantage of our S/B enhancement approach, besides the intrinsic simplicity and combination with volumetric imaging, is the capacity to capture all necessary information to suppress background at a pixel by pixel basis. Thus, potential drifts or motion of the sample or system that can affect the subtraction algorithm can be discarded. In contrast, a potential downside of our approach, common of

any subtraction method, is the impossibility to eliminate background generated from fast random events, such as the so-called shot noise. As a random signal is introduced in the acquisition process with a timescale shorter than the pixel dwell time, the subtraction step might not only eliminate it but can potentially increase it, eventually resulting in image artifacts.

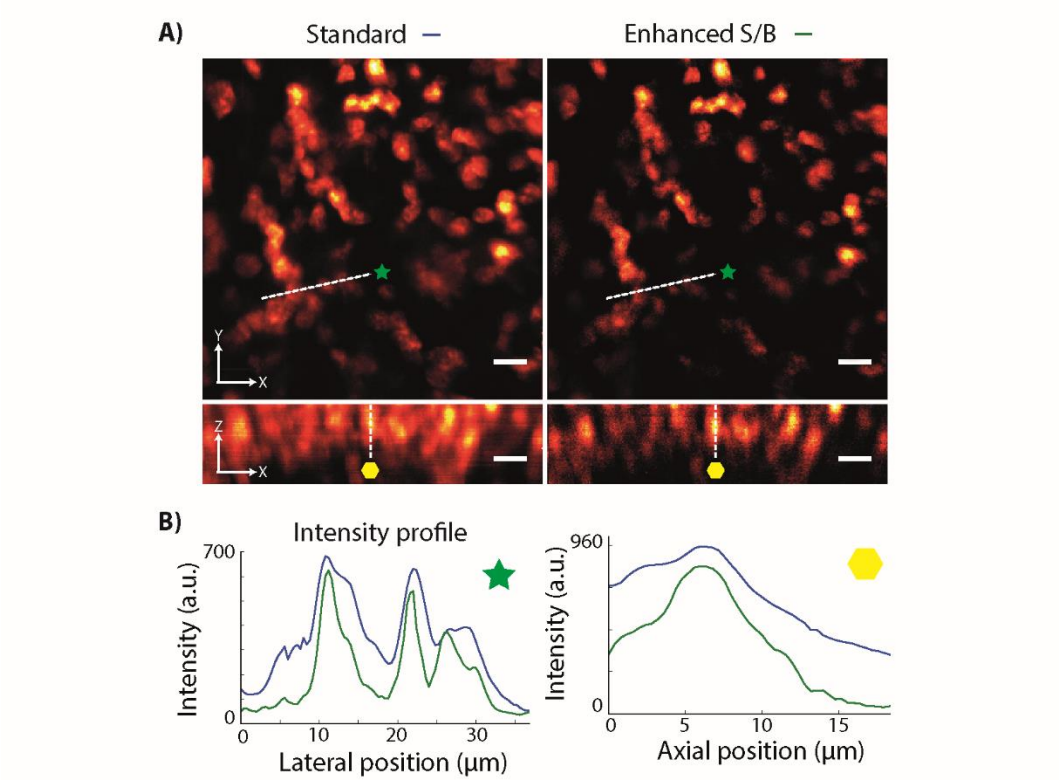

Figure 2.11 Signal-to-background enhancement in a biological sample. A) XY and XZ maximum intensity projection images of neuronal cell bodies from a mouse brain slice acquired at a depth of 250 µm in a standard configuration (acoustic lens off) and after applying the S/B enhancement approach. B) Plots of the intensity profiles corresponding to the dashed lines in the XY and XZ images. Scale bars are 10 µm.

In fact, a quantification of shot noise in our experiments obtained by measuring the standard deviation (SD) of the signal from the background regions of the images acquired reveals that our method does not remove shot noise. For instance, in Figure 2.10B at an imaging depth of 50 μm, the SD of background pixels (computed over an area of 50 by 50 pixels) is ±8 counts for the standard image and ±12 counts for the enhanced S/B one. Notably, the use of a longer integration time can help decreasing the effects of shot noise but does not reduce the contribution of out-of-focus background. Therefore, given that scattering typically represents the main source of background in 2PE at large depths, our approach should increase S/B for most of the biological applications.

2.5 B-scan for imaging flow cytometry in confocal microscopy

Flow cytometry is a well-established and powerful technique used to perform high throughput cell counting, cell sorting, and biomarker detection in fields as important as cellular biology, biotechnology, and medicine [71] [72]. By suspending cells in a laminar flow and passing them through a laser-based detection system, a flow cytometer typically allows simultaneous multi-parametric analysis of the physical and chemical features of up to thousands of cells per second [73]. Despite the capability to perform high-throughput analysis, however, standard flow cytometry techniques usually provide little morphological information over the flowing samples. While relevant cytological information can be collected from large amount of cells in very short time (100 to 100'000 cells per second), key parameters such as the cell size, shape, and morphology, as well as the distribution or location of biomarkers within the cells cannot be analyzed [74]. This could potentially pose severe limitations in applications where the cells morphology is of interest, as for instance in the case of early disease and

clinical diagnostics (e.g. cancer screening). The possibility to perform imaging of flowing samples represents, to this end, a major challenge for the technological advance of flow cytometry [75].

Recently, several approaches for imaging flow cytometry have been demonstrated which aims at integrating the high spatial resolution offered by optical microscopes into flow cytometry systems to achieve phenotypic characterization of cells at high rates. In this regard, mainly two classes of techniques have been developed [76].

The most common approach to imaging flow cytometry involves the use of widefield illumination coupled with a camera-based detection in order to obtain 2D images of cells. Imaging of the sample is usually achieved by employing CMOS or CCD cameras with high-sensitivity, to collect single or multiple field of views of the sample [77] [78]. Temporal multiplexing of the excitation light can also be used in order to improve signal-to-noise [79]. However, while these techniques have proven to be successful in assessing cellular morphology and distribution, they usually provide only information from 2D projections of the sample. Widefield illumination strongly limits the resolution and penetration depth of light into the sample, and the possibility to extract 3D information relies on the use of more complex structured illumination and severe post-processing algorithms (e.g. deconvolution).

The second type of flow imaging techniques involves the use of laser scanning (point scanning) systems coupled with single-pixel photodetectors, such as photomultiplier tubes (PMTs) or avalanche photodiodes (APDs) [76]. These techniques take advantage of the higher sensitivity offered by single-point detectors together with the intrinsic benefits of laser-based excitation – such as resolution and penetration depth – in order to provide blur-free images of the flowing samples. Nonetheless, while several techniques have shown remarkable performance for high-throughput, real-time imaging of cells [80] [75], very little has been demonstrated with respect to the possibility of performing 3D imaging of the flowing samples [81]. This

restriction is mainly due to the limited scanning speed, especially in the axial direction, of current laser scanning systems. As the standard methods to achieve high-speed 3D imaging (see section 2.2) fail to adapt to flow cytometry applications, imaging in scanning systems is usually constrained to 1D line scanning instead of 2D cross-sectional scanning.

Here, we implement a flow imaging system capable of performing high-speed cross-sectional imaging of cells flowing through a microfluidic chip. Our implementation relies on coupling an acoustic lens into a commercial confocal microscope in order to axially scan the focus at kHz rates [51]. By combining the axial scanning capabilities offered by the acoustic lens with line scanning, we are able to collect cross-sectional images at rates up to 1 kHz. We employ this technique to perform B-scan imaging flow cytometry, and demonstrate the possibility to retrieve morphological information of individual cells and cell clusters, therefore paving the way for the study of cellular morphology, intercellular interactions, and evaluation of cell clusters also in flow cytometry experiments.

2.5.1 Optical system

The optical setup for imaging flow cytometry consisted of a commercial confocal microscope (Nikon A1R, Nikon Instruments Inc., Tokyo Japan) equipped with four excitation CW lasers (405 nm, 488 nm, 561 nm, 640 nm) and a resonant scanner. All the experiments were performed using a 20X (Nikon Plan Apo CFI, NA 0.8, Nikon Instruments, Japan) objective lens. An acoustic optofluidic lens (TAG lens 2.0, TAG Optics Inc., Princeton, New Jersey, USA) was used to achieve high-speed axial scanning. In order to place the acoustic lens in the commercial setup, we inserted a relay lens pair (f = 200 mm) between the tube lens and scan lens of the microscope (Figure 2.12). The lens was then positioned between the relay lenses, so that the TAG lens was conjugated with the scanner as well as the back focal

plane of the objective lens. For all the experiments, we drove the acoustic lens near the 143 kHz resonant frequency, and with a voltage amplitude of 23 V_{pp}. In order to match the effective numerical aperture of the TAG lens, which corresponded to 6 mm, we placed an aperture of the same size in front of the lens.

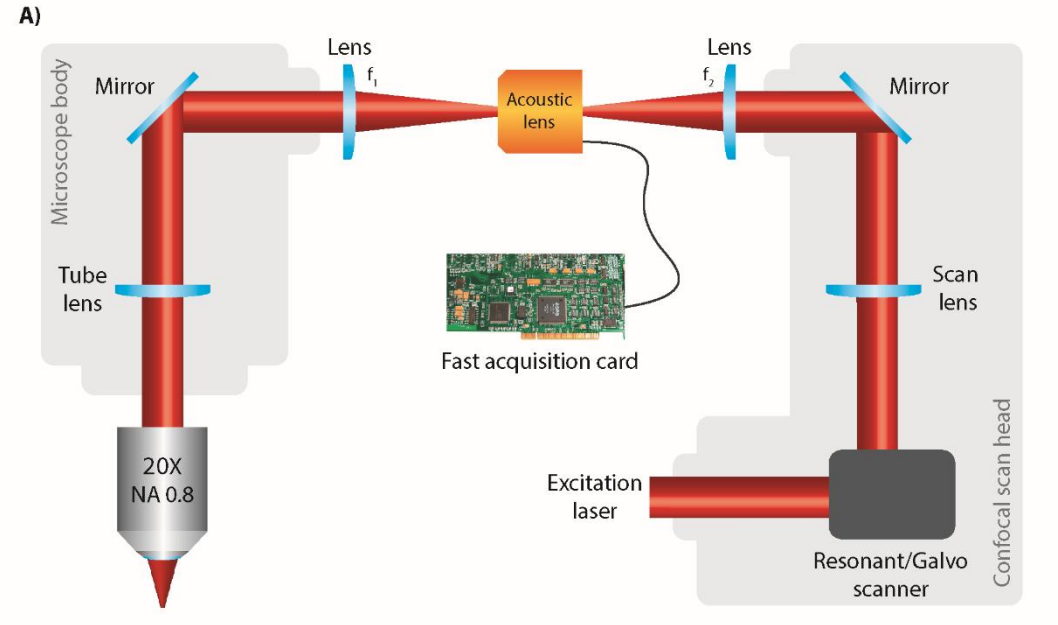

Figure 2.12 Scheme of the confocal setup used for imaging flow cytometry. A relay lens system was inserted right after the microscope scan head in order to position the acoustic lens. Demodulation of the collected signal was performed by using a fast acquisition card.

The pinhole in front of the TAG lens reduced the beam diameter of the excitation laser, causing under-filling of the back aperture of the objective lens. To retrieve the information related to the focal length of the acoustic lens as a function of time, we measured the intensity of a CW laser source (657 nm) that passed through the lens slightly off its axis by means of a photodiode (Thorlabs PDA36A Si Switchable Gain Detector, 350-1100 nm). Because the CW laser was deflected with an angle that linearly depended on

the focal length of the acoustic lens, the photodiode collected an intensity signal modulated accordingly. On the detection side, we used a fast acquisition card (Becker and Hickl DPC-230, ~180ps time resolution) synchronized with the XY scanner of the microscope (pixel, line and frame feedback signals), and with the photodiode (Figure 2.12). Finally, we implemented custom-made software, written in Python language, to perform the image processing of the acquired data and the temporal photon sorting.

Sample preparation: HeLa-miRFP703 cells were grown in DMEM medium (Dulbecco's Modified Eagle Medium, Thermo Fisher Scientific, Massachusetts, USA) supplemented with 10% FBS (Fetal bovine serum, Sigma-Aldrich, Missouri, USA), 1% penicillin-streptomycin, 1% glutamine, and 0.5 mg/ml of antibiotic G418. To label mitochondria and plasma membrane, we incubated $3x10^6$ cells with CellMask Green and MitoTracker Orange (Thermo Fisher Scientific, Massachusetts, USA) at the dilution 1:100 and 1:1000 respectively, at 37 °C and 5% CO2 for 30-45 minutes. After, we centrifuged the cells at 300xg for 5 minutes and suspended in Live Cell Imaging Solution (Thermo Fisher Scientific Massachusetts, USA) to perform the flow imaging experiments.

Microfluidic chip fabrication: A microfluidic channel with a squared-section of 130 μm (Figure 2.13A) was fabricated in polydimethylsiloxane (PDMS) using single-step soft lithography. More in detail, photolithography was used to first pattern a master into a layer of 260-μm-thick SU-8-100 photoresist applied on top of a 4-in. silicon wafer by spin coating. Once the photoresist master was ready, the PDMS prepolymer was poured onto the master with a cross-linker (mass ratio 10:1), degassed in a vacuum for 30 min, and cured at 60 °C for 1 h. After curing, the microfluidic chip was sealed to a microscope coverslip by O_2 plasma bonding (RF power 60 W, exposure time 20 s) in order to allow for optical imaging from the coverslip side. Active flow of both fluorescent beads and cells was induced into the microfluidic channel by using a syringe pump (Nexus 6000, Chemyx) operated in withdrawing mode.

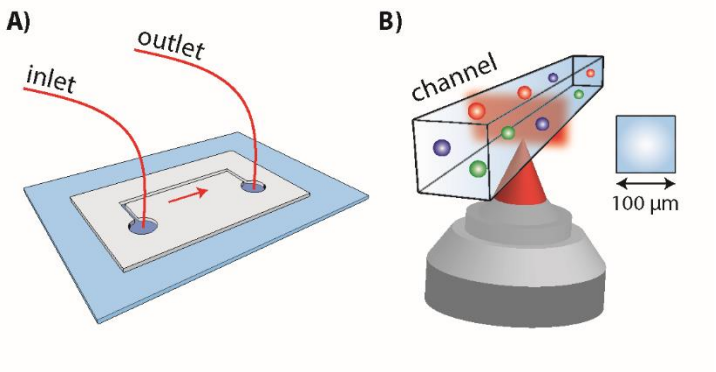

Figure 2.13 (A) Schematic representation of the fabricated microfluidic chip. After fabrication, the channel was sealed to a microscope coverslip by plasma bonding in order to allow for optical imaging. (B) An inverted imaging configuration was adopted to collect images of the flowing samples.

2.5.3 Microscope characterization

Before investigating the flow imaging capabilities of our microscope (x,z,t), we started by inspecting its ability to collect extended depth of field information on a pixel-by-pixel basis (z,t). Hence, we collected volumetric images (x, y, z, t) of 0.2 µm fluorescent beads dispersed in agarose to characterize the lateral and axial PSF of the system. To compare the performance of the microscope without and with the use of the TAG lens, we acquired two 3D stacks (with lens off and lens on, respectively) using the microscope stage to translate the sample over a Z range of 100 µm. For this experiment, we drove the lens at 143 kHz, while the voltage was set at 23 V_{pp}, and the pixel dwell time corresponded to 1 ms. In agreement with our expectations, when the acoustic lens was turned on (Figure 2.14), the excitation beam was scanned multiple times over the z-axis at each pixel, and consequently, integration of the signal from each pixel resulted in an extension of the axial PSF FWHM from 8 µm to about 60 µm (Figure 2.14B).

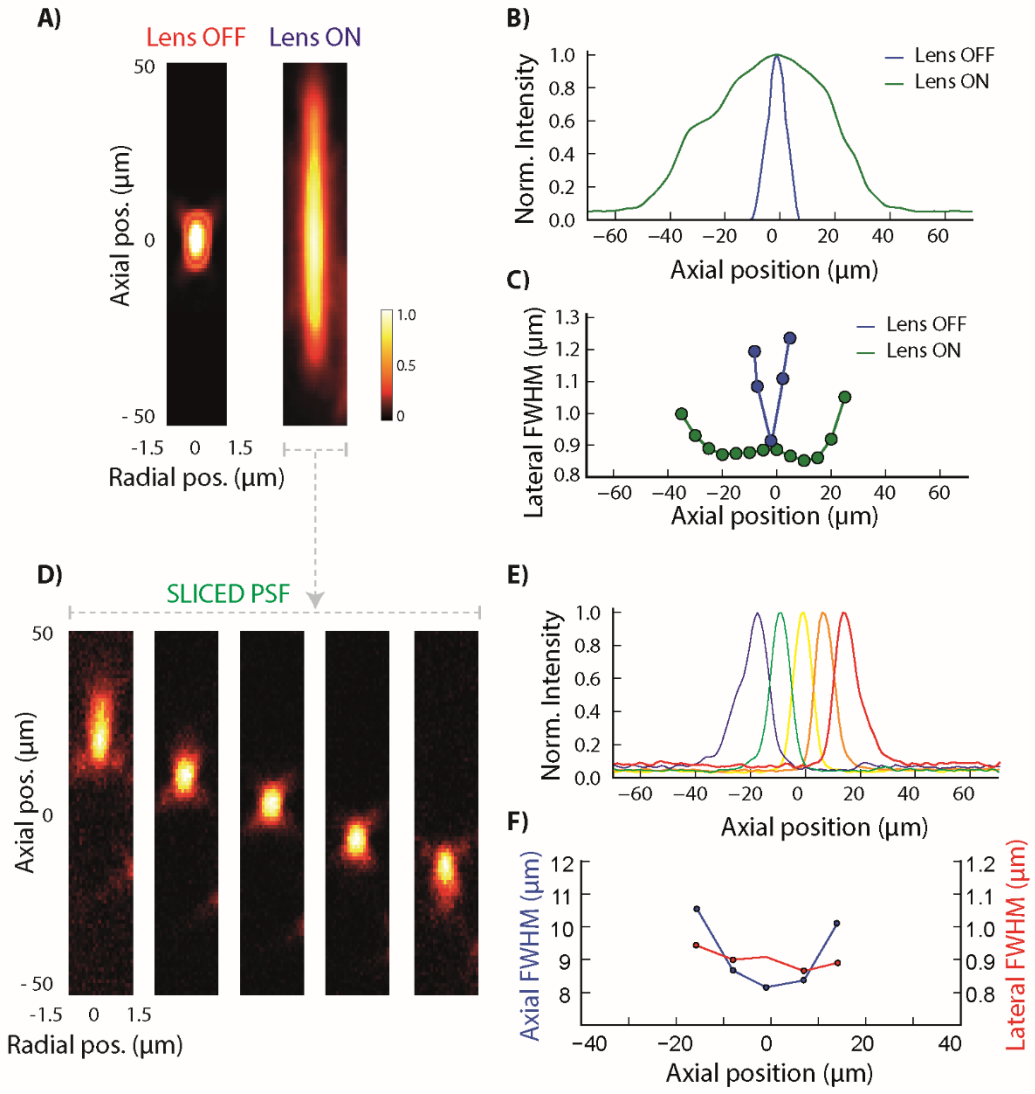

Figure 2.14 Experimental PSF characterization. (A) Standard PSF of the microscope with the acoustic lens off and extended PSF obtained with the lens on. B) Intensity profile of the axial PSF with the acoustic lens off (red line) and on (blue line) and C) corresponding plots of the FWHM of the lateral PSF vs axial position. (D) Representative PSFs corresponding to 5 different focal planes reconstructed from the temporal information of the detected photons during acoustic lens *z*-scanning (SLICED PSF). E) Axial PSF characterization of the 5 representative planes shown in (A), and (F) corresponding plots of the lateral and axial FWHM of the PSF vs axial position.

Notably, the lateral PSF was preserved throughout the whole scanning range (average FWHM = 0.87 μm), as compared to the in-focus PSF with lens off (FWHM ≃ 0.91 μm) (Figure 2.14C). As in the case of 2PE microscopy described in section 2.4, the elongated PSF can be used to collect an EDOF image or, by properly demodulating the collected signal, to obtain multiple PSFs, each one corresponding to a different focal plane [24]. In this respect, Figure 2.14D shows an image of the reconstructed PSFs for five representative planes. The FWHM of the lateral PSF for each of these planes is 0.86±0.02 μm (Fig. 3E). The FWHM of the axial PSF is 8.2 μm for the plane located at $z = 0$ μm (native focal plane of the system) and progressively increases up to 12.4 μm for planes located at $z = \pm 20$ μm due to spherical aberrations (Figure 2.14F). With this optical configuration, our microscope was able to axially scan the focus at high speed – time to perform an axial scan was 7 μs – over an axial range of 60 μm, therefore providing a Z travel range which covered almost 50% of the section of the microfluidic chip.

At this point, we characterized the flow imaging capabilities (x, z, t) offered by our microscopes by imaging flowing 1 μm fluorescent beads. Being assembled onto a glass coverslip, the microfluidic circuit was positioned in the microscope stage in the same way as for a standard sample. This represents an inherent advantage offered by our setup, as most optical systems used for imaging flow cytometry or flow characterization require orthogonal illumination and dedicated setups [82]. Imaging of the channel was performed from below, according to the scheme presented in Figure 2.13B. The inlet and outlet of the chip were connected to a reservoir containing fluorescent beads dispersed in water, and to a syringe pump operated in withdraw mode, respectively. The native focal plane of the system ($z = 0\,\mu m$, acoustic lens off) was positioned at the centre of the channel. Thus, when switching the lens on, 30μm above and 30μm below that plane were properly imaged.

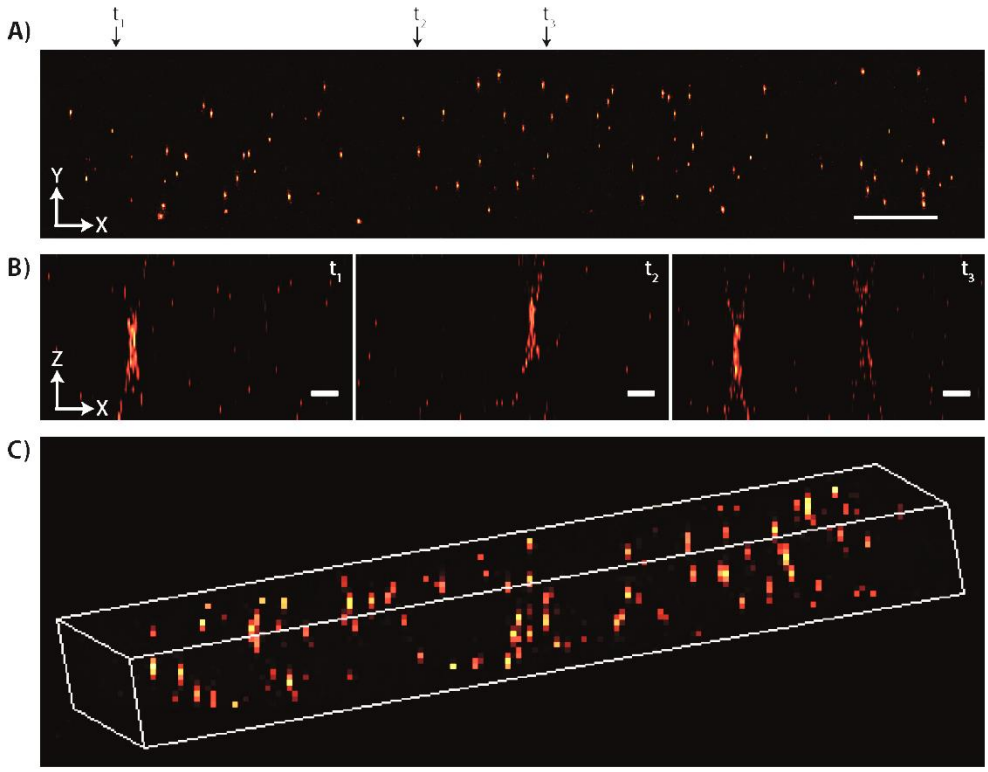

Figure 2.15 Fluorescent beads flow imaging. (A) Extended depth of field image acquired with the acoustic lens on. The image corresponds to an acquisition of 10 seconds and shows the fluorescent beads flowing through the channel. Scale bar 50µm. (B) Cross-sectional images obtained by using the multiplane imaging approach while performing a line scan. D) Rendering of a 3D image from the imaged volume. Scale bars 10µm.

Because of the parabolic velocity profile of low Reynolds number flows, such as that found in a microfluidic channel, the scanned region covered the parts of the channel where the beads travel at the fastest speed.Finally, the lateral displacement for cross-sectional imaging was achieved by performing a line scan along the X-axis (perpendicular to the flow direction) by using the microscope controlling software. In this particular experiment, we set a line scan of 256 pixels with a pixel size of 0.45 μm so to cover the entire lateral extension of the channel. The line scan rate was set to 128 $lines/s$.

We then used the syringe pump to induce an active flow into the channel at a flow rate of $1\mu L/min$, resulting in a maximum flow speed of about 3.5 mm/s and an average flow speed of 2.3 mm/s. We waited several minutes before each acquisition in order to enable the fluidic system to stabilize to a constant flow rate.

By operating our system in cross-sectional imaging modality (x, z, t), images of the flowing beads as a function of time can be collected. Figure 2.15A shows a top-view EDOF image of the channel obtained after 10 seconds of acquisition (1280 scan lines). In addition, by applying the multiplane imaging approach previously described, information regarding the axial position of each single bead can also be retrieved. Figure 2.15B reports cross-sectional images (x, z) of the channel acquired at three different time instants. Finally, the reconstructed axial planes can be combined together in order to obtain a 3D reconstruction of the flowing fluorescent beads (Figure 2.15C).

2.5.4 High-speed cross-sectional imaging of living cells

As a proof-of-concept to demonstrate the flow imaging capabilities of our microscope, we performed imaging of flowing living cells. We loaded the microfluidic chip reservoir with a solution containing Hela-cells at a concentration of $10^3 cells/ml$. As in the previous experiment, we used the syringe pump in withdrawal mode to induce an active flow of the cells into the channel. In this case we used a flow rate of $50nL/min$. We selected a line scan of 256 pixels with a pixel size of 0.45 μm and a scan rate of 512 $lines/s$. The acoustic lens was driven at 143 kHz, voltage was set at 23 V_{pp}, as for the previous experiments. After waiting few minutes for the flow rate to stabilize, we collected cross sectional images of the flowing cells.

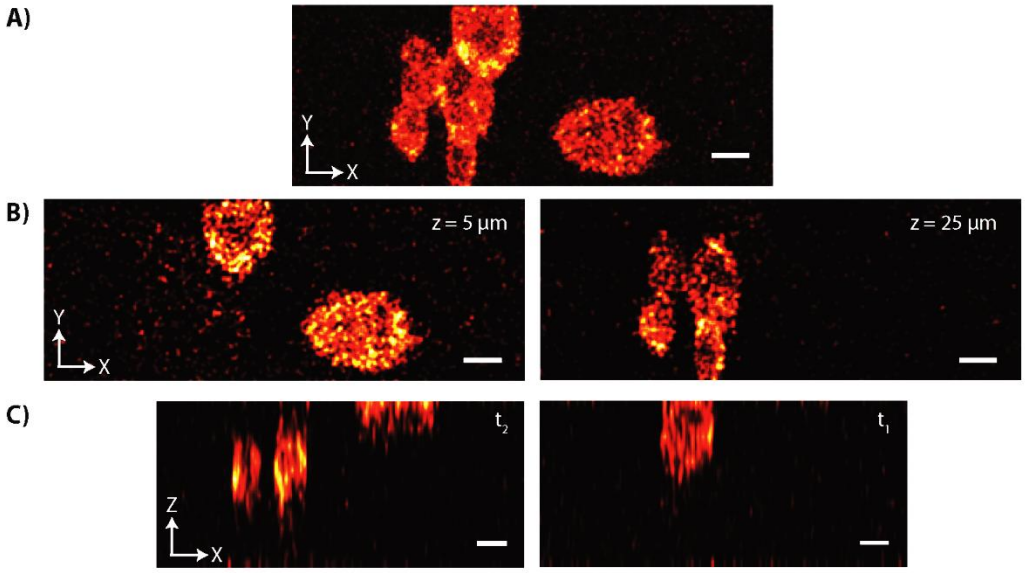

Figure 2.16 Cells flow imaging. (A) Top-view image captured with the acoustic lens on showing a cluster of cells flowing through the microfluidic channel. (B) Images of the cell cluster obtained using multiplane imaging approach. The two images are located at two different axial positions (z=5µm and z=25µm). (C) XZ cross-sectional images of the cells retrieved from the multiplane imaging information. Scale bars 10µm.

Figure 2.16A presents an EDOF image corresponding to acquisition of about 0.67 seconds (345 lines), obtained with the acoustic lens on. Several cells can be distinguished as they flow through the channel section. Notably, instead of being limited to a single 2D acquisition, EDOF cross-sectional imaging enables to collect information from almost the entire cross-section of the channel. However, no information regarding the axial position of each cell is provided. To this end, the exact Z position of the cells can be retrieved by applying the multiplane imaging approach. By using the temporal information of the collected photons, images of multiple axial sections can be obtained.

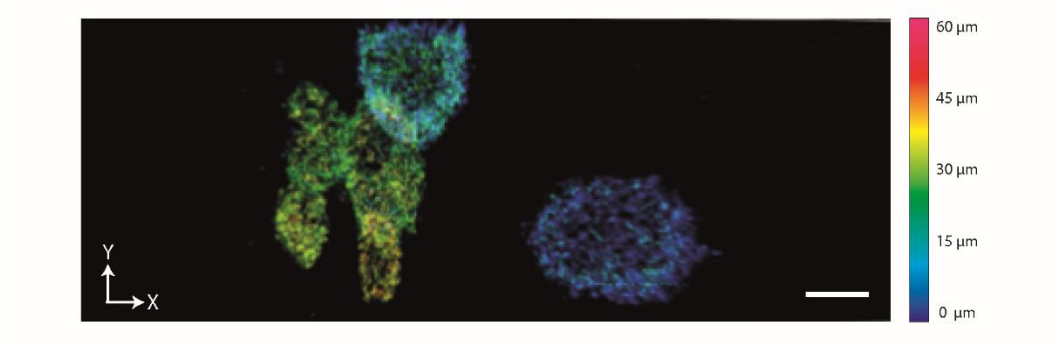

Figure 2.17 Z-depth color-coded images of flowing cells. The image shows a z-depth color-coded representation of the cell cluster shown in Figure 2.16. The axial distribution of the cells spans over an axial range of about 50 µm. Scale bar 10µm.

Figure 2.16B and C show respectively, XY sections obtained from two different axial positions within the channel, and XZ cross-sectional images obtained from two different time instants. Note that in this case, the axial location of each cell within the channel can be clearly distinguished, thus allowing to render a 3D reconstruction of the imaged volume. In this regard, Figure 2.17 shows Z-depth color-coded representations of the imaged cell clusters where the axial position of each cell within the cell aggregate can be better appreciated. By means of an acoustic optofluidic lens, our system is therefore capable of performing cross-sectional measurements which can, in turn, be used for imaging flow cytometry applications. In addition, the possibility to use multicolor stimulation makes it possible to eventually monitor multiple flowing samples expressing different fluorescent markers.

2.6 Conclusions

Our approach for pixel-based z focus control can be used to significantly increase the capability of standard LSMs. The use of ultrafast beam shaping on a pixel by pixel basis enables improved axial acquisition speed in confocal as well as 2PE microscopy, together with an increased imaging depth capability. A standard LSM setup can be provided with beam shaping capabilities with the integration of an acoustic optofluidic lens into the excitation pathway of the system, together with the use of a fast acquisition card for appropriate demodulation. By simply adjusting the driving frequency of the lens, different imaging modalities can be obtained. In this way, when the lens is driven with a parabolic phase profile, fast axial focus scanning can be achieved at each pixel. The collected signal can be combined for EDOF imaging, or de-multiplexed into different time intervals for volumetric imaging. In any case, fast 3D imaging can be performed at rates similar to those currently used for imaging a standard 2D section. The possibility to collect axial information on a pixel by pixel basis enables for different imaging architectures and opens up new possibilities for the use of LSMs in applications such as imaging flow cytometry and high-speed volumetric imaging. In addition, by using the acoustic lens in order to induce controlled aberrations in the excitation pathway, enhanced S/B imaging can be achieved by means of a simple subtraction algorithm. Contrary to other approaches, all information required for background rejection is acquired simultaneously at each pixel, suppressing potential motion artifacts. Finally, no need for cumbersome customization is needed, and a commercial LSM can be provided with beam shaping capabilities with minimum modifications. Our electronically tunable and ultrafast beam shaper is a novel and simple approach to enhance the performance of existing laser scanning microscopes, which paves the way for investigating complex biological phenomena at high temporal resolutions and over deep penetrations depths.

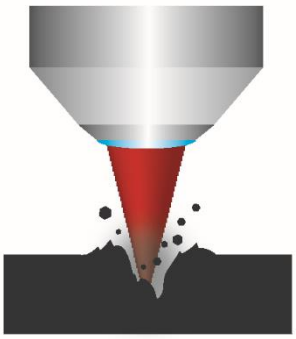

Chapter 3

Laser fabrication using engineered materials and shaped light

Current trends toward the fabrication of small customized units render laser-based fabrication techniques particularly suitable for 2D and 3D fabrication. By simply translating the laser focus within the material, laser direct-write (LDW) methods allow for the processing of a wide variety of materials with no need of expensive masks or clean room facilities. However, the optical nature of laser-based systems strongly constrains the fabrication capabilities of this technology, with parameters such as minimum feature size, spatial resolution and depth of the fabricated structures typically in the order of microns. In this chapter, we present a novel strategy to overcome the intrinsic limits of LDW techniques. Our approach relies on the use of engineered materials whose shape can change according to an applied external stimulus, such as mechanical force or heat, thus enabling to decouple feature size from the interaction of laser with materials. Indeed, irradiation of such materials can result in structures with a size dictated by light-matter interactions. However, after applying an external stimulus, the material can be reconfigured, consequently reducing the size of the structures beyond the limits imposed by the initial light interaction.

3.1 Introduction

Since the advent of semiconductors and microelectronics industry, miniaturized devices have become ubiquitous in our everyday life. From the production of mobile phones and computers to the creation of more advanced engineered systems, miniaturized components constitute the essential units in many technological applications [83]. As a result, while current trends toward miniaturization demands for ever smaller mechanical, optical and electronic systems, the development of proper techniques to fabricate these devices is of utmost relevance.

Arguably, the gold standard approaches for micro- and nano-fabrication are photo-lithographic processes [84,85]. Based on the polymerization of a resist layer using light that passes through a mask, they offer the possibility to fabricate large structures with a precision reportedly below 100 nm. However, they can be limited by an inherently short parameter space – planar substrates and reduced number of compatible materials – and by the need for complex multistep fabrication processes as well as expensive instrumentation, including clean room facilities. In addition, lithographic approaches are mostly optimized for 2D fabrication, typically rendering the creation of 3D structures challenging. In as much, the high production costs of the masks or molds required also render these techniques suitable for large-scale fabrication of identical units, but fail to accommodate the demands in terms of cost and time for the production of small customized units [86].

A promising alternative to lithographic methods is represented by direct-writing techniques, based on the creation of patterns without masks or intermediate steps. A paradigmatic example of these techniques is represented by laser-direct write systems [87–89,20]. By simply scanning a laser across a sample, and thanks to the high focusing power of lasers, it is possible to induce localized modification of a material with a reduced

number of processing steps. Control of the laser parameters such as wavelength, pulse duration or intensity, enables to use lasers to either remove parts of a workpiece, as it occurs in laser ablation, or to add new materials into targeted areas, as in laser photo-polymerization [90] or laser-induced forward transfer [86,91]. The possibility to achieve both subtractive and additive manufacturing is complemented with the potential use of virtually any material, as long as it interacts with the laser wavelength [87]. Additionally, the use of lasers as writing tools allows for the development of 2D and 3D structures with complex geometries while working in standard ambient conditions [19,92], further enhancing the capabilities of such systems for micro- and nanofabrication.

Despite the advantages offered by laser-based fabrication techniques, two main constraints ultimately limit the minimum feature size of the fabricated structures. First, the optical properties of the setup. Indeed, the minimum laser spot size is determined by the diffraction limit, which is about half the processing wavelength for air objectives. Second, the interaction between the laser and the material. This interaction defines the final shape of the fabricated structures. Even if non-linear absorption processes can be used to confine the modified area within a sub-region of the laser spot [93], these processes are typically difficult to control. In fact, when laser fluences are close to the threshold for material modification, potential laser power fluctuations or material non-uniformities can compromise the quality and size of the fabricated structures. Thus, it is typically desirable to operate at conditions well above the threshold for modification, limiting the minimum feature size of laser-based processes to approximately the diffraction-limited spot size.

In this chapter, we focus our attention on the development of novel strategies for improving the spatiotemporal resolution of laser-direct write systems. This is in analogy to the previous chapter, in which we aimed at improving the spatiotemporal resolution of optical microscopes, but instead of improving the temporal resolution without sacrificing the spatial one as

previously demonstrated, in this chapter we aim at the opposite: improving the spatial resolution while preserving the inherent speed of laser systems. More in detail, we propose a new method to overcome spatial resolution constraints of current LDW systems, and achieve smaller features than currently possible. The core concept of our strategy is to use engineered materials, namely materials which can be reshaped in response to an external stimulus [94]. The proposed technique consists of two fabrication steps: first, the desired structure is obtained through standard laser modification; second, material reconfiguration is induced through an external stimulus in order to reduce the final size of the structure (Figure 3.1). In this way, it is possible to decouple the feature size from the initial laser irradiation step, opening the door to true laser nanofabrication.

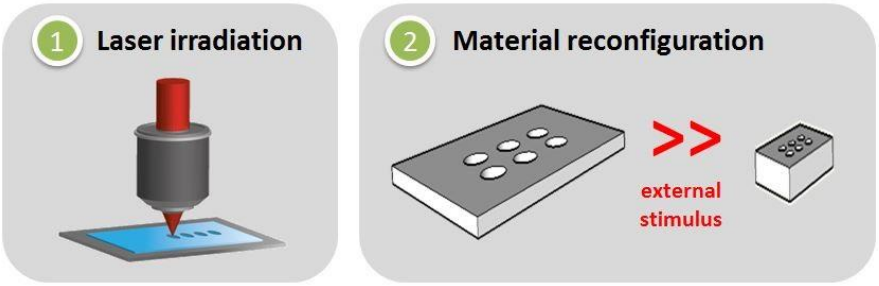

Figure 3.1 Scheme of the fabrication steps for laser-based fabrication of engineered materials.

To demonstrate the capabilities of our method, we perform ultrafast laser processing of pre-stretched elastomers [94] and heat-shrinkable polymers [95] and fabricate user-designed 2D and 3D structures. Importantly, the use of a femtosecond laser enables highly localized energy deposition with minimal thermal effects [96]. Moreover, because material modification only occurs within the focal volume via nonlinear absorption, high-precision manufacturing can be achieved at the surface as well as in the bulk of the material. As shrinkage of the polymers in response to the

external stimuli (release of tension or heat-induced shrinkage) results in a reduction of the lateral dimensions together with an increase in thickness [95], deep sub-wavelength structures can be obtained with sizes and aspect ratios not achievable with current LDW techniques. Finally, by combining engineered materials with non-conventional beam shapes such as Bessel beams [31], further flexibility in the design of the nanostructures becomes possible. In this regard, we use Bessel beams to achieve uniform energy deposition over extended lengths [97] and demonstrate the fabrication of ultra-high aspect-ratio (>50) through-hole microchannels. Our results represent a step forward in the use of LDW technologies for 2D and 3D fabrication at the micro- and nanoscale. As new engineered materials are being developed, the current method could indeed pave the way for the use of laser systems as economic, flexible and customizable nanofabrication tools.

3.2 Optical system

The optical setup for laser direct-writing consisted of a 100 kHz Ti:sapphire amplifier (Coherent, Inc.) tuned at a wavelength of 800 nm, with a pulse duration of 100 fs. As illustrated in Figure 3.2, the laser beam was focused on the sample by using either a 10X NA 0.28 (Plan Apo Infinity Corrected Long WD Objective, Mitutoyo, Inc.) or a 50X NA 0.55 objective lens (Plan Apo Infinity Corrected Long WD Objective, Mitutoyo, Inc.). In order to control the laser power, we used two neutral density (ND) filters and a rotating λ/2-waveplate. Constant monitoring of the laser pulse energy was obtained by a beam splitter and a laser-energy meter (Coherent Inc.). For the fabrication of 2D and 3D structures, we moved the sample with respect to the laser focus using an XYZ motorized stage (Prior Scientific, Inc.) with micrometer resolution (0.01μm in X and Y, and 0.002 μm in Z), translation speed up to 150 mm/s, and travel ranges of 112 mm × 112 mm × 73mm. In the case of

fabrication of high aspect ratio structures, we used shaped light in the form of a Bessel beam. To this end, we equipped the optical system with an axicon lens (Plano-Convex Axicon, apex angle 178°, Altechna) (Figure 3.2, inset). The Bessel beam generated by the axicon was imaged at the focal plane of the objective lens by means of a 4f system conjugated with the back focal plane of the objective (Figure 3.2).

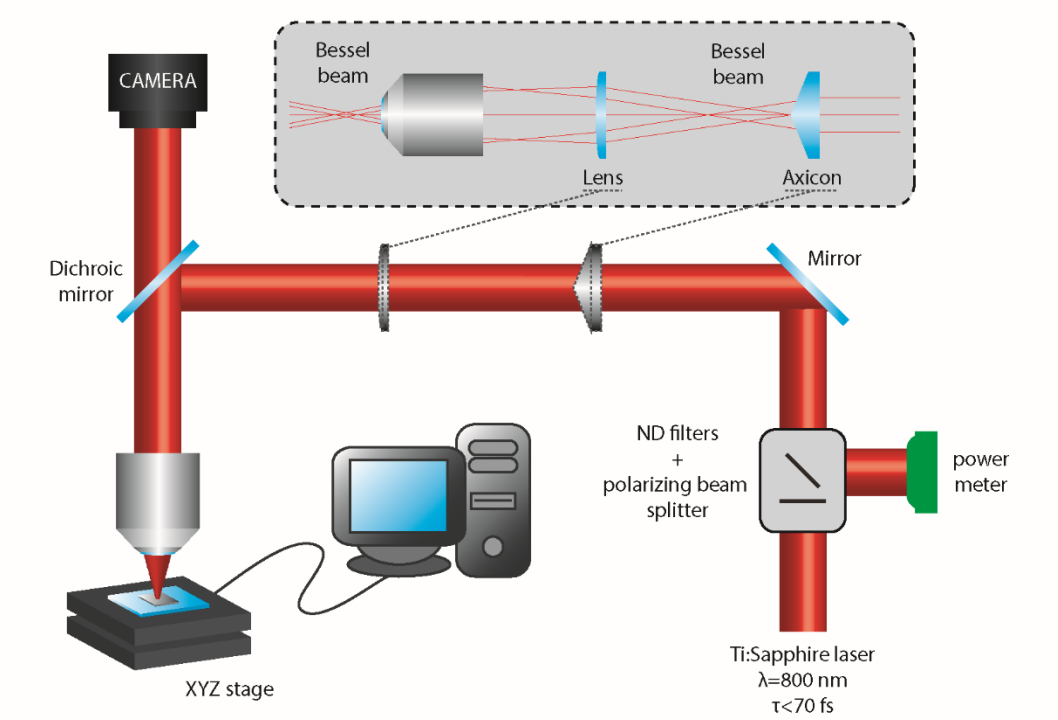

Figure 3.2 Optical system used for laser direct-writing. A femtosecond laser source was focused on the sample by means of a 10X or a 50X objective lens. Inset: laser fabrication using shaped light. In case of 3D fabrication, an axicon lens was inserted in the setup together with a relay lens in order to obtain a Bessel beam at the objective focal plane.

Finally, imaging of the sample during fabrication was performed with a CCD camera (DCC1645C, Thorlabs Inc.) coaxially placed with respect to the laser beam. The focal plane of the camera was selected to be confocal with the

laser focus so that the imaged at the CCD gave a good estimation of the position of the laser beam waist. We used Kohler illumination to illuminate the sample with a white LED light source. Custom software, written in LabView language, was used to control and synchronize the laser unit with the stage displacement.

3.3 Laser-based fabrication of pre-stretched elastomers

Our first attempt to demonstrate the possibilities offered by laser processing of engineered materials was performed with elastomers, namely polymers which typically show excellent elastic properties (low Young's modulus) and high failure strain compared to other materials [98]. In particular, we used the previously described LDW system to fabricate user-designed 2D patterns on the surface of uniaxially pre-stretched poly(dimethylsiloxane) (PDMS) membranes [94].

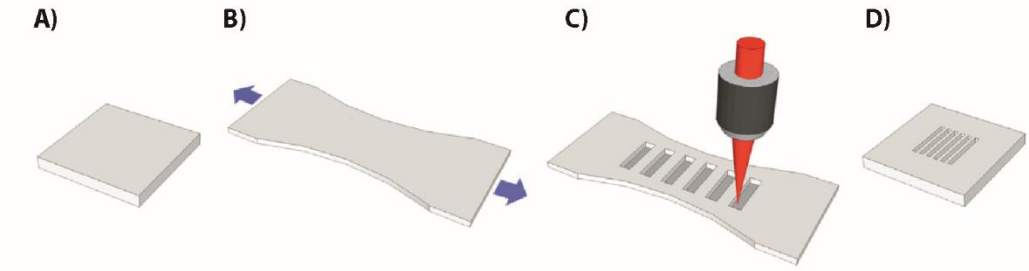

Figure 3.3 Schematic diagram of the fabrication process. (A) The starting material is a thin elastomeric membrane with initial length L_0; (B) the membrane is uniaxially stretched until it reaches the desired length L_1 and thus the desired mechanical strain; (C) direct laser writing of the desired pattern into the pre-stretched elastomeric membrane; (D) By releasing the mechanical stress the size of the laser-ablated patterns scales down according to the amount of mechanical strain applied to the elastomeric membrane (C).

The choice of PDMS, a silicon-based elastomeric material optically transparent, inert, non-toxic and biocompatible, is mainly due to its elastic properties [99]. Indeed, it enables large deformations, making it a suitable candidate to validate our approach, as illustrated in Figure 3.3.

We start with a thin elastomeric membrane of length L_0. The membrane is then uniaxially stretched up to a length L_1, therefore corresponding to a mechanical strain $\varepsilon = (L_1-L_0)/ L_0$ (Figure 3.3B). At this point, laser irradiation is performed according to the desired pattern (Figure 3.3C). Finally, as the mechanical stress is removed, the membrane relaxes to its original size, and the laser ablated pattern shrinks while preserving its shape (Figure 3.3D). In this way, independently from the laser irradiation step, we are able to obtain a reduction in the minimum feature size that is proportional to the elongation of the membrane. Within the following sections, we report results from the fabrication of arrays of periodic lines under different strain conditions and compare the experimental results with the theoretical predictions based on the strain experienced by the elastomers during the laser ablation process.

3.3.1 Laser patterning of pre-stretched elastomers

Among the wide family of PDMS-based elastomers, we used Syligard poly(dimethylsiloxane) (PDMS), and acetoxy-polysiloxane (acetoxy-PDMS [100]. Figure 3.5A shows the typical tensile stress-strain curve for both PDMS (red line) and acetoxy-PDMS (blue line). Both the elastomers exhibit non-linear stress-strain curve typical of rubber-like cross-linked polymers [100]. The superior elasticity of the acetoxy-PDMS with respect to the PDMS is evident can be observed in Figure 3.4. The maximum strain before mechanical fracture of the membrane occurs is $\varepsilon_{max} = 4$ for PDMS, and $\varepsilon_{max} = 10.5$ for acetoxy-PDMS. This result is confirmed by several tensile stress-strain tests performed on both PDMS and acetoxy-PDMS membranes

in the same nominal conditions (i.e. chemical compositions of the pre-polymers, curing conditions, stretching rate). In particular, we experimentally found a mean value and standard deviation of ε_{max} = 3.6 ± 0.4 for PDMS and ε_{max} =10.8 ± 0.9 for acetoxy-PDMS. The superior elasticity properties of acetoxy-PDMS, in particular, the low stress needed to reach strain values close to 4, make it the material of choice for our current experiments.

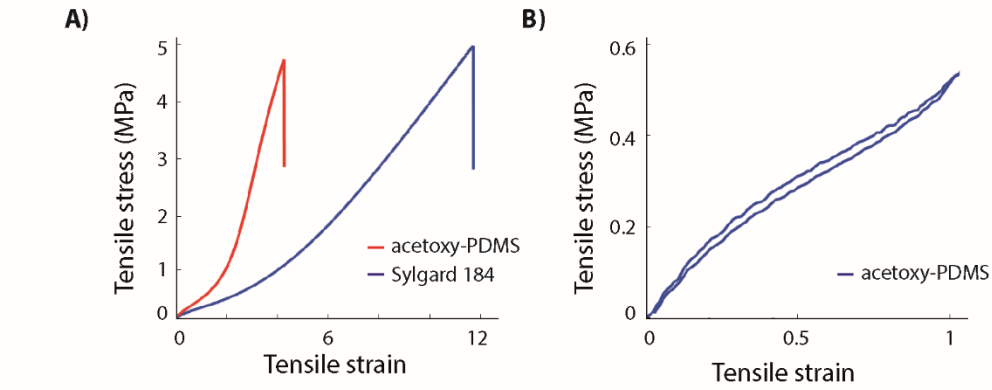

Figure 3.4 (A) Tensile stress-strain curves for Sylgard PDMS (redline) and acetoxy-PDMS (blue line). The strain at which the mechanical fracture occurs defines the elongation at break. (B) Uniaxial tensile test for acetoxy-PDMS membrane subject to a single loading-unloading cycle.

Figure 3.4B shows the stress-strain curve of the acetoxy-PDMS subjected to cyclic tensile test. The acetoxy-PDMS shows a negligible amount of hysteresis during cyclic loading. In particular, after the first uploading-unloading cycle the membrane exhibits a residual mechanical strain (i.e. residual elongation of the membrane) of $\varepsilon_{res} \approx 0.03$ and corresponding to about the 3% of the maximum strain exploited during the cyclic tensile test. This residual strain could be due to a rearrangement of the polymeric chain in the acetoxy-PDMS as well as to clamping losses of our experimental setup. The effects of laser pulse energy on the size of structures obtained by

femtosecond laser ablation of the acetoxy-PDMS membrane are shown in Figure 3.5. In particular, we fabricated periodic parallel lines by irradiating the non-stretched membrane with laser pulses of different energies, while maintaining a shot to shot separation of 500 nm. Line-width values from 0.9 to 2.8 μm were obtained for pulse energies ranging from 63 to 360 μJ.

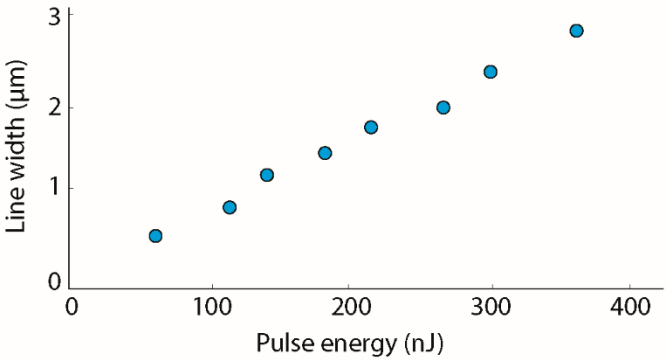

Figure 3.5 Width of the fabricated lines as a function of the used laser pulse energy for a non-stretched acetoxy-PDMS membrane.

Notably, at an energy of 63 nJ, the acetoxy-PDMS membrane is still ablated, but the resulting lines are discontinuous. For even lower energies, no ablation is observed. This suggests that the threshold energy for laser ablation of the acetoxy-PDMS is about 63 nJ, and discontinuities in the ablated lines can be attributed to fluctuations in laser energy or to potential imperfections of the elastomeric membrane, i.e. the surface roughness. Therefore, the minimum line width that can be fabricated with our current optical setup for a non-stretched acetoxy-PDMS membrane is of about 0.9 μm at an energy pulse value of 115 nJ.

In order to overcome this spatial limitation, we performed laser-ablation of pre-stretched membranes. More in detail, we prepared arrays of lines at a fix laser pulse energy of 215 nJ and a shot to shot separation of 500 nm. In

this case, the membrane was irradiated while subject to different mechanical strains ranging from 0 to 4 (i.e. membrane elongation from 0 to 5). After releasing stress, we expect an enhancement in terms of both pitch (P) and width (W) of the ablated periodic lines according to the following equations:

$$P_\varepsilon = \frac{P_0}{1+\varepsilon} \tag{3.1}$$

$$W_\varepsilon = \frac{W_0}{1+\varepsilon} \tag{3.2}$$

where, the subscript $_0$ and ε corresponds to non-stretched and stretched acetoxy-PDMS, respectively, with ε referring to the mechanical strain of the elastomer during ablation. Figure 3.6 shows confocal images of the femtosecond laser-ablated lines after releasing of the mechanical stress. In all cases, during the ablation process, the spacing between two consecutive parallel lines was maintained at P_0 = 50 µm. All ablated lines are well-defined and present minimal debris, especially at low mechanical strain (ε<4).

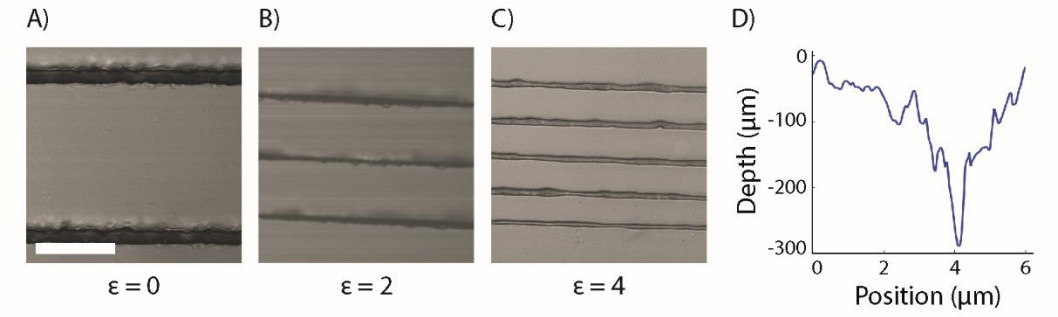

Figure 3.6 (A-C) Optical images of laser-ablated periodic lines of the acetoxy-PDMS membranes subjected to a mechanical strain of 0, 2 and 4. (D) AFM cross-section depth profile curve of one of the laser ablated lines of (C). Scale bars are 25 µm.

This illustrates the suitability of femtosecond lasers as a tool for patterning elastomeric materials. In addition, a significant reduction of the lines pitch (P_ε) can be clearly observed for lines obtained under strain conditions. In particular, the line pitch decreases from 50 μm when no stress is applied, to 17.88 μm for ε = 2 and to 10.2 μm for ε = 4. Quantification of the reduction in line pitch is presented in Figure 3.7. In this case, we plotted the experimental (blue symbol) and theoretical (solid line) normalized line-pitch (p), by definition $p=P_\varepsilon/P_0$, as a function of mechanical strain (ε). Notice that, experimental data are in good agreement with theoretical predictions. Therefore, our approach enables a user-tunable line-pitch by simply modifying the amount of mechanical strain experienced by the membrane during ablation. The reduction in line-width (W_ε) can also be determined from Figure 3.7. In this case, we found a value for W_ε that ranges from 2.7 ± 0.2 μm when no stress is applied to the membrane, to 1.1 ± 0.1 μm for ε = 2 and to 1.1 ± 0.1 μm as ε reaches a value of 4.

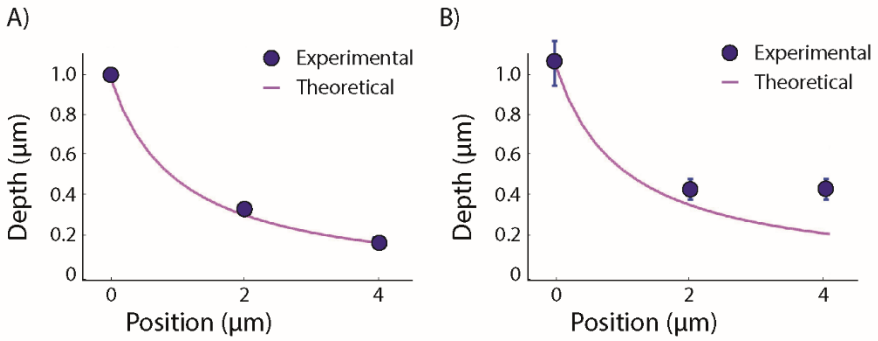

Figure 3.7 Experimental (blue symbol) and theoretical values (pink solid line) of normalized pitch (A) and normalized width (B) of laser-ablated periodic lines as a function of the applied strain.

The plot of the experimental (blue symbol) and theoretical (solid line) normalized line-width (w), by definition $w = W_\varepsilon/W_0$, as a function of mechanical strain ε is shown in Figure 3.7. The value of 1.1 μm obtained at the highest tested strain is apparently in contrast with the theoretical prediction expected from Equation 3.2, which should result in a line-width of 0.54 μm. Such difference could be attributed to non-propagating micro-fractures, i.e. micro-cracks, surrounding the irradiated regions of the pre-stretched elastomer. Though the mechanisms by which high-energy radiation damages the elastomers are not completely understood itis reasonable to hypothesize a chain breakage of the polymeric chemical bonds caused by the laser ionizing irradiation (i.e. photochemical reactions). The breakage of one chain transfers stress to the neighboring chains, so that chain breakage propagates to the surrounding molecules and the cumulative effect produces micro-fractures. However, these micro-fractures do not extend over large areas due to the viscoelastic dissipation of the stored elastic energy during crack formation. In other words, under high strain conditions, the laser energy results in micro-fractures, but viscoelastic dissipation would maintain the damaged area fairly localized.

Interestingly, a depth–profile curve extracted from an AFM image of the laser-ablated lines obtained at high mechanical strain (ε = 4) presents two main contributions. The first one corresponds to the broad part of the trench profile and can be ascribed to the formation of localized micro-fractures in the elastomeric membrane described above. The second contribute – section located in between red dashed lines in Figure 3.6D – has a much smaller size, and could be related to the pure laser–elastomer inter-action without fracture. Therefore, even if micro-fractures are present, they do not seem to extend over the entire ablated area. In this way, by neglecting the extension of the region featuring micro-cracks, the lines ablated at ε = 4 would present width of W_ε= 0.43 μm, in closer agreement with theoretical predictions.

Finally, by performing laser patterning of pre-stretched elastomers, we successfully achieved fabrication of sub-micrometric features at pulse energies greater than the ablation threshold. Our line patterns presented a reduced line-pitch and line-width compared to the traditional non-stretched ones, with a reduction in size that directly depended on the applied strain.

Sample preparation: Acetoxy polysiloxane (acetoxy-PDMS, Elastosil E43) was purchased from Wacker Chemie AG and used as structural material for the realization of the elastomeric stamp. Reagent grade heptane was purchased from Sigma-Aldrich and used as solvent for the acetoxy-PDMS. The use of heptane was necessary to reduce the viscosity of the acetoxy-PDMS (≈ 3×10^5 cP), so that it can be easily molded without high-pressure-based injection systems. The procedure for the realization acetoxy-PDMS membranes with a thickness of 1 mm thick was as follows. Pure acetoxy-PDMS (30 mg in weight) was dissolved in heptane (≈20 mL in volume) and then mixed vigorously. The resultant mixture was degassed in a low vacuum desiccator for about 5 min, and poured into square-shaped (120 mm) polystyrene petri dish, where it was left to cure overnight under ambient conditions. Two-component PDMS Sylgard 184 was purchased from Dow Corning and used for benchmarking the mechanical properties of the acetoxy-PDMS (e.g. elongation at break). PDMS Sylgard 184 membranes, with a thickness of 1 mm, were prepared by thoroughly mixing the curing agent and the PDMS prepolymer in a 1:10 weight ratio. The mixture was degassed in low vacuum desiccator for 1 hour to remove any air bubbles, and cured at 60°C for 1 h.

Mechanical characterization: The mechanical properties (e.g. elongation at break) of both the acetoxy-PDMS and PDMS Sylgard 184 elastomers were evaluated by uniaxial tensile tests performed on dog bone-shaped samples (4 mm width, 1 mm thickness, 25 mm length) with an Instron 3365 dual column-testing machine. The sample-stretching rate was 100 mm/min. The elastic modulus, ultimate tensile strength, and elongation at break were extracted from the experimental stress−strain curves. Residual mechanical

strain, after releasing the stress applied to the elastomer, was studied from cyclic tensile tests on samples (5 mm width, 1 mm thickness, 10 mm starting length) with a custom designed Deben miniaturized dual-screw uniaxial tensile stage with a strain cycling rate of 5 mm min^{-1} and a strain value from 0 to 1.

Sample preparation for laser-ablation: Laser ablation experiments were performed on membranes of acetoxy-PDMS with rectangular shape (40 mm × 20 mm, 1 mm thickness). Before irradiation, samples were cleaned with ethanol and distilled water in an ultrasonic bath and dried under a nitrogen flux. No other special treatment was performed during the membrane preparation. Mechanical strain was applied to the elastomeric membrane by means of a custom-made uniaxial stretching device (Figure 3.8) which was integrated into the XYZ translation system of our laser setup. The stretching device consisted of two motorized single-axis translation stages (PT1/M-Z8, Thorlabs, Inc.), which were mounted on top of a 50-cm-long aluminum rail (Thorlabs, Inc.) by means of two double dovetail clamps (XT34C1, Thorlabs, Inc.). The elastomeric membrane was clamped between the two motorized single-axis stages by means of two sliding brackets. The two stages can be moved in opposite directions along the aluminum rail, leading to a change in the membrane length, and hence, to a mechanical strain applied to it.

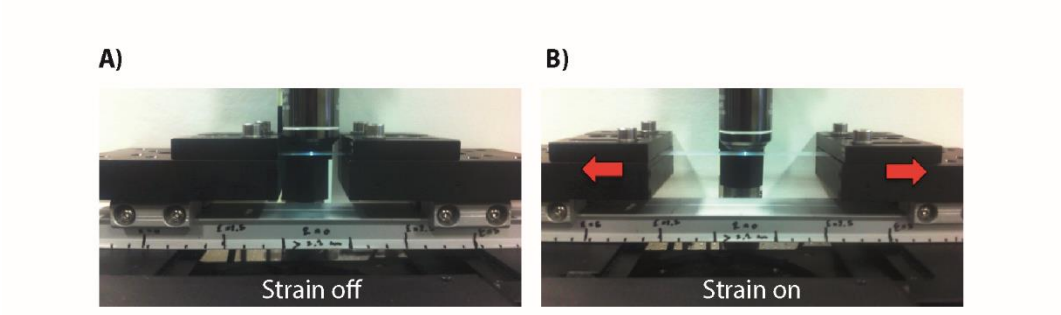

Figure 3.8 Custom made device for uniaxial stretching. The elastomeric membrane was clamped between two motorized single-axis stages moving along a rail in order to obtain (A) strain 'off' and (B) strain 'on' conditions.

To finely tune the strain, the relative position between the two stages was adjusted by means of a controller unit (TDC001 T-Cube Motor Controller, Thorlabs, Inc.) providing a computerized control of each single motor axis.

Optical characterization: Optical images of the ablated samples were acquired by means of a commercial confocal microscope (Fluoview 1000, Olympus) equipped with a water immersion objective lens (Olympus WLSC, 40X, NA 0.9). Geometrical properties of the laser-ablated patterns, i.e. the width and the pitch of parallel lines, were automatically obtained by numerical post-processing of the intensity profile curves extracted from the confocal images. More in details, the distance between two consecutive lines, defined as the pitch P_ε, was determined from the spacing of two consecutive intensity peaks in the intensity profile curve, while the width W_ε of the ablated lines was obtained by measuring the full width at half maximum (FWHM) of each intensity peak in the intensity profile curve.

AFM characterization: Atomic Force Microscopy (AFM) images (amplitude data) were acquired in tapping mode using a Nanowizard II (JPK Instruments, Inc.) mounted on an Axio Observer D1 (Carl Zeiss) inverted optical microscope. V-shaped gold-coated silicon nitride cantilevers (NPS, Veeco Instruments), with a nominal spring constant of 40 N/m and pyramidal tip with typical curvature radius of 10 nm were used. The width of the laser-ablated lines was obtained by measuring the line-depth in cross-section.

3.4 Laser fabrication of thermo-shrinkable polymers

Stimuli-responsive materials, namely materials that can change their properties in response to external stimuli, are the perfect candidates for our strategy to decouple feature size from light-matter interactions. Among the myriad of stimuli responsive materials, shape memory polymers (SMPs) are

particularly appealing due to their high yield of change, wide availability and ease of production [101–103]. Based on the imprint of an initial shape, which is typically 'memorized' into the polymer at an initial fabrication stage, SMPs are stimuli-responsive materials that result in mechanical action when triggered by an external stimulus [95]. In this section, we use SMPs, and in particular heat-shrinkable polymers, to reduce the minimum feature size of laser ablated structures beyond the limits imposed by light-matter interactions. Notably, the thermal and shrinking mechanisms of these polymers have been extensively investigated [104], and they represent a commercially available product widely used for instance in packaging and heat-shrinking tubing applications. In addition, their attractive mechanical, processing, and optical properties render them ideal for applications in fluidics and sensing [105,106].

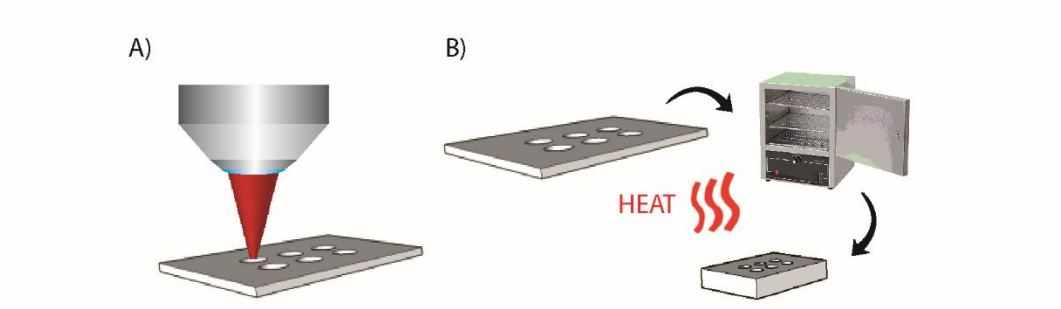

Figure 3.9 Schematic diagram of laser-patterning of thermo-shrinkable polymers. (A) The desired structure was obtained by means laser irradiation. (B) Application of heat caused shrinkage of the pattern, therefore allowing to obtain a reduced minimum feature size.

A schematic representation of our laser-based fabrication of thermo-shrinkable polymers is illustrated in Figure 3.9. Initially, laser-ablation is performed over a thin polyolefin membrane in order to obtain the desired 2D or 3D pattern. Polyolefins (PO) are commercially available thermo-shrinkable polymers which are widely used as shrink wrap films [107]. Due to their

excellent elastic memory, POs can shrink up to 95% depending on the resin selection, blend proportion, and operating conditions [108]. Secondly, the fabricated structure is heated in order to achieve shrinking of the polymeric substrate and, in turn, of the fabricated structure. Thus, with a simple two-step process we are able to obtain a diminished minimum feature size, therefore overcoming the spatial limitations imposed by LDW systems.

In the following subsections, we report results from the fabrication of 2D and 3D patterns. We start by investigating the behavior of the heat-shrinkable polymers when patterning two-dimensional arrays of dots, and continue our study by fabricating 3D through-hole microchannels. We demonstrate miniaturization of the fabricated structures, achieving a shrinking factor of about 3. Importantly, as shrinking in the lateral dimension of the structures corresponds to an increase in the thickness of the polymer, we are able to obtain final patterns with high aspect ratios which would be hardly achievable with other fabrication techniques.

3.4.1 2D patterning of thermo-shrinkable polymers

In order to fully investigate the possibilities offered by the PO substrate with respect to the uniformity and reproducibility of the shrinking as well as to the achievable shrinking factor, we started by fabricating 2D arrays of dots at the polymer surface. For this particular experiment, we used a 10X objective (NA 0.3), resulting in a diffraction limited spot of about 1.3 μm (λ = 800nm). At first, we performed a systematic study of the change in size of the ablated spots as a function of the laser ablation parameters. As a typical example of the fabricated patterns, Figure 3.10A shows a 3 by 3 array obtained by performing single pulse laser ablation at the polymer surface with a pulse energy of 80 μJ. After laser irradiation, we induced shrinking of the ablated pattern via heat application. The resulting structure is shown in Figure 3.10B. Size of the ablated dots was reduced from 22 ± 3 μm to 10 ± 2

μm. Results from the systematic study of the polymer response are presented in Figure 3.10C, which shows the diameter of the ablated dots as a function of the laser pulse energy before and after the shrinking process, respectively. Notably, for energies lower than 0.4 μJ no ablation was observed, thus indicating the ablation threshold for the PO substrate at the aforementioned conditions.

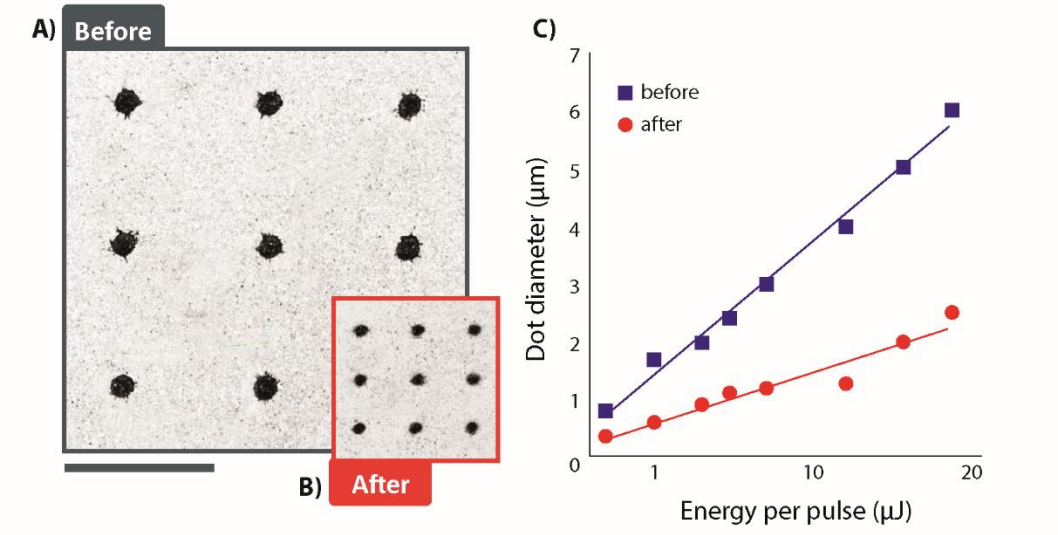

Figure 3.10 2D patterning of heat-shrinkable polymers**.** (A) A 3 by 3 array of dots fabricated by laser ablation onto the membrane surface (E_{pulse}=80 μJ, single pulse). (B) Shrinkage of the array presented in (A) resulted in miniaturization of the pattern while preserving the initial shape. Scale bar 100μm. (C) Size of the ablated dots versus laser energy pulse before (blue) and after (red) shrinking.

Close to the ablation threshold, the minimum feature size can also be evaluated, corresponding in this case to about 1.0 μm. Importantly, linear fitting of the experimental data (before and after shrinking) allows for an estimation of the shrinking factor given by the ratio of the two fitted curve slopes (blue and red lines in Figure 3.10C). In agreement with the result obtained for the initial dots array, we obtained an average shrinking factor of about 2.7. Heating of the PO substrate at higher temperatures with

respect to the one used for this experiment resulted in an increased shrinking factor. However, uniformity of the fabricated structures was not preserved. As in the case of pre-stretched elastomers, we can relate the enhancement in the lateral dimension of the ablated structure to the initial size according to the following equation:

$$S_{final} = S_0(1 - s) \tag{3.3}$$

where S_0 and S_{final} are the initial and final size of the structure, respectively, and s is the lateral shrinking of the polymer in percentage, which in turn depends on the used material and on the shrinking temperature [108]. Finally, we were able to reduce the minimum feature size from 1.0 μm to less than 400 nm, therefore successfully demonstrating the capabilities offered by our approach in order to enhance the performance of current LDW systems.

Sample preparation: A heat-shrinkable polymer consisting of an optically transparent polyolefin (PO) film [108] with a thickness of 25 μm was purchased from Sigma-Aldrich and used as structural material for the realization of our laser-ablated structures. Laser ablation experiments were performed on polyolefin membranes with a circular shape (30 mm radius). Before irradiation, samples were cleaned with distilled water and dried under a nitrogen flux to remove dust or debris from the surface. No other special treatment was performed during the membrane preparation. In order to allow for the correct handling of the thin polymeric film as well as for an optimal planar positioning of the membrane for laser ablation, the membrane was housed into a circular sample holder (Microscopy Attofluor Cell Chamber A7816, Thermo Fisher). Sample cleaning was repeated at the end of the laser processing in order to remove laser processing debris.

Heat-induced shrinking: According to the manufacturer's specifications, shrinking of the polymeric film was achieved by heating the sample inside an oven at a temperature of 115°C for 5 minutes. A temperature ramp of

about 3 minutes (60°C to 115°C) was adopted in order to gradually heat the polymer and achieve a uniform shrinkage of the substrate without deformations. No relevant differences were observed when using a slower heating ramp. To ensure uniform shrinkage, the sample was placed in the oven hung on one side, thus being almost in a freestanding configuration. This solution was used in order to minimize contact of the membrane with other surfaces during shrinking, avoiding crumpling or sticking effects, and allowing for a spontaneous relaxation of the polymeric chains to their original shape.

Optical characterization: Optical images of the ablated samples were acquired by means of a commercial brightfield microscope (Eclipse, Nikon) equipped with a 10X (CFI Plan Apo Lambda, Nikon), a 40X (CFI Plan Apo Lambda, Nikon), and a 100X (CFI Plan Apo Lambda, Nikon) objective lenses. Geometrical properties of the laser-ablated patterns were automatically obtained by numerical post-processing of the intensity profile curves extracted from the optical images.

3.4.2 Fabrication of high aspect-ratio channels

After studying the performance of PO membranes in case of 2D patterning, we extended our investigation to the fabrication of 3D through-holes channels. The ability to fabricate micro and nanochannels is highly desirable for applications such as microfluidics and sensing, and represents at the same time a challenge for current fabrication techniques due to the difficulties in achieving structures with high aspect-ratios [109] [110] [111]. For this experiment, we equipped our LDW system with a 50X objective lens (NA 0.5), while an axicon lens was used to generate a Bessel beam according to Figure 3.2. As shown in Figure 3.11, the resulting Bessel beam had a central focal spot diameter of about 1.0 μm and a focal depth of Z_{max} = 140

μm (FWHM), therefore being well suited for the fabrication of through holes in the PO membranes (thickness 25 μm).

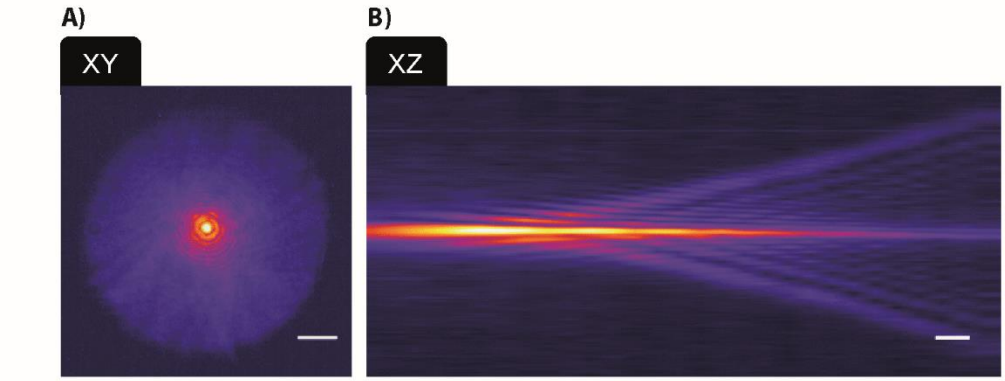

Figure 3.11 Bessel beam characterization (A) XY and (B) XZ profiles of the Bessel beam at the objective lens focal plane.

As for the case of 2D patterning, we performed a systematic study by performing laser ablation with different irradiation parameters. More in detail, we initially investigated the possibility of obtaining through-hole channels by using different pulse energies and pulse numbers. Figure 3.12A shows a map of the fabricated structures by varying the pulse energy between 0.4 and 10 μJ, and the number of pulses from 1 to 100. A representative case of an array of through-holes with a diameter of about 10 μm is shown in Figure 3.12B. In this case, the channels were obtained by using a laser pulse energy of 6 μJ, and a number of pulses equal to 10. As expected, not all the parameter combinations resulted in the generation of through-holes in the polymer (Figure 3.12C), leading to partially opened channels, or simply to deep holes at both polymer surfaces. In agreement with previous studies [112], we observed a ring-like structure surrounding the entrance of the ablated holes, most likely being caused by the low-energy side lobes of the Bessel beam. As the number of laser pulses or the laser energy increased, the annular ring became more evident.

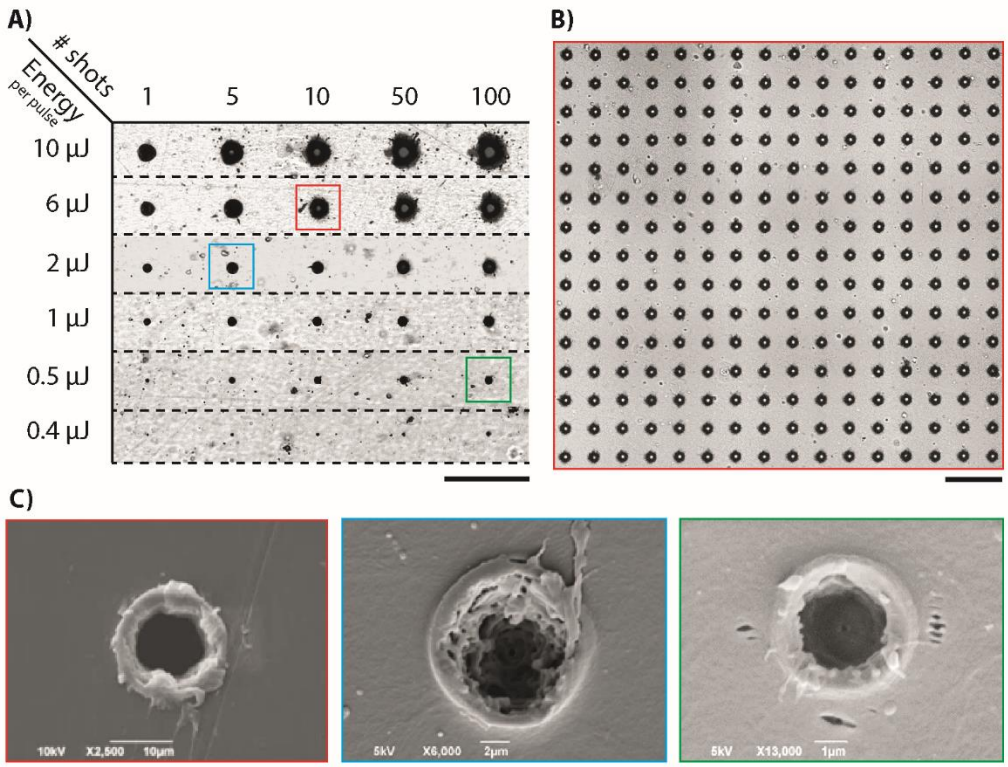

Figure 3.12 Laser fabrication of through-hole channels. (A) Optical images of the laser ablated holes for different laser pulse energy (0.4 to 10 µJ) and pulse number (1 to 100). (B) Optical image of an array of through-hole channels fabricated using an energy per pulse of 6 µJ and a number of pulses equal to 10. (C) SEM images illustrating a magnified view of the channels in (A).

Following our study of the ablation parameters, we then performed shrinking of the fabricated patterns in order to characterize the shrinking performance also in case of 3D structures. As an example, Figure 3.13 illustrates the size (diameter) of the ablated channels as a function of the laser pulse energy before and after the shrinking. In this case the number of laser pulses per each hole was fixed to 100. By performing a linear fit of the experimental data, we could extract the ratio between the slope of the fitted curves before and after shrinking, which lead to a shrink factor of about 2.7, in agreement with the values observed in case of 2D pattering.

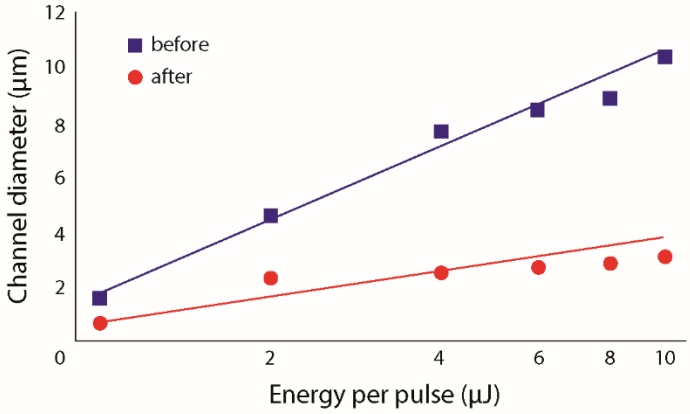

Figure 3.13 Laser fabrication of through-hole channels – calibration curve. The size (diameter) of the ablated channels is plotted as a function of the used laser pulse energy. The number of energy pulses was fixed to 100.

Notably, also in this case we successfully reduced the minimum feature size of the fabricated channels going from an initial minimum feature size (before shrinking) of about 1.0 µm to a final one (after shrinking) of about 400 nm.

Finally, figure 3.14A and 3.14B show a top-view image of the fabricated channels before and after the shrinking respectively. These particular channels were fabricated by using an energy per pulse of 6 µJ and a number of pulses equal to 10 (as for the channels array presented in Figure 3.12B). Lateral dimensions of the ablated channels were successfully reduced from about 10 µm to 3.7 µm. As previously mentioned, the heat-induced shrinkage of the polymers also results in a reduction of lateral dimensions together with an increase in thickness. Figure 3.14C, and 3.14D show the corresponding side-view of the fabricated channels. Remarkably, the height of the channels increased from 25 µm to almost 170 µm. Therefore, the current approach led to an increase in aspect ratio of a factor of ~20 over Bessel-beam fabricated channels.

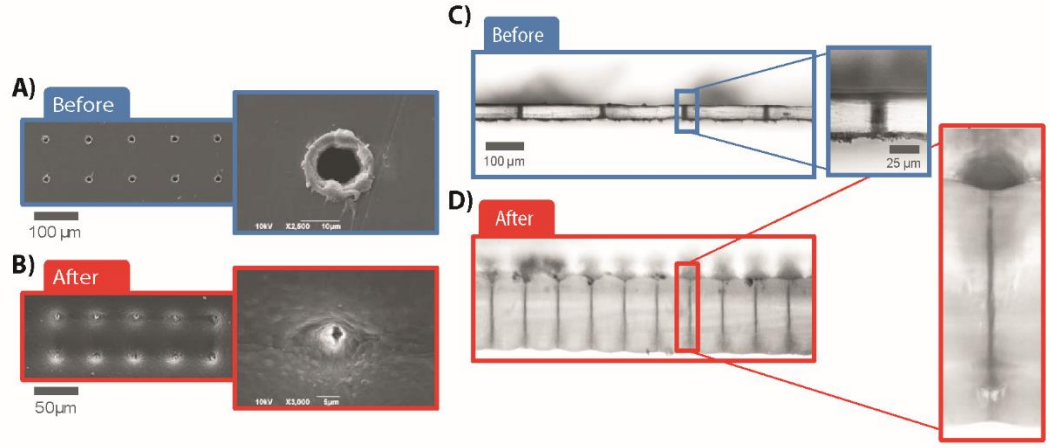

Figure 3.14 Laser fabrication of through-hole channels – top and side view. (A) SEM images of through hole channels fabricated using an energy per pulse of 6 µJ and a number of laser pulses equal to 10. (B) SEM image of the pattern from (A) after the shrinking process. (C) Optical image illustrating a side-view of the channels before shrinking. (D) Optical image illustrating a side-view of the channels after shrinking. Insets represent magnified images of the channels.

These results show the potential of engineered materials to overcome the constraints of LDW techniques. Indeed, Bessel-beams are currently used thanks to their needle-like intensity distribution that enables the fabrication of high aspect ratio structures. By using engineered materials, such aspect ratio can be increased by more than an order of magnitude, obtaining an unprecedented control on the laser-fabricated structures.

3.5 Engineering the design of shrinkable materials

The use of stimuli-responsive materials in order to overcome current limitations of LDW systems allows for the creation of devices with uncommon or non-trivial geometries. Within section 3.4.3, we showed how

the shrinking properties of thermo-shrinkable polymers can be leveraged in order to fabricate 3D structures with ultra-high aspect ratios, successfully achieving fabrication of through-holes microchannels. Notably, as new engineered materials are being developed, additional structures expressing innovative or non-conventional shapes could potentially be fabricated, therefore increasing the capabilities offered by our technique [113]. Nonetheless, fabrication of devices with new articulated or complex shapes often requires thoughtful design in order to fully understand and exploit the material reconfiguration capabilities [104]. Can any desired pattern be fabricated by means of laser ablation and then uniformly shrank while preserving its shape? To this end, we performed simulations of the polymers shrinking process with the aim of potentially predicting the behavior of shrinkable materials, as well as of developing a tool to properly pre-design the desired structures prior to laser irradiation. The model presented herein represents a preliminary work and results from the simulations should be used, at this stage, as a qualitative tool for predicting the reconfiguration capabilities of shape-memory polymers.

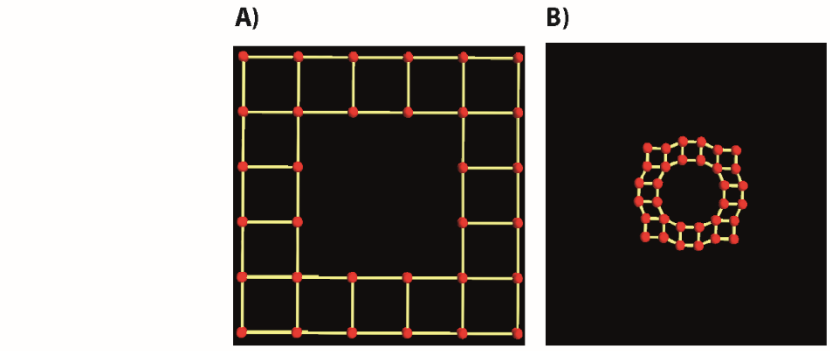

Figure 3.15 Simulation of the shrinking dynamics of a 2D lattice consisting of a 6 by 6 array of masses (red) mutually interconnected by springs (yellow). (A) Image of the lattice before shrinking and (B) after shrinking.

Among the various discrete simulations which have already been developed to mimic the behavior of polymeric chains, the so-called bead-spring chain model represents the simplest simulation of polymeric chains capable of capturing the essential physical principles and dynamics of polymers (e.g. extension and shrinkage of the polymeric chains) [114]. Accordingly, polymeric chains can be approximated as a series of masses mutually interconnected by springs. A desired morphological distribution of polymeric chains can, therefore, be obtained by building an equivalent system composed of masses and springs.

As an example, Figure 3.15A shows a simulated 2D lattice where the mass-spring model was used to model a thin polymeric membrane with a single central hole, potentially resembling a through-hole channel obtained by laser ablation. In this case, each mass was positioned in space according to the desired morphology, and connected to the neighboring masses in order to resemble the connections between the polymer chains. Importantly, starting from this configuration, mechanical stress acting on the polymer can be simulated by simply setting the initial extension of the springs. According to Hooke's law, the force generated by a spring can be written as $F = kx$, where k is the spring constant, and x represents the displacement or change in length of the spring with respect to its initial length. As a consequence, compression or tension of the springs composing the polymeric chains can be simulated by choosing the proper initial value of x. In our case, we simulated shrinkable polymers by setting the springs to an initial elongated state. Notably, this configuration can be compared both to the case of a pre stretched elastomer, as well as to a heat shrinkable polymer. For this particular simulation, we decided to set the initial length of the springs to be 2 times their initial length. After simulating shrinking dynamics, our model correctly predicted the size reduction of the lattice, as shown in Figure 3.15B. Following this first simulation, we then investigated the capability of our model to predict the shrinking behaviour of polymeric substrates after laser ablation of more complex patterns. To this end, we

designed a 2D lattice resembling a polymeric substrate with a pattern of holes (Figure 3.16A).

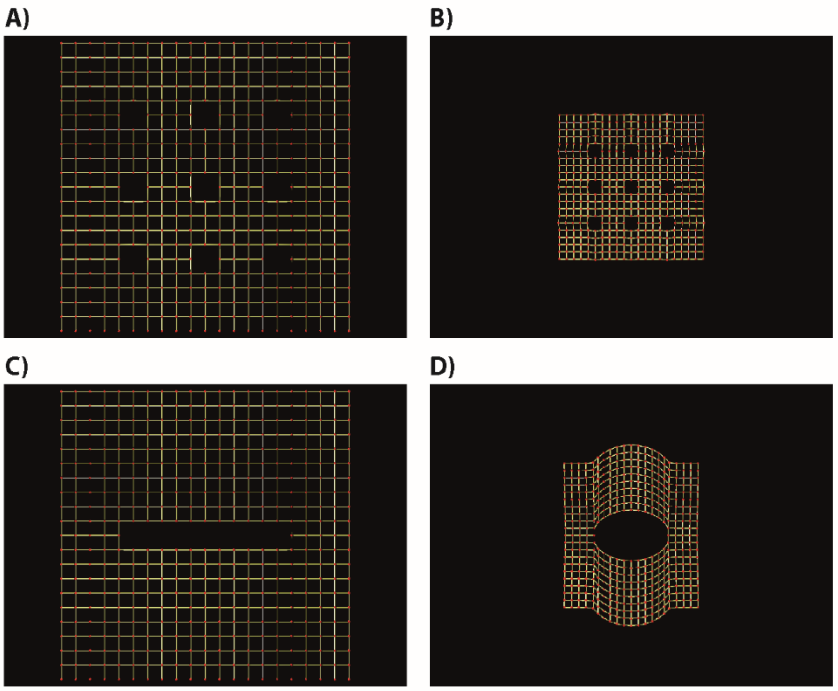

Figure 3.16 Simulation of the shrinking dynamics of a 2D lattice consisting of a 21 by 21 array of masses (red) mutually interconnected by springs (yellow). (A) and (C) illustrate two different lattice structures resembling a substrate with an array of holes, and a cut-like pattern, respectively. (B) and (D) represent images of the 2D lattices after simulation of the shrinking process. Notably, while the pattern in (A) correctly reduces its size resulting in a uniform shrinking, the asymmetrical pattern in (B) fails to achieve a uniform shrink.

As in the previous case, we hypothesized an initial elongation of the springs of a factor of 2, and then simulated the shrinking process. Figure 3.16B shows the resulting structure after shrinking. In accordance with experimental results, the fabricated holes, as well as the substrate, uniformly reduced their size, resembling relaxation of the polymer to its original shape.

Finally, as a proof of concept to evaluate the design of more complex structure, we simulated shrinking of a highly non-symmetrical pattern. Figure 3.16C shows a 2D lattice resembling a polymeric membrane affected by an elongated cut. Is this pattern going to affect the uniformity of the shrinking? In this case, simulation of the shrinking process resulted in a non-uniform size reduction of the 2D lattice (Figure 3.16D), therefore indicating a potential constraint for the successful fabrication of this type of patterns. Our model represents only a primitive approximation of the behavior of a polymeric material. However, it offers the possibility to simulate shrinkable substrates with potentially any desired shape or pattern. In conclusion, this could lead to the realization of a useful tool to pre-design structures or devices while taking into account the material reconfiguration properties.

Simulations: Custom software written in Python language was developed in order to perform simulations of the shrinkable polymers. The mass-spring model allowed for the creation of a mesh of m x n virtual masses. Each mass was linked to its neighbors by massless springs and positioned at time t at the location $P_{i,j}(t)$. Evolution of the system was simulated according to the fundamental law of dynamics $F_{ij} = ma_{ij}$, where m is the mass of each point $P_{i,j}(t)$ (equal for all points) and a_{ij} is the acceleration caused by the force F_{ij}. The force $F_{ij}(t)$ applied on a point $P_{i,j}(t)$ at time t was computed as $F_{ij} = \sum(F_{spring}, F_{damp})$, which included the force contributions given by the springs connected to the mass (F_{spring}), and by the viscous damping (F_{damp}). The fundamental dynamics equations were then integrated through time by using Euler method in order to retrieve the position of each mass at any given time:

$$\begin{cases} a_{ij}(t+\Delta t) = \dfrac{1}{m}F_{ij}(t) \\ v_{ij}(t+\Delta t) = v_{ij}(t) + \Delta t a_{ij}(t+\Delta t) \\ P_{ij}(t+\Delta t) = P_{i,j}(t) + \Delta t v_{ij}(t+\Delta t) \end{cases}$$

where $v_{ij}(t)$ is the velocity of point $P_{i,j}(t)$, and Δt is a chosen time-step. A comprehensive description of the used model can be found in [115]. Simulations of the implemented mass-spring model were achieved by ad-hoc customization of a Python library for physics-based general 3D mass-spring systems (Kinetics Kit, kineticskit.net). Finally, images corresponding to the 3D rendering of the simulated mass-spring models were obtained by using a ray tracing software (PovRay, POV-Ray.org).

3.6 Conclusions

The focusing capabilities of an optical system can be significantly enhanced by combining laser processing together with engineered materials which can reconfigure themselves in response to an external stimulus. Fabrication of structures with minimum feature size beyond the diffraction limit can, in fact, be achieved by means of shrinkable materials. As a result, sub-micrometric features can be obtained at pulse energies greater than the ablation threshold, with a reduction in feature size that directly depends on the material shrinkage. In this way, 2D and 3D user-designed patterns can be fabricated with dimensions that are significantly reduced compared to the traditional laser direct-writing approaches. At this stage, laser ablation of engineered materials can be a valid alternative to current multistep, time-consuming and expensive technologies exploited so far in the microfabrication field, opening new possibilities for the rapid design of microstructures suitable for a wide range of relevant applications including soft-lithography, microfluidics, and lab-on-chip. In the future, application of our method to newly developed engineered materials will make it possible to further decrease the minimum feature size, thus converting laser-based fabrication to a true nanopatterning tool.

Conclusions

Optical systems represent a powerful tool to achieve at the same time characterization and modification of materials at the micro and nanoscale. The intrinsic properties offered by light enable imaging a biological sample with minimal perturbation, as well as fabrication of miniaturized 2D and 3D devices with high flexibility. Nonetheless, the trade-off between the spatial and temporal resolution offered by standard optical systems and the technical constraints imposed by the desired application (e.g. imaging of fast biological dynamics or nanoscale laser fabrication) still limits the establishment of optical systems to a wider range of applications.

In this thesis, we explored the development of novel systems for optical-based imaging and fabrication techniques, with the aim of overcoming current limitations in both fields. The following conclusions can be deduced from our work:

Optical systems for imaging:

1. Pixel-based Z-focus control enables for novel versatile approaches to fast 3D imaging. An acoustic optofluidic lens can be easily integrated into a standard laser scanning microscope in order to achieve beam shaping capabilities at the microsecond timescale. Such a lens enables for high-speed axial scanning in both two-photon microscopy and confocal microscopy allowing to perform interchangeably A, B, or C scans without the need for dedicated optical setups. By using different phase profiles to drive the lens, either high- speed axial scanning or controlled aberrations imaging can be achieved.
2. The possibility to achieve axial scanning on a pixel by pixel basis is useful to perform volumetric imaging at high rates (x,y,z,t), or to enable for high-speed cross-sectional imaging (x,z,t).
3. The capability of the acoustic lens to induce controlled aberrations in the excitation pathway can increase the penetration depth of current

2PE microscopes by means of a differential-aberration imaging approach. The lens can, in fact, be used to successfully reject the out-of-focus contribution in a 2PE system in order to remove the scattering component of an image.

4. Pixel-based z focus control can potentially establish as a new paradigm for laser scanning microscopes, leading to the design of novel optical systems capable of achieving unprecedented 3D spatiotemporal resolution.

Optical systems for fabrication:

1. The use of optical systems together with engineered materials enables for the fabrication of structures with a minimum feature size below the limitations imposed by diffraction. This approach allows to successfully decouple the final size of the fabricated structures from light-matter interaction constraints.
2. The size reduction capabilities offered by shape memory polymers such as pre-stretched elastomers and heat-shrinkable polymers combined with femtosecond laser ablation enables for the fabrication of 2D and 3D structures with sub-wavelength dimensions.
3. As the shrinking process results in a reduction in lateral dimensions together with an increase in thickness, realization of structures with aspect ratios not achievable with current laser-based techniques is possible.
4. Laser-based fabrication using engineered materials represents a step forward in the use of laser-based fabrication systems for 2D and 3D fabrication at the nanoscale. As new engineered materials are being developed, this approach could, in fact, pave the way for the use of laser systems as economic, flexible and customizable nanofabrication tools.

References

1. D. B. Murphy and M. W. Davidson, "Fundamentals of Light Microscopy," in *Fundamentals of Light Microscopy and Electronic Imaging* (John Wiley & Sons, Inc., 2012), pp. 1–19.

2. P. P. Mondal and A. Diaspro, "Ray Optics, Wave Optics and Imaging System Design," in *Fundamentals of Fluorescence Microscopy: Exploring Life with Light* (Springer Netherlands, 2014), pp. 3–31.

3. F. A. Jenkins and H. E. White, *Fundamentals of Optics* (Mc-Graw Hill, 2001).

4. M. Born, E. Wolf, and A. B. Bhatia, *Principles of Optics: Electromagnetic Theory of Propagation, Interference and Diffraction of Light* (Cambridge University Press, 1999).

5. J. W. Goodman, *Introduction to Fourier Optics* (Mc-Graw Hill, 1996).

6. Y. B. Band, *Light and Matter: Electromagnetism, Optics, Spectroscopy and Lasers*, Light and Matter (John Wiley & Sons, 2006).

7. M. Mishchenko, L. D. Travis, and A. Lacis, *Scattering, Absorption, and Emission of Light by Small Particles* (2002), Vol. 4.

8. M. S. Brown and C. B. Arnold, "Fundamentals of Laser-Material Interaction and Application to Multiscale Surface Modification," in *Laser Precision Microfabrication*, K. Sugioka, M. Meunier, and A. Piqué, eds. (Springer Berlin Heidelberg, 2010), pp. 91–120.

9. C. W. Schneider and T. Lippert, *Laser Processing of Materials* (2003).

10. M. Castillejo and P. M. Ossi, *Lasers in Materials Science* (2014), Vol. 191.

11. J. Ying, F. Liu, and R. R. Alfano, "Effect of Scattering on Nonlinear Optical Scanning Microscopy Imaging of highly scattering media," Appl. Opt. **39**, 509 (2000).

12. A. K. Dunn, V. P. Wallace, M. Coleno, M. W. Berns, and B. J. Tromberg, "Influence of optical properties on two-photon fluorescence imaging in turbid samples," Appl. Opt. **39**, 1194 (2000).

13. C. M. Blanca and C. Saloma, "Monte Carlo Analysis of Two-Photon Fluorescence Imaging Through a Scattering Medium," Appl. Opt. **37**, 8092 (1998).

14. A. Singh, J. D. McMullen, E. A. Doris, and W. R. Zipfel, "Comparison of objective lenses for multiphoton microscopy in turbid samples," Biomed. Opt. Express **6**, 3113 (2015).

15. P. Theer and W. Denk, "On the fundamental imaging-depth limit in two-photon microscopy," J. Opt. Soc. Am. A **23**, 3139–3149 (2006).

16. a Leray, K. Lillis, and J. Mertz, "Enhanced background rejection in thick

tissue with differential-aberration two-photon microscopy.," Biophys. J. **94**, 1449–1458 (2008).

17. P. T. C. So, C. Y. Dong, B. R. Masters, and K. M. Berland, "Two-photon excitation fluorescence microscopy," Annu. Rev. Biomed. Eng. **2**, 399–429 (2000).

18. S. Quirin, J. Jackson, D. S. Peterka, and R. Yuste, "Simultaneous imaging of neural activity in three dimensions.," Front. Neural Circuits **8**, 29 (2014).

19. R. R. Gattass and E. Mazur, "Femtosecond laser micromachining in transparent materials," Nat. Photonics **2**, 219–225 (2008).

20. F. Chen and J. R. Vázquez de Aldana, "Laser-written 3D crystalline photonic devices," SPIE Newsroom 1–4 (2015).

21. S. Zhang, C. Li, and S. Li, *Understanding Optical Systems Through Theory and Case Studies*, SPIE Press Monographs (SPIE Press, 2017).

22. R. D. Guenther, D. G. Steel, and L. P. Bayvel, *Encyclopedia of Modern Optics*, Encyclopedia of Modern Optics (Elsevier Academic Press, 2005).

23. R. R. Alfano, "Handbook of Biomedical Optics, by David A Boas, Constantinos Pitris, and Nimmi Ramanujam," **16**, 129901 (2011).

24. N. Olivier, A. Mermillod-Blondin, C. B. Arnold, and E. Beaurepaire, "Two-photon microscopy with simultaneous standard and extended depth of field using a tunable acoustic gradient-index lens.," Opt. Lett. **34**, 1684–1686 (2009).

25. L. Kong, J. Tang, J. P. Little, Y. Yu, T. Lämmermann, C. P. Lin, R. N. Germain, and M. Cui, "Continuous volumetric imaging via an optical phase-locked ultrasound lens.," Nat. Methods **12**, 759–762 (2015).

26. M. Duocastella and C. B. Arnold, "Enhanced depth of field laser processing using an ultra-high-speed axial scanner," Appl. Phys. Lett. **102**, (2013).

27. J.-A. Conchello and J. W. Lichtman, "Optical sectioning microscopy," Nat. Methods **2**, 920–931 (2005).

28. C. Sheppard and D. Shotton, *Confocal Laser Scanning Microscopy*, Microscopy Handbooks (BIOS Scientific, 1997).

29. A. Diaspro, *Confocal and Two-Photon Microscopy: Foundations, Applications and Advances* (Wiley, 2002).

30. T. V Truong, W. Supatto, D. S. Koos, J. M. Choi, and S. E. Fraser, "Deep and fast live imaging with two-photon scanned light-sheet microscopy.," Nat. Methods **8**, 757–60 (2011).

31. M. Duocastella and C. B. Arnold, "Bessel and annular beams for materials processing," Laser Photon. Rev. **6**, 607–621 (2012).

32. F. Courvoisier, J. Zhang, M. K. Bhuyan, M. Jacquot, and J. M. Dudley, "Applications of femtosecond Bessel beams to laser ablation," Appl. Phys. A

Mater. Sci. Process. **112**, 29–34 (2013).

33. M. Mazilu, D. J. Stevenson, F. Gunn-Moore, and K. Dholakia, "Light beats the spread: “non-diffracting” beams," Laser Photon. Rev. **4**, 529–547 (2009).

34. D. McGloin and K. Dholakia, "Bessel beams: Diffraction in a new light," Contemp. Phys. **46**, 15–28 (2005).

35. M. Duocastella, B. Sun, and C. B. Arnold, "Simultaneous imaging of multiple focal planes for three-dimensional microscopy using ultra-high-speed adaptive optics.," J. Biomed. Opt. **17**, 50505 (2012).

36. A. Mermillod-blondin, E. Mcleod, and C. B. Arnold, "High-speed varifocal imaging with a tunable acoustic gradient index of refraction lens," Opt. Lett. **33**, 2146–2148 (2008).

37. Y. Nakai, M. Ozeki, T. Hiraiwa, R. Tanimoto, A. Funahashi, N. Hiroi, A. Taniguchi, S. Nonaka, V. Boilot, R. Shrestha, J. Clark, N. Tamura, V. M. Draviam, and H. Oku, "High-speed microscopy with an electrically tunable lens to image the dynamics of *in vivo* molecular complexes," Rev. Sci. Instrum. **86**, 13707 (2015).

38. M. Blum, M. Büeler, C. Grätzel, and M. Aschwanden, "Compact optical design solutions using focus tunable lenses," in (International Society for Optics and Photonics, 2011), Vol. 8167, p. 81670W.

39. M. Duocastella and C. B. Arnold, "Transient response in ultra-high speed liquid lenses," J. Phys. D. Appl. Phys. **46**, 75102 (2013).

40. N. Ji, J. Freeman, and S. L. Smith, "Technologies for imaging neural activity in large volumes," Nat. Neurosci. **19**, 1154–64 (2016).

41. A. Cheng, J. T. Gonçalves, P. Golshani, K. Arisaka, and C. Portera-Cailliau, "Simultaneous two-photon calcium imaging at different depths with spatiotemporal multiplexing," Nat. Methods **8**, 139–142 (2011).

42. G. Katona, G. Szalay, P. Maák, A. Kaszás, M. Veress, D. Hillier, B. Chiovini, E. S. Vizi, B. Roska, and B. Rózsa, "Fast two-photon in vivo imaging with three-dimensional random-access scanning in large tissue volumes," Nat. Methods **9**, 201–208 (2012).

43. G. Y. Fan, H. Fujisaki, A. Miyawaki, R. K. Tsay, R. Y. Tsien, and M. H. Ellisman, "Video-rate scanning two-photon excitation fluorescence microscopy and ratio imaging with cameleons.," Biophys. J. **76**, 2412–20 (1999).

44. E. Y. S. Yew, C. J. R. Sheppard, and P. T. C. So, "Temporally focused wide-field two-photon microscopy: paraxial to vectorial.," Opt. Express **21**, 12951–63 (2013).

45. E. E. Hoover and J. A. Squier, "Advances in multiphoton microscopy technology," Nat. Photonics **7**, 93–101 (2013).

46. R. Salomé, Y. Kremer, S. Dieudonné, J.-F. Léger, O. Krichevsky, C. Wyart, D. Chatenay, and L. Bourdieu, "Ultrafast random-access scanning in two-

photon microscopy using acousto-optic deflectors.," J. Neurosci. Methods **154**, 161–74 (2006).

47. A. Bullen, S. S. Patel, and P. Saggau, "High-speed, random-access fluorescence microscopy: I. High-resolution optical recording with voltage-sensitive dyes and ion indicators.," Biophys. J. **73**, 477–91 (1997).

48. A. Cheng, J. T. Gonçalves, P. Golshani, K. Arisaka, and C. Portera-Cailliau, "Simultaneous two-photon calcium imaging at different depths with spatiotemporal multiplexing," Nat. Methods **8**, 139–142 (2011).

49. X. Mao, S.-C. S. Lin, M. I. Lapsley, J. Shi, B. K. Juluri, and T. J. Huang, "Tunable Liquid Gradient Refractive Index (L-GRIN) lens with two degrees of freedom.," Lab Chip **9**, 2050–8 (2009).

50. N.-T. Nguyen, "Micro-optofluidic Lenses: A review," Biomicrofluidics **4**, 31501 (2010).

51. M. Duocastella, G. Vicidomini, and A. Diaspro, "Simultaneous multiplane confocal microscopy using acoustic tunable lenses," Opt. Express **22**, 19293–19301 (2014).

52. S. Piazza, P. Bianchini, C. Sheppard, A. Diaspro, and M. Duocastella, "Enhanced volumetric imaging in 2-photon microscopy via acoustic lens beam shaping," J. Biophotonics 1–11 (2017).

53. E. McLeod and C. B. Arnold, "Mechanics and refractive power optimization of tunable acoustic gradient lenses," J. Appl. Phys. **102**, 33104 (2007).

54. A. Leray and J. Mertz, "Rejection of two-photon fluorescence background in thick tissue by differential aberration imaging.," Opt. Express **14**, 10565–10573 (2006).

55. M. Duocastella and C. B. Arnold, "Transient response in ultra-high speed liquid lenses," J. Phys. D. Appl. Phys. **46**, 75102 (2013).

56. M. Born, E. Wolf, and A. B. Bhatia, *Principles of Optics: Electromagnetic Theory of Propagation, Interference and Diffraction of Light* (Cambridge University Press, 1999).

57. Q. Q. Zhang, X. J. Wu, C. Wang, S. W. Zhu, Y. L. Wang, B. Z. Gao, and X.-C. Yuan, "Scattering Coefficients of Mice Organs Categorized Pathologically by Spectral Domain Optical Coherence Tomography," Biomed Res. Int. **2014**, 1–5 (2014).

58. H. Navarro, A. Dorado, G. Saavedra, and M. M. Corral, "Three-Dimensional Imaging and Display through Integral Photography," J. Inf. Commun. Converg. Eng. **12**, 89–96 (2014).

59. M. E. Brezinski, *Optical Coherence Tomography: Principles and Applications* (Academic Press, Inc., 2005).

60. W. Denk, J. H. Strickler, and W. W. Webb, "Two-photon laser scanning fluorescence microscopy.," Science **248**, 73–76 (1990).

61. D. W. Piston, "Imaging living cells and tissues by two-photon excitation microscopy.," Trends Cell Biol. **9**, 66–69 (1999).

62. P. Theer, M. T. Hasan, and W. Denk, "Two-photon imaging to a depth of 1000 microm in living brains by use of a Ti:Al2O3 regenerative amplifier.," Opt. Lett. **28**, 1022–4 (2003).

63. I. Escobar, G. Saavedra, M. Martínez-Corral, and J. Lancis, "Reduction of the spherical aberration effect in high-numerical-aperture optical scanning instruments," J. Opt. Soc. Am. A **23**, 3150 (2006).

64. N. G. Horton, K. Wang, C. C. Wang, and C. Xu, "In vivo three-photon imaging of subcortical structures of an intact mouse brain using quantum dots," 2013 Conf. Lasers Electro-Optics Eur. Int. Quantum Electron. Conf. CLEO/Europe-IQEC 2013 **7**, 205–209 (2013).

65. J. Schindelin, I. Arganda-Carreras, E. Frise, V. Kaynig, M. Longair, T. Pietzsch, S. Preibisch, C. Rueden, S. Saalfeld, B. Schmid, J.-Y. Tinevez, D. J. White, V. Hartenstein, K. Eliceiri, P. Tomancak, and A. Cardona, "Fiji - an Open Source platform for biological image analysis," Nat. Methods **9**, 10.1038/nmeth.2019 (2012).

66. G. Marriott, S. Mao, T. Sakata, J. Ran, D. K. Jackson, C. Petchprayoon, T. J. Gomez, E. Warp, O. Tulyathan, H. L. Aaron, E. Y. Isacoff, and Y. Yan, "Optical lock-in detection imaging microscopy for contrast-enhanced imaging in living cells," Proc. Natl. Acad. Sci. **105**, 17789–17794 (2008).

67. M. Duocastella, F. Tantussi, A. Haddadpour, R. P. Zaccaria, A. Jacassi, G. Veronis, A. Diaspro, and F. De Angelis, "Combination of scanning probe technology with photonic nanojets," Sci. Rep. **7**, 3474 (2017).

68. W. J. Shain, N. A. Vickers, B. B. Goldberg, T. Bifano, and J. Mertz, "Extended Depth-of-Field Microscopy with a High-Speed Deformable Mirror," **10073**, 1–7 (2017).

69. R. T. Borlinghaus, "High Speed Scanning Has the Potential to Increase Fluorescence Yield and to Reduce Photobleaching," Microsc. Res. Tech. **69**, 689–692 (2006).

70. G. Donnert, C. Eggeling, and S. W. Hell, "Triplet-relaxation microscopy with bunched pulsed excitation.," Photochem. Photobiol. Sci. **8**, 481–485 (2009).

71. M. G. Macey, *Flow Cytometry: Principles and Applications*, SpringerLink: Springer E-Books (Humana Press, 2007).

72. H. M. Shapiro, *Practical Flow Cytometry* (Wiley, 2005).

73. A. Adan, G. Alizada, Y. Kiraz, Y. Baran, and A. Nalbant, "Flow cytometry: basic principles and applications," Crit. Rev. Biotechnol. **37**, 163–176 (2017).

74. D. A. Basiji, W. E. Ortyn, L. Liang, V. Venkatachalam, and P. Morrissey, "Cellular Image Analysis and Imaging by Flow Cytometry," Clin. Lab. Med. **27**, 653–670 (2007).

75. N. S. Barteneva, E. Fasler-Kan, and I. A. Vorobjev, "Imaging Flow Cytometry,"

J. Histochem. Cytochem. **60**, 723–733 (2012).

76. Y. Han, Y. Gu, A. Ce Zhang, and Y.-H. Lo, "Imaging Technologies for Flow Cytometry," Lab Chip **36**, 1011–1014 (2016).

77. T. C. George, D. A. Basiji, B. E. Hall, D. H. Lynch, W. E. Ortyn, D. J. Perry, M. J. Seo, C. A. Zimmerman, and P. J. Morrissey, "Distinguishing modes of cell death using the ImageStream® multispectral imaging flow cytometer," Cytom. Part A **59A**, 237–245 (2004).

78. E. Schonbrun, S. S. Gorthi, and D. Schaak, "Microfabricated multiple field of view imaging flow cytometry," Lab Chip **12**, 268–273 (2012).

79. S. S. Gorthi, D. Schaak, and E. Schonbrun, "Fluorescence imaging of flowing cells using a temporally coded excitation," Opt. Express **21**, 5164–5170 (2013).

80. K. Goda, K. K. Tsia, and B. Jalali, "Serial time-encoded amplified imaging for real-time observation of fast dynamic phenomena," Nature **458**, 1145 (2009).

81. L. Kong, J. Tang, and M. Cui, "Multicolor multiphoton in vivo imaging flow cytometry," Opt. Express **24**, 6126–6135 (2016).

82. J. Wu, J. Li, and R. K. Y. Chan, "A light sheet based high throughput 3D-imaging flow cytometer for phytoplankton analysis," Opt. Express **21**, 14474 (2013).

83. R. W. Keyes, "The Future of Solid-State Electronics," Phys. Today **45**, 42–48 (1992).

84. Y. Xia and G. M. Whitesides, "Soft Lithography," Angew. Chemie Int. Ed. **37**, 550–575 (1998).

85. A. Bertsch, H. Lorenz, and P. Renaud, "3D microfabrication by combining microstereolithography and thick resist UV lithography," Sensors Actuators A Phys. **73**, 14–23 (1999).

86. P. Serra, "Laser-induced forward Transfer: a Direct-writing Technique for Biosensors Preparation," J. Laser Micro/Nanoengineering **1**, 236–242 (2006).

87. A. Piqué, R. C. Y. Auyeung, H. Kim, N. A. Charipar, and S. A. Mathews, "Laser 3D micro-manufacturing," J. Phys. D. Appl. Phys. **49**, 223001 (2016).

88. Y. Qin, A. Brockett, Y. Ma, A. Razali, J. Zhao, C. Harrison, W. Pan, X. Dai, and D. Loziak, "Micro-manufacturing: Research, technology outcomes and development issues," Int. J. Adv. Manuf. Technol. **47**, 821–837 (2010).

89. J.-Y. Cheng, "High-Quality Surface Micromachining on Polymer Using Visible-LIBWE," J. Laser Micro/Nanoengineering **11**, 117–123 (2016).

90. S. Maruo, O. Nakamura, and S. Kawata, "Three-dimensional microfabrication with two-photon-absorbed photopolymerization," Opt. Lett. **22**, 132 (1997).

91. C. Florian, S. Piazza, A. Diaspro, P. Serra, and M. Duocastella, "Direct Laser Printing of Tailored Polymeric Microlenses," ACS Appl. Mater. Interfaces **8**,

17028–17032 (2016).

92. C. B. Arnold, P. Serra, and A. Piqué, "Laser Direct-Write Techniques for Printing of Complex Materials," MRS Bull. **32**, 23–32 (2007).

93. F. Korte, J. Serbin, J. Koch, A. Egbert, C. Fallnich, A. Ostendorf, and B. N. Chichkov, "Towards nanostructuring with femtosecond laser pulses," Appl. Phys. A **77**, 229–235 (n.d.).

94. S. Surdo, S. Piazza, L. Ceseracciu, A. Diaspro, and M. Duocastella, "Towards nanopatterning by femtosecond laser ablation of pre-stretched elastomers," Appl. Surf. Sci. **374**, 151–156 (2016).

95. S. Lin, E. K. Lee, and M. Khine, "Thermally-induced miniaturization for micro- and nanofabrication: progress and updates," Lab Chip **14**, 3475–3488 (2014).

96. M. Beresna, M. Gecevičius, and P. G. Kazansky, "Ultrafast laser direct writing and nanostructuring in transparent materials," Adv. Opt. Photon. **6**, 293–339 (2014).

97. J. Durnin, J. J. Miceli, and J. H. Eberly, "Diffraction-free beams," Phys. Rev. Lett. **58**, 1499–1501 (1987).

98. J. E. Mark, *Polymer Data Handbook* (1999).

99. A. Mata, A. J. Fleischman, and S. Roy, "Characterization of Polydimethylsiloxane (PDMS) Properties for Biomedical Micro/Nanosystems," Biomed. Microdevices **7**, 281–293 (2005).

100. L. Ceseracciu, J. A. Heredia-Guerrero, S. Dante, A. Athanassiou, and I. S. Bayer, "Robust and Biodegradable Elastomers Based on Corn Starch and Polydimethylsiloxane (PDMS)," ACS Appl. Mater. Interfaces **7**, 3742–3753 (2015).

101. M. Behl and A. Lendlein, "Shape-memory polymers," Mater. Today **10**, 20–28 (2007).

102. Q. Zhao, H. J. Qi, and T. Xie, "Recent progress in shape memory polymer: New behavior, enabling materials, and mechanistic understanding," Prog. Polym. Sci. **49**–**50**, 79–120 (2015).

103. M. D. Hager, S. Bode, C. Weber, and U. S. Schubert, "Shape memory polymers: Past, present and future developments," Prog. Polym. Sci. **49**–**50**, 3–33 (2015).

104. J. Morshedian, H. A. Khonakdar, and S. Rasouli, "Modeling of Shape Memory Induction and Recovery in Heat-Shrinkable Polymers," Macromol. Theory Simulations **14**, 428–434 (2005).

105. W. Small, IV, P. Singhal, T. S. Wilson, and D. J. Maitland, "Biomedical applications of thermally activated shape memory polymers," J. Mater. Chem. **20**, 3356 (2010).

106. C. C. Fu, A. Grimes, M. Long, C. G. L. Ferri, B. D. Rich, S. Ghosh, S. Ghosh,

L. P. Lee, A. Gopinathan, and M. Khine, "Tunable nanowrinkles on shape memory polymer sheets," Adv. Mater. **21**, 4472–4476 (2009).

107. A. Durmus, M. B. Alanalp, and I. Aydin, "Investigation of morphological, rheological, and mechanical properties of cyclic olefin copolymer/poly(ethylene- *co* -vinyl acetate) blend films," J. Plast. Film Sheeting 875608791770933 (2017).

108. D. Nguyen, D. Taylor, K. Qian, N. Norouzi, J. Rasmussen, S. Botzet, M. Lehmann, K. Halverson, and M. Khine, "Better shrinkage than Shrinky-Dinks," Lab Chip **10**, 1623 (2010).

109. M. K. Bhuyan, F. Courvoisier, P. A. Lacourt, M. Jacquot, R. Salut, L. Furfaro, and J. M. Dudley, "High aspect ratio nanochannel machining using single shot femtosecond Bessel beams," Appl. Phys. Lett. **97**, 95–98 (2010).

110. Y. Bellouard, A. Said, M. Dugan, and P. Bado, "Fabrication of high-aspect-ratio, micro-fluidic channels and tunnels using femtosecond laser pulses and chemical etching," Opt. Express **12**, 2120 (2004).

111. R. Suriano, A. Kuznetsov, S. M. Eaton, R. Kiyan, G. Cerullo, R. Osellame, B. N. Chichkov, M. Levi, and S. Turri, "Femtosecond laser ablation of polymeric substrates for the fabrication of microfluidic channels," Appl. Surf. Sci. **257**, 6243–6250 (2011).

112. Q. Xie, X. Li, L. Jiang, B. Xia, X. Yan, W. Zhao, and Y. Lu, "High-aspect-ratio, high-quality microdrilling by electron density control using a femtosecond laser Bessel beam," Appl. Phys. A Mater. Sci. Process. **122**, 1–8 (2016).

113. A. Magos and L. Chapman, "Biodegradable, Elastic Shape-Memory Polymers for Potential Biomedical Applications," Obstet. Gynecol. Clin. North Am. **31**, 705–19, xii (2004).

114. B. Liu, J. Wang, X. Fan, Y. Kong, and H. Gao, "An effective bead-spring model for polymer simulation," (2007).

115. X. Provot, "Deformation Constraints in a Mass-Spring Model to Describe Rigid Cloth Behaviour," in *Proceedings of Graphics Interface '95*, GI '95 (Canadian Human-Computer Communications Society, 1995), pp. 147–154.

Publications

- Enhanced volumetric imaging in two-photon microscopy via acoustic lens beam shaping
  S. Piazza, P. Bianchini, C. Sheppard, A. Diaspro, M. Duocastella
  2017 - Journal of Biophotonics

- Laser-Induced localized growth of methylammonium lead halide perovskite nano-and microcrystals on substrates
  M.P. Arciniegas, A. Castelli, S. Piazza, S. Dogan, L. Ceseracciu, R. Krahne, M. Duocastella, L. Manna
  2017 - Advanced Functional Materials

- Towards nanopatterning by femtosecond laser ablation of pre-stretched elastomers
  S. Surdo, S. Piazza, L. Ceseracciu, A. Diaspro, M. Duocastella
  2016 - Applied Surface Science 374, 151-156

- Direct laser printing of tailored polymeric microlenses
  C. Florian, S. Piazza, A. Diaspro, P. Serra, M. Duocastella
  2016 - ACS Applied Materials & Interfaces 8 (27), 17028-17032

- Fast volumetric imaging in two-photon microscopy and enhanced background rejection using an acoustic lens
  S. Piazza, P. Bianchini, C. Sheppard, A. Diaspro, M. Duocastella
  2016 - Biophysical Journal 3 (110), 162a

ORAL PRESENTATIONS

- Laser direct-write nanofabrication using engineered materials and shaped light.
  S. Piazza, S. Surdo, A. Diaspro, M. Duocastella
  2017 – COLA – Marseille (France).

- Pixel-based Z-focus control in scanning microscopy.
  S. Piazza, T. Deguchi, P. Bianchini, A. Diaspro, M. Duocastella
  2017 – Focus on microscopy – Bordeaux (France).

POSTERS

- Fast volumetric imaging in two-photon microscopy and enhanced background rejection using an acoustic lens.
  S. Piazza, P. Bianchini, C. Sheppard, A. Diaspro, M. Duocastella.
  2016 - Biophysical Society Meeting - Los Angeles (California).

- Enhanced signal-to-background in two-photon microscopy via ultrafast beam shaping using an optofluidic acoustic lens.
  S. Piazza, P. Bianchini, C. Sheppard, A. Diaspro, M. Duocastella.
  2015 - Coherent bioimaging workshop - Genova (Italy).

- Free-standing and flexible 1D photonic crystals obtained by periodically arranged thin polymeric films.
  S. Piazza, S. Surdo, A. Diaspro, M. Duocastella.
  2015 - European Conference on Organized Films - Genova (Italy).